**Measuring mass and structure of the Universe with LSST:**

**importance of precise photometric redshift estimation and CCD sensor effects**

A Dissertation presented

by

**HyeYun Park**

to

The Graduate School

in Partial Fulfillment of the

Requirements

for the Degree of

**Doctor of Philosophy**

in

**Physics and Astronomy**

Stony Brook University

**August 2019**

**Stony Brook University**

The Graduate School

**HyeYun Park**

We, the dissertation committee for the above candidate for the

Doctor of Philosophy degree, hereby recommend

acceptance of this dissertation

**Dmitri Tsybychev - Dissertation Advisor**
**Associate Professor, Physics and Astronomy, Stony Brook University**

**Andrei Nomerotski - Dissertation Advisor**
**Scientist, Physics and Astronomy, Brookhaven National Laboratory**

**Rouven Essig - Chairperson of Defense, Committee**
**Associate Professor, CN Yang Institute for Theoretical Physics, Stony Brook University**

**Michael Zingale - Committee**
**Associate Professor, Physics and Astronomy, Stony Brook University**

**Paul Stankus - Committee, External Member**
**Scientist, Physics and Astronomy, Brookhaven National Laboratory**

This dissertation is accepted by the Graduate School

Eric Wertheimer
Dean of the Graduate School

Abstract of the Dissertation

**Measuring mass and structure of the Universe with LSST: importance of precise photometric redshift estimation and CCD sensor effects**

by

**HyeYun Park**

**Doctor of Philosophy**

in

**Physics and Astronomy**
Stony Brook University

**2019**

Sensor anomalies and photometric redshift are the main areas studied to find and correct the error in measurement of the cosmological parameters more precisely and more accurately. For this purpose, we have tested and analyzed over 200 CCD sensors used for Large Synoptic Survey Telescope (LSST) production at Brookhaven National Laboratory. Using those data, we have studied Tree Rings and Charge Transfer Efficiency. These two sensor effects were studied to correct shape distortion of the light sources due to the CCD, from the shear measurement for Weak Lensing research. We have developed a new method to study the blending effects in simulated data prepared for Data Challenge of Dark Energy Science Collaboration (DESC). We used it to systematically study the impact of blending on photometric redshift estimation. From observations we know that ordinary matter consist of 5 % of the Universe and the rest is dark matter and dark energy. The LSST is proposed to study dark matter and dark energy, collaborating with DESC. With improved understanding of blending effects and effective corrections of instrumental effects, we are one step closer to measure properties of dark energy and dark matter. More accurate and precise measurement of the cosmological parameters will support the survey to understand how the Universe has been formed and transformed over time.

## Dedication Page

For my brother, JoonKyu Park, who bravely left the family business, a.k.a. Physics. I wish with all my heart that my family and friends would find happiness in life, in their own ways.

Table of Contents

# Contents

**List of Figures/Tables/Illustrations**

# List of Figures

# List of Tables

## Acknowledgements

First and foremost, I would like to express my sincere gratitude to my advisors, Andrei Nomerotski, Dmitri Tsybychev, and Anže Slosar for the support during my Ph.D study, for their patience and motivation. I thank Neelima Sehgal who introduced me to meet them and helped me to start my research at Brookhaven National Laboratory. Anja von der Linden's idea for me to connect sensor effect to shear on weak lensing study became a sturdy base of my research. She also helped me to see the big picture of what I want to do and what my strengths are. I would also like to thank my committee Rouven Essig. His interest and many precious opinions on my research was very helpful. I was lucky to meet the people who value happiness the most and who cared for my physical and mental health very much. I learned not only how to become a good scientist but also how to live a good life.

I thank all my colleagues at BNL, Instrumentation and Astrophysics group, who placed a lot of effort to handle sensors with me and who taught me various fields of cosmology. I thank everyone in LSST−DESC team for their valuable discussions. Without their help, it would have been much harder for me to finish my PhD or to continue my academic career.

As a daughter of my loving parents who already went through the same path as physicists, I would like to thank them for showing me and my brother a big world and for believing in me even when I am the "sloth". I can't thank enough to all my family, friends and my cat △. I feel loved so much and they are the reason I am living for. I really appreciate everyone helping me to prepare my defense and to finish my PhD journey at SUNY Stony Brook.

## Vita, Publications and/or Fields of Study

H.Y.Park, A.Nomerotski, D.Tsybychev, *"Properties of Tree Rings in LSST Sensors"*, Jinst 12, C05015, 2017

P.Svirin, H.Y.Park, et al, *"BigPanDA: PanDA Workload Management System And Its Applications beyond ATLAS"*, CHEP, 2018

H.Y.Park, S.Karpov, A.Nomerotski, D.Tsybychev, *"Tree Rings in LSST Production Sensors: its dependence on radius, wavelength, and back bias voltage"*, JATIS, 2019

# 1 Introduction

## 1.1 Motivation

We observe that the Universe is expanding, but this idea was sensational in the 1920s. Edwin Hubble discovered that light from far away galaxies was redshifted, which means the wavelength of the light becomes longer (redder). This redshift behavior becomes larger for light from further away galaxies. For many years, it was hard to figure out the redshift-distance relation, why and how it works. As shown in Figure 1, the expanding Universe in time is in a bell-shape, meaning the expansion rate increased rapidly after the Big Bang and slowed down for the next several billion years after the "inflation" period. More recently, the expansion rate has begun to increase again due to dark energy pushing the Universe to expand further.

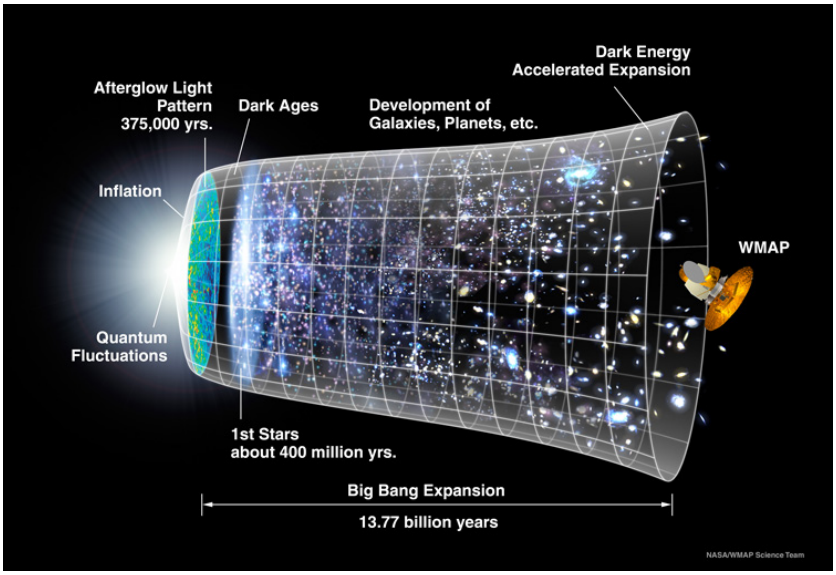


Figure 1: The evolution of the Universe over 13.7 billion years. Credit: NASA/WMAP Science Team [57].

The history of astrophysics and cosmology follows along with the improvement of telescopes and observation techniques. Kepler for example, found the laws of orbits of planets in the Solar System with Brahe's accuracy of 1 arcmin, which is equivalent to measuring the diameter of a human hair

at a distance of human arm. It helped Kepler to distinguish the elliptical orbit of Mars, which has ellipticity of 0.093. Further objects are fainter and harder to observe due to high noise but development of telescopes is helping astronomers to separate blurred objects and measure the shape, distance, and structure of the Universe better. Compared to the naked eye observation, modern survey like Gaia [38] can measure a diameter of a human hair at a distance of 1000 km, meaning 20 microarcsec of accuracy. Not only is the resolution of the observation improving, but with a better understanding of the systematic and statistical errors in recent observations, theory on expanding Universe is now established and supported.

The purpose of this study is to measure the cosmological parameters more precisely. A further goal is to understand the physics of dark matter and dark energy by studying the structure of the Universe: how it has been formed and it is expanding. The ratio of the components of the Universe is closely related to the acceleration of the expanding Universe, shape distortion and clustering of the galaxies due to the gravitational lensing. Apart from the cosmological effects, atmosphere and the observational devices alter the image and mislead the results in measuring the mass and shape of the light sources. In this dissertation, we are going to focus on the precise photometric redshift estimation and CCD sensor effects when measuring mass and structure of the Universe.

## 1.2 Studying dark matter and dark energy with large scale structures

### 1.2.1 Dark matter and Dark energy

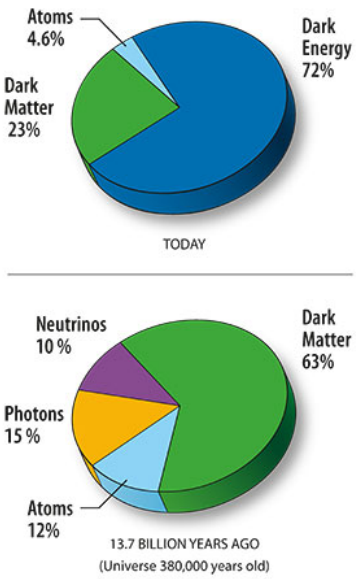


Figure 2: Content of the Universe pie chart adapted from NASA WMAP [59].

The Universe is composed of 70% dark energy, 25% dark matter and only 5% of baryonic matter in our cosmological model [39]. Measuring the density of these components and the Hubble constant in time is an important question to understand the history of the Universe: how the Universe is formed, how it is expanding.

The evidence of Dark Energy and Dark Matter's existence is indirect, but can be seen in various ways like in gravitational lensing, distance-redshift relations, and mass density of the Universe, none of which can be explained without them. The Universe has been expanding faster than the earlier Universe, and it needs more mass and energy than known ordinary matter to show the wave patterns of mass density we observe. Therefore measuring the distance, redshift, mass density, and shape distortion of the Universe is an important key to learn about the existence of Dark Matter, Dark Energy, and to study how the Universe has formed and evolved over time.

As mentioned earlier, the research on the expanding Universe begins with the discovery of the relation between the redshift ($z$) and the distance ($r$) of the galaxies:

$$z = \frac{\lambda_{observe} - \lambda_{emit}}{\lambda_{emit}} \tag{1}$$

which lead to the famous linear relation, Hubble's Law,

$$z = \frac{H_0}{c} r. \tag{2}$$

To describe the galaxies moving away from other galaxies in the expanding Universe and how this expansion depends on time, the scale factor $a(t)$ is defined as $1/(1+z)$. The function $a(t)$ is independent of location and direction, and $a(t_0)$ is one when $t_0$ is the present time.

Einstein's field equation from the theory of general relativity describes the curvature of a four dimensional space-time by linking the scale factor $a(t)$, the curvature constant $\kappa$, and the radius of the curved space $R$. With the general relativity, the Robertson-Walker metric can be written as:

$$ds^2 = -c^2dt^2 + a(t)^2[dr^2 + S_\kappa(r)^2 d\Omega^2] \tag{3}$$

where

$$d\Omega^2 \equiv d\theta^2 + \sin^2\theta d\phi^2 \tag{4}$$

and

$$S_\kappa(r) = \begin{cases} R\ \sin(r/R) & (\kappa = +1) \\ r & (\kappa = 0) \\ R\ \sinh(r/R) & (\kappa = -1). \end{cases} \tag{5}$$

Here we follow the notations from B. Ryden [48].

Einstein's field equation is the relativistic equivalent of Poisson equation in Newtonian dynamics,

$$\bigtriangledown^2\Phi = 4\pi G\rho = -\bigtriangledown\cdot\vec{g} \tag{6}$$

where $\Phi$ and $g$ are the gravitational potential and acceleration accordingly. This explains a relation between the gravitational potential and the mass density $\rho$.

Adding energy density $\epsilon(t)$ and pressure $P(t)$ to this, the Friedmann equation (Equation (7)) and the acceleration equation (Equation (8)) describe how the Universe expands.

$$\left(\frac{\dot{a}}{a}\right)^2 = \frac{8\pi G}{3c^2}\epsilon - \frac{\kappa c^2}{R^2a^2} \tag{7}$$

$$\frac{\ddot{a}}{a} = -\frac{4\pi G}{3c^2}(\epsilon + 3P) \tag{8}$$

Here the energy density $\epsilon$ can be rewritten with the scale factor and the equation-of-state parameter $w$ as:

$$\epsilon(a) = \epsilon_0 a^{-3(1+w)}, \tag{9}$$

where $w$ is zero for non-relativistic matter, 1/3 for the radiation (or ultra-relativistic matter), and -1 for the lambda (dark energy) dominated universe. The Friedmann equation in the form of density parameter $\Omega(t) \equiv \epsilon(t)/\epsilon_c(t)$ is,

$$\frac{H^2}{H_0^2} = \frac{\Omega_{r,0}}{a^4} + \frac{\Omega_{m,0}}{a^3} + \Omega_{\Lambda,0} + \frac{1-\Omega_0}{a^2}, \tag{10}$$

where $\Omega_0 = \Omega_{r,0} + \Omega_{m,0} + \Omega_{\Lambda,0}$. Equation (10) shows that the expansion of the Universe will differ as the ratio of the mass density and hence the distance and the power spectrum will follow the structure of the Universe in time. We will discuss more about the power spectrum and the correlation function in Chapter 1.2.3.

### 1.2.2 Large Scale Structure

The Large Scale Structure of the Universe refers to groups of galaxies in a scale of 10 to 100 Mpc, which is equivalent to hundreds of millions to billions of light years in length. The large scale structure takes an important role in understanding grouping mass in the Universe, which relates with gravity, Dark Energy, and how the Universe evolves in time. The large scale structure consists of approximately 10% hot gas, 90% Dark Matter, and less than 1% of galaxies and stars. Therefore, astronomers study the large scale structure with its X-ray emitted by hot gas, gravitational lensing, and internal structure.

### 1.2.3 Weak Lensing

Two-point correlation is a powerful way nowadays to study the mass and shape distribution of the galaxies in the Universe. "3x2pt" refers to the three different types of two-point correlation function measurements: Galaxy Clustering, Galaxy-Galaxy Lensing, and Cosmic Shear. The idea is to pair all galaxies in the Universe, and measure the correlation of each pair's position to position (Galaxy Clustering), position to shape (Galaxy-Galaxy Lensing), and shape to shape (Cosmic Shear) [2].

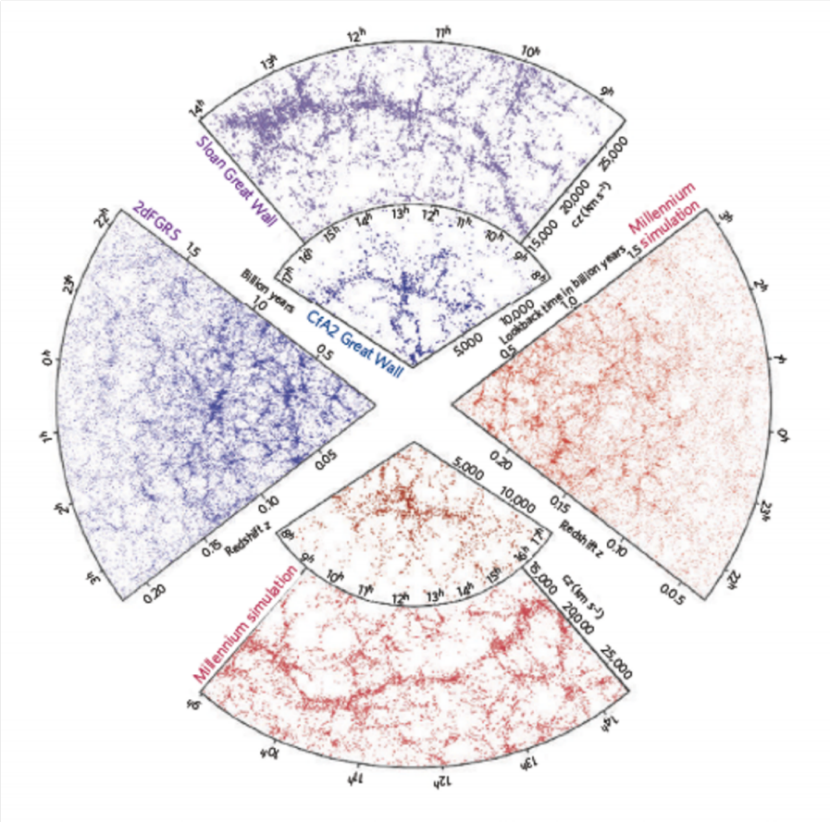


Figure 3: Large Scale Structure image adapted from V. Springel [3]. Each slice shows the galaxy distribution obtained from spectroscopic redshift surveys and from mock catalogs constructed from cosmological simulations: the CfA2 'Great Wall', the SDSS 'Sloan Great Wall', the 2dFGRS, and the 'Millennium' simulation. The top slice of SDSS Sloan Great Wall shows the largest observed structures in the Universe, covering 10,000 galaxies and 1.37 billion light years.

Estimating two fundamental cosmology parameters $\sigma_8$ and $\Omega_m$ and comparing them with observations such as supernovae and baryon acoustic oscillations leads us to a measurement of how much matter clusters consists the Universe ($\sigma_8$) and the overall density of matter in the Universe ($\Omega_m$). DES (Dark Energy Survey) used 3x2pt correlation to measure $\sigma_8$ and $S_8$ and the results are shown as a contour plot of $\sigma_8$ (or $S_8$ which is a combination of $\sigma_8$

and $\Omega_m$) vs $\Omega_m$ and compared to Planck CMB satellite telescope's results [2] (see Figure 4).

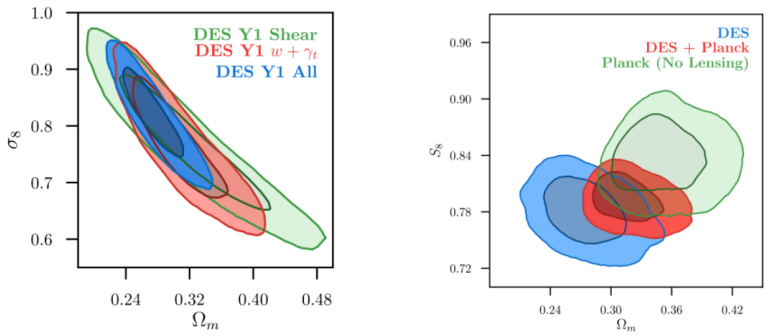


Figure 4: The constraints achieved on $\sigma_8$ (or $S_8$) and $\Omega_m$. Image adapted from [2].

Generally, ellipticity is defined in terms of the a and b (major and minor) axis and $\theta$, the angle between the coordinate system and the major-minor axis, as follows

$$\begin{pmatrix}\chi_1\\ \chi_2\end{pmatrix} = \frac{1-\beta}{1+\beta}\begin{pmatrix}cos2\theta\\ sin2\theta\end{pmatrix} \tag{11}$$

$$\chi = \frac{(a^2-b^2)}{(a^2+b^2)} = \chi_1 + i\chi_2. \tag{12}$$

However we need "shear" information in the + (horizontal and perpendicular) and the x (cross, 45 degrees rotated from +) directions, to find a correlation between two objects in every pair. Here, horizontal and perpendicular direction, respectively, means along and 90 degrees with respect to the vector connecting the two galaxies. We use the combinations of the second central moments to define the second-moment squared radius $r^2$ and two complex ellipticities $\chi$ and $\epsilon$ as shown below. Here we are going to follow the notation

of the ellipticity, second moment, and shear by Meyer and Burchat [45]:

$$r^2 = I_{xx} + I_{yy} \tag{13}$$

$$\chi_1 = \frac{I_{xx} - I_{yy}}{I_{xx} + I_{yy}} \tag{14}$$

$$\chi_2 = \frac{2I_{xy}}{I_{xx} + I_{yy}} \tag{15}$$

$$\epsilon_1 = \frac{I_{xx} - I_{yy}}{I_{xx} + I_{yy} + 2\sqrt{I_{xx}I_{yy} - I_{xy}^2}} \tag{16}$$

$$\epsilon_1 = \frac{2I_{xy}}{I_{xx} + I_{yy} + 2\sqrt{I_{xx}I_{yy} - I_{xy}^2}}. \tag{17}$$

Here $I_{\mu\nu}$ is the second central moments of a galaxy's surface brightness distribution:

$$I_{\mu\nu} = \frac{1}{f}\int I(x,y)(\mu - \langle\mu\rangle)(\nu - \langle\nu\rangle)dxdy \tag{18}$$

when $\mu$ and $\nu$ are the angular coordinate $x$ or $y$. The centroids $\langle\mu\rangle$ (and $\langle\nu\rangle$) and the total flux $f$ of the galaxy are given as:

$$\langle\mu\rangle = \frac{1}{f}\int I(x,y)\mu dxdy, \tag{19}$$

$$f = \int I(x,y)dxdy. \tag{20}$$

With the gravitational lensing, the shear $\gamma = \gamma_1 + i\gamma_2$ and the reduced shear $g = \gamma/(1-\kappa)$ relate the lensed ellipticities $\chi^{(a)}$ and $\epsilon^{(a)}$ to unlensed ellipticities $\chi^{(i)}$ and $\epsilon^{(i)}$ as

$$\chi^{(a)} = \frac{\chi^{(i)} + 2g + g^2\langle\chi^{(i)}\rangle}{1 + |g|^2 + 2Re(g\langle\chi^{(i)}\rangle)} \tag{21}$$

$$\epsilon^{(a)} = \frac{\epsilon^{(i)} + g}{1 + \langle g\rangle\epsilon^{(i)}}, \tag{22}$$

when $\kappa$ is the convergence. The intrinsic (unlensed) galaxy ellipticities average out assuming they are isotropically distributed, the mean of the apparent (sheared) ellipticities are related with reduced shear $g$ as:

$$\langle\chi^{(a)}\rangle = 2g \tag{23}$$

$$\langle\epsilon^{(a)}\rangle = g. \tag{24}$$

The probability of an object that appears in the volume $dV$ with the number density $n$ can be calculated by Equation (25), and two-point correlation function $\xi$ will be added as in Equation (26) to get the probability of having objects in each volume $dV_1$ and $dV_2$, with distances between the two by $r_{12}$.

$$dP = ndV \tag{25}$$

$$dP = n^2 dV_1 dV_2 [1 + \xi(r_{12})] \tag{26}$$

$$\xi(r) = \langle f(\vec{x} + \vec{r}) f(\vec{x}) \rangle / \langle f \rangle^2 - 1 \tag{27}$$

If the Universe is homogeneous and all the objects are spread out randomly without any dependence on distance between the objects, the continuous function $f(\vec{r})$ in Equation (27) will be a constant and $\xi$ will be zero.

The variance of the number of randomly spread out objects over the volume $V$ is

$$\begin{aligned} \sigma^2 &= \langle (N - \overline{N})^2 \rangle \\ &= nV + n^2 \int_v dV_1 dV_2 \xi(r_{12}) \qquad (28) \\ &= nV + n^2 \int d^3k P(k) |W_{\vec{k}}|^2 \qquad (29) \end{aligned}$$

where $W_{\vec{k}} = \int_V d^3 r e^{i\vec{k}\vec{r}} / (2\pi)^{3/2}$.

In terms of the density contrast $\delta$ to describe a density perturbation, the power spectrum and the correlation function can be written as

$$\delta(\vec{x}) = \frac{\rho(\vec{x})}{\langle \rho \rangle} - 1 \tag{30}$$

$$\delta_k = \frac{1}{V} \int_V \delta(\vec{x}) exp^{-i\vec{k}\cdot\vec{x}} d^3\vec{x} \tag{31}$$

$$P(k) = \langle |\delta_k|^2 \rangle_{|\vec{k}|=k} \tag{32}$$

$$\xi(r) = \langle \langle \delta(\vec{x}) \delta(\vec{x} + \vec{r}) \rangle_{\vec{x}} \rangle_{|\vec{r}|=r} \tag{33}$$

The power spectrum $P(k)$ is defined as a Fourier transform of the correlation function $\xi(r)$ as

$$\xi(r) = \frac{V}{(2\pi)^3} \int P(k) e^{-i\vec{k}\cdot\vec{r}} d^3\vec{k}. \tag{34}$$

In terms of angular coordinates with $\ell$ as a wavenumber, the power spectrum $C_X(\ell)$ and the correlation function $\xi_{+,XX}(\theta)$ can be written as discussed in C. Chang [1],

$$\xi_{+,XX}(\theta) = \langle X_t(\theta_0) X_t(\theta_0 + \theta) \rangle + \langle X_\times(\theta_0) X_\times(\theta_0 + \theta) \rangle \tag{35}$$

$$C_X(\ell) = 2\pi \int_0^\infty d\theta \ \theta \ \xi_{+,XX}(\theta) J_0(\ell\theta) \tag{36}$$

$$\xi_{+,XX}(\theta) = 12\pi \int_0^\infty d\ell \ \ell \ C_X(\ell) J_0(\ell\theta) \tag{37}$$

where X is a ellipticity $\epsilon$ or shear $\gamma$, and the subscripts t and $\times$ indicate the + (perpendicular and horizontal direction) and x (45 degrees from + direction) decomposition along the line connecting a pair of galaxies. $J_0$ is the Bessel Function at zeroth order, $J_0(x) = \sin(x)/x$.

The power spectrum can be expressed in terms of a transfer function $T(k, z)$ as well, as discussed by C. Baugh [40],

$$P(k, z) = A(z) k^n T(k, z) \tag{38}$$

where $A(z)$ is the normalization factor. As shown in Figure 5 by C. Baugh [40], the shape of the power spectrum depends on the density of the components of the Universe. For example, the Harrison-Zeldovich form of the primordial power spectrum as the long dashed line in Figure 5 shows the linear relation between the power spectrum and the wavenumber $k$ ($k = 2\pi/\lambda$). Depending on the ratio of the dark matter, baryonic matter, neutrinos and cosmological constant contained in the Universe, the shape of the power spectrum changes, and it can be determined by the observations. In this dissertation, we will not discuss the correlation functions in details but will study the impact of the sensor effects on shear correlation in Chapter 6.

The accuracy of measuring the shear is defined by $m$ and $c$ as

$$g_i^{obs} = g_i^{true} + m_i g^{true} + c_i, \ i = 1, 2 \tag{39}$$

The shear bias parameters $m$ and $c$ specifications for the LSST is

$$m < 3 \times 10^{-3} \tag{40}$$

$$c < 2 \times 10^{-4} \tag{41}$$

$$Var(c) < 1.8 \times 10^{-7}. \tag{42}$$

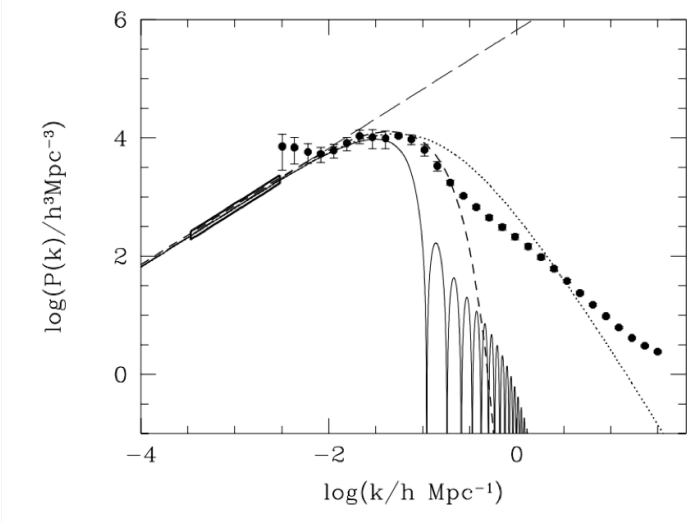


Figure 5: Examples of power spectra image adapted from P. Murdin [40]. The long dashed line shows the primordial power spectrum, $P(k)$ proportional to $k$. The dotted line, solid line, and short dashed line show the cold dark matter, baryonic matter, and massive neutrinos dominated Universe accordingly. The big dotted line with error bars is the COBE satellite measurement of temperature fluctuations in the CMB.

We can measure these shear calibration parameters by:

$$m_1 = m_2 = \frac{-(\triangle I^{PSF}_{xx} + \triangle I^{PSF}_{yy})}{r^2_{gal}} \tag{43}$$

$$c_1 = \frac{\triangle I^{PSF}_{xx} - \triangle I^{PSF}_{yy}}{2r^2_{gal}} \tag{44}$$

$$c_2 = \frac{\triangle I^{PSF}_{xy}}{r^2_{gal}} \tag{45}$$

when $\triangle I^{PSF}_{\mu\nu}$ is the difference between second central moments of galactic and stellar PSFs (Point Spread Function). PSF is a size and shape estimation of galaxies and stars on CCD.

In Chapter 6, we will write the second moment terms as $XX$, $YY$ and $XY$ instead of $I_{xx}, I_{yy}$ and $I_{xy}$. The reduced shear $g$ will be measured using the second moment $XX$, $YY$, $XY$, and ellipticity $e1$ and $e2$, and then we will

check if the Tree ring effect and Charge Transfer Efficiency are insignificant such that they satisfy the $m$ and $c$ limit of the accuracy.

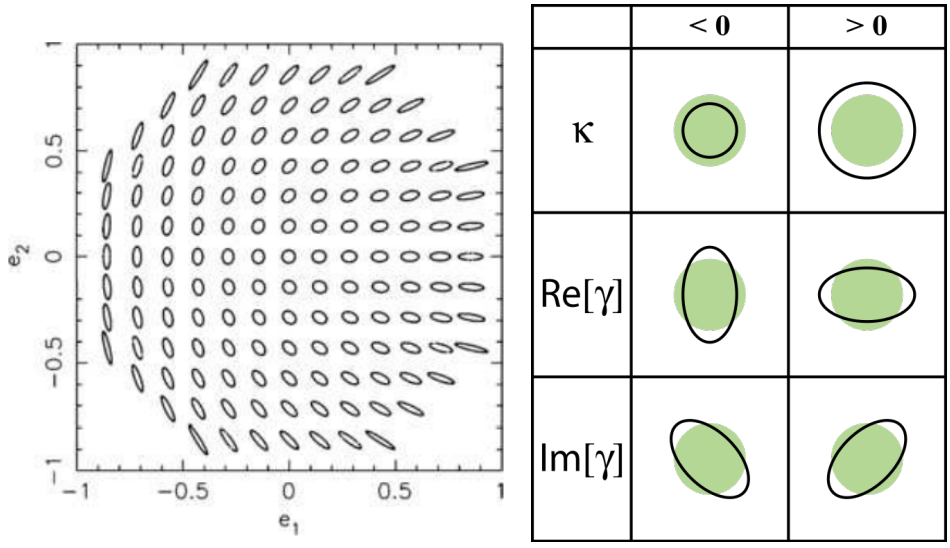


Figure 6: Left: The shape of elliptical object according to $e1$ and $e2$ values. Adapted image from the handbook for the GREAT08 Challenge [66]. Right: We can measure the shear in + and x direction. Image adapted from [37]. The solid green circle represents the circular source and black elliptical line shows the convergence and shear according to its positive/negative values.

## 1.3 Photometric Calibration

Astrophysics has been developing along with the improvement in precise measurement of astronomical parameters. Higher accuracy in measurements allow us to confirm or disprove the cosmological theories, separating the noise from actual cosmological effects. CMB (Cosmic Microwave Background) polarization and the shear need to be measured precisely with very high signal-to-noise ratio, since they are dealing with faint objects and a weak distortion in the shapes in the range of 1 % [4]. Hence understanding and correction of systematic uncertainties are necessary to study weak lensing. Systematic uncertainties like photometric redshift estimation, Point Spread

Function (PSF), detector effects, and galaxy selection bias are very important for more accurate measurement of redshift, number density, and shear [7].

In measuring lensing shear, blurred image and shape distortion due to the atmosphere, telescope optics, and sensors can cause significant errors. In this dissertation, we mainly study two sensor effects: the Tree rings effect and CTE, and photometric redshift estimation along with blending issue for more precise and accurate measurement of shear in weak lensing research.

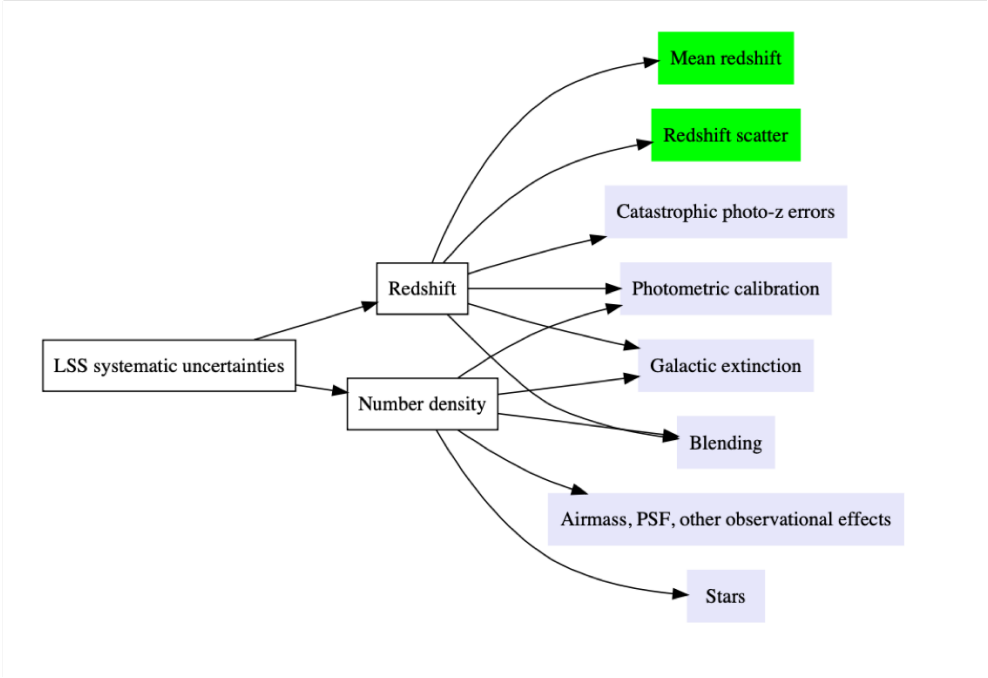


Figure 7: A diagram indicating sources of systematic uncertainties for the Large Scale Structure analysis to place requirements in the DESC SRD [7].

### 1.3.1 Sensor Anomalies

Charge-Coupled Device (CCD) is a sensor that converts information from photons to electrons. The LSST uses sensors from two manufacturing companies, e2v and ITL. Each CCD for LSST has 4k x 4k (4072 pixels x 4000 pixels for ITL and 4096 pixels x 4004 pixels for e2v) and 4 cm x 4 cm in

size. Each sensor is divided into 16 segments and all the segments output data at the same time with a readout time of two seconds [12]. Each pixel collects electrons in the potential well during the exposure time and when the shutter closes, each pixel's information is moved row by row and column by column for the readout. Uncertainty in position, size, and shape can occur when the movements of electrons are disturbed during the readout, or while the electrons are propogating through the silicon wafer.

We are going to show our study of two sensor effects investigated for LSST, Tree rings and Charge Transfer Efficiency (CTE), and analyze how they distort the shape of the light source compared to the error limits on size and shape of the weak gravitational lensing study. In Chapter 3 and Chapter 4, the methodology and results from 189 LSST production sensors for the Tree ring effect and CTE will be discussed. The influence of those sensor effects on shear measurement will be discussed in Chapter 6.

### 1.3.2 Photometric Redshift Calibration

There are two ways to measure the redshift: spectroscopy and photometry. LSST uses photometry, which can measure hundreds of galaxies at once but has a larger uncertainty compared to spectroscopy, which uses the spectrum of the source to determine the exact absorption lines of a single or a few galaxies at once. LSST has five filters to collect the light in six different range of wavelengths. We use these filters to get the color information and to estimate the redshift from the pattern of the flux in each band.

Also, when multiple objects are observed as a single object either due to the noise or due to the bright object merging with other faint objects, it is called blending, and this can cause a completely different redshift calibration. Blended objects will cause errors in measuring the mass distribution of the Universe and shear. We will describe photometric redshift calibration and de-blending in Chapter 5.

## 1.4 Large Synoptic Survey Telescope

The Large Synoptic Survey Telescope (LSST) is a ten-year, deep and wide optical survey, currently under construction in Chile [7]. The LSST will be built on Cerro Pachŏn, a mountain located in north-central Chile, with the benefit of low humidity suitable for infrared observations. The location of LSST is shown in Figure 8.


Figure 8: The location of LSST in Chile on Google Maps.

It is designed to study the four principal scientific topics: Dark Matter and Dark Energy, the Solar System, the Transient Optical Sky, and the Milky Way. LSST will cover 20,000 square degrees of the sky recording images of ten billion galaxies in six light bands: u, g, r, i, z, y. The first observation is planned in 2022. The LSST camera consists of 21 Science Raft Tower Modules (RTMs), which were all built and tested at Brookhaven National Laboratory (BNL) during 2016-2019. Each raft has nine 4k x 4k CCD sensors from either e2v or ITL vendors [55, 56]. The testing datasets are available for more than 200 sensors with electro-optical (EO) and metrological measurements performed at the BNL and SLAC national laboratory (SLAC). The sensor teststands and testing procedures have been described in detail previously (R. Coles et al. [21]). In Chapter 2 the sensor testing, analysis, and construction handling will be discussed including the raft building, EO and metrology test.

When construction is completed, the LSST facility will include a rotating

Figure 9: LSST site construction status updated on May 10 2019. Pictures adapted from the LSST gallery website [58].

dome that is 30 m wide and a 3000 $m^2$ of service and an operations building. The cutaway view of the facility is shown in Figure 10. The bottom right corner of the white building is where the clean room and control/monitor room will be held. The LSST telescope and facility will be highly automated and with operators on duty, researchers will be able to monitor the progress remotely at any operation center. The dome will hold the telescope with 11 m x 11 m screen protecting the telescope from the wind and light.

The LSST telescope will have three aspheric mirrors: an 8.4 m primary mirror (M1), a 3.5 m convex secondary mirror (M2), and a 5.0 m tertiary mirror (M3). The three mirrors shown in Figure 12 make LSST unique to deliver a 3.5 degree field of view, covering 64 cm diameter flat focal plane. The camera will be located after M3. It will have three large fused-silica lenses, a filter wheel capable of holding 5 filters, camera sensors, and a system for vacuum and temperature control. The LSST camera instrumentation, including lenses, filters, and sensors, are shown in Figure 12.

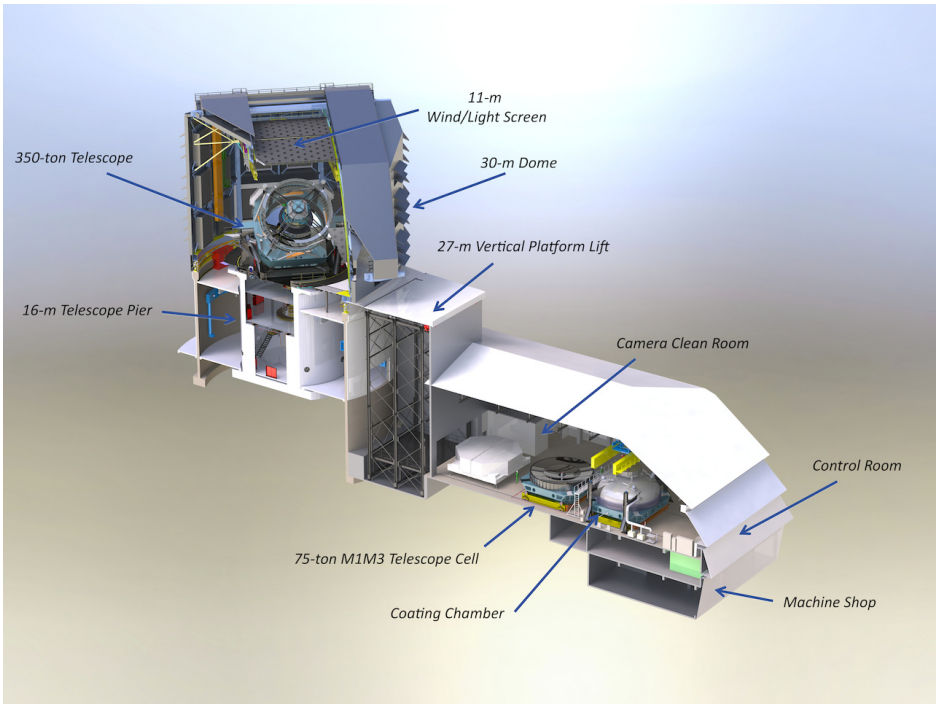


Figure 10: Artistic conception of LSST facility. Picture adapted from the LSST telescope and site information website [58].

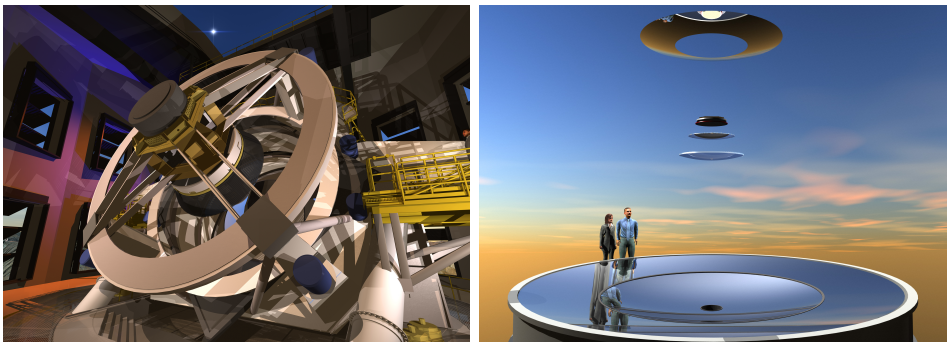

Figure 11: Left: Telescope inside the dome. Right: Three mirrors. Pictures adapted from the LSST telescope and site information website [58]

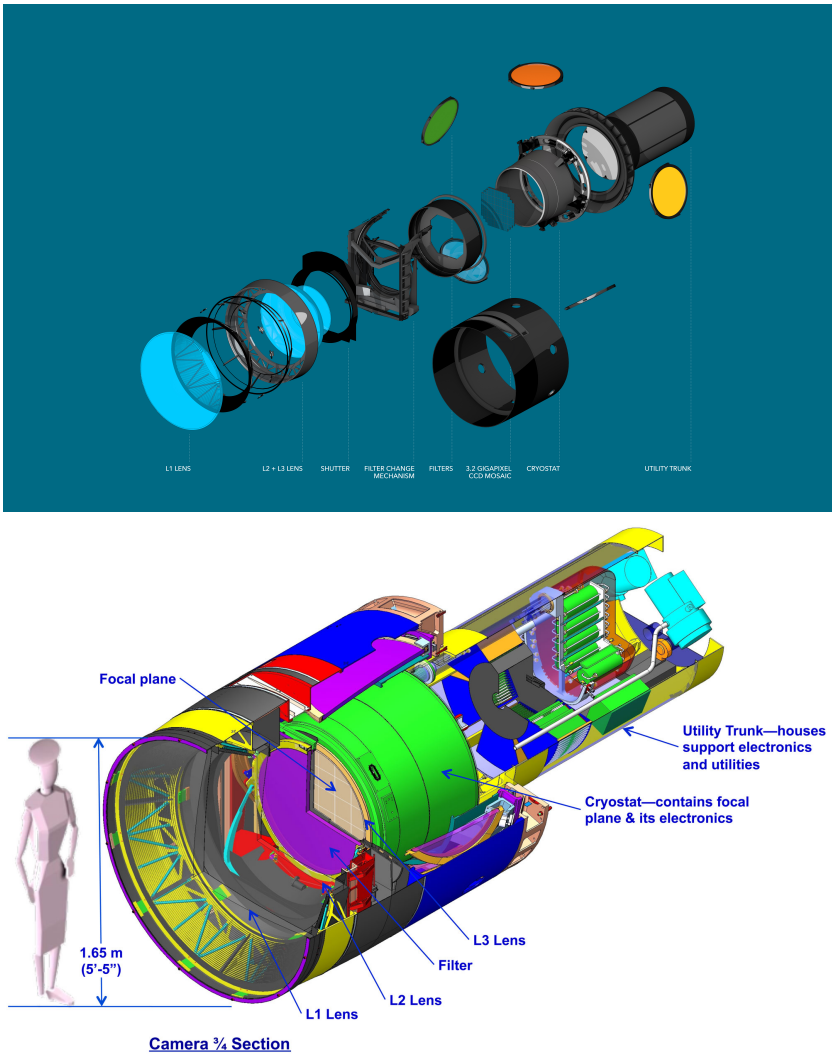


Figure 12: The LSST camera instrumentation including three large fused-silica lenses, five filters, and camera sensors. Pictures adapted from the LSST telescope and site information website [58]

## 1.5 Dark Energy Science Collaboration

The Dark Energy Science Collaboration (DESC) will analyze the LSST data aiming to study various fields in cosmology focusing on Dark Energy. Each working group of DESC focuses on a specific area of science and a technical area (Figure 13). The DESC uses the Science Roadmap (SRM) for long-term planning to meet its scientific goals [13].

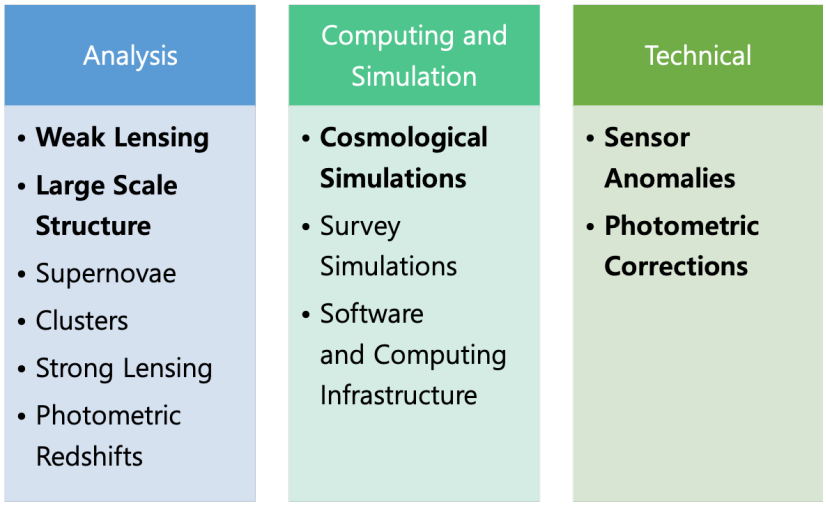


Figure 13: DESC working groups (The working groups I mainly worked with are in bold font). Figure adapted from DESC SRM [13].

In this dissertation, three categories will be discussed: instrumentation for the Sensor Anomalies working group (SAWG), 3x2pt correlation for the Large Scale Structure (LSS) working group, and input-output catalog matching for deblending and photometric redshift estimation for the Data Challenge (DC). The SAWG is developing correction procedures and investigating the residual systematics to measure cosmological parameters more accurately and precisely. The LSS working group studies mass and shape distribution of large scale structures at scales between 30 and 200 megaparsecs to study dark energy and dark matter in the Universe. DC has two goals: to study catalog defining cuts and how they affect the cleanliness of the sample, and to study the efficiency of deblending algorithms in the full realistic sky. DC

of DESC has three phases and it is now on the second phase, DC2. We are going to increase the variables and the size of the simulations during later phases. We are using FoF (Friends of Friends) algorithm which puts input and output objects together and group them by maximum separation. After binning the groups according to their number of input and output objects, we compare the flux of input and output objects in each groups to find how de-blender in DC2 is performing and ways to improve it.

# 2 Testing sensors at Brookhaven National Laboratory

## 2.1 CCD sensors of LSST

The whole focal plane of LSST will require 21 rafts which will require nine sensors per raft and hence 189 sensors in total. The four corner rafts shown in Figure 14 require three sensors each. Each CCD sensor of LSST has 4 k x 4 k pixels (4000 pix by 4072 pix for ITL and 4004 pix by 4096 pix for e2v) and 4 cm x 4 cm size. Size in pixels are written in order of y axis by x axis. Each sensor is divided into 16 segments and all the segments collect data at the same time with a readout time of 2 seconds [12]. The whole focal plane of LSST will capture images of millions of stars and billions of galaxies every night. More details on CCD sensors of LSST will be discussed in Chapter 4.

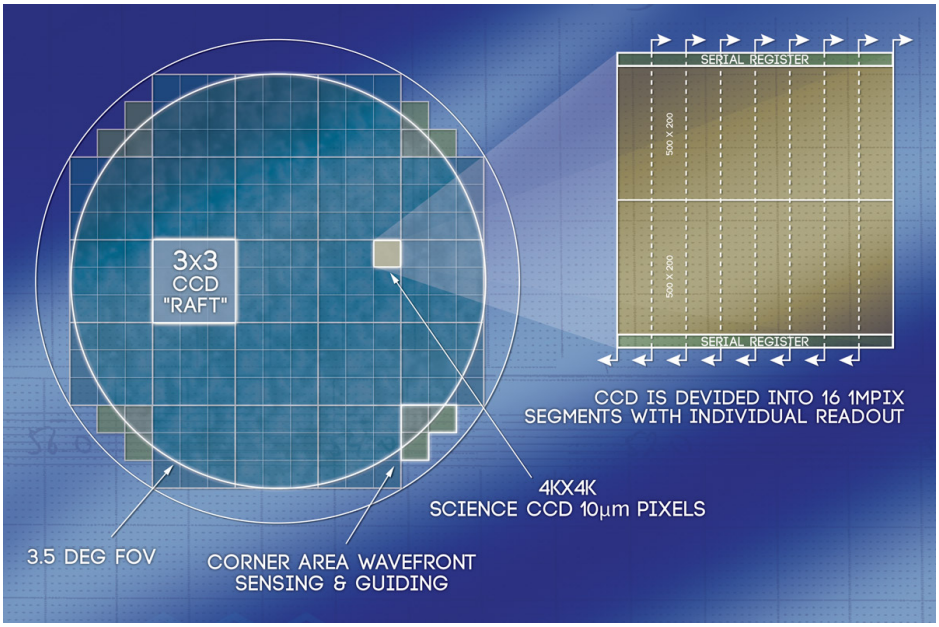


Figure 14: The whole focal plane of LSST image adapted from LSST camera web page [58].

## 2.2 Cleanroom at BNL

LSST is under a construction in Chile; however, many institutes are sharing the responsibilities for each part, such as CCD camera, mirrors, and lens. BNL and SLAC are in charge of constructing the whole focal plane with 21 rafts and four corner rafts. BNL tests all the sensors at a single sensor level and a single raft level, for Electro Optics (EO) and metrology. BNL is also responsible for assembling the modules into the raft structures before sending them to SLAC. Then SLAC re-verifies the rafts and builds the whole focal plane assembly (FPA).

During the four years of my research at BNL, I worked on all the Test Stands' (TS) work related to CCD sensors such as receiving sensors from e2v and ITL vendors, testing Electro-Optics (EO) and metrology for a single sensor and a raft, and assembling and disassembling the raft with nine sensors. (Figure 15)

Figure 15: Cleanroom at BNL. Left: Two identical test stands in the picture are TS3-1 and TS3-2. Right: The picture shows TS5 measuring the flatness of nine sensors combined in a raft.

## 2.3 TS1 : visual inspection

When the sensors arrive at BNL from the two vendors, e2v and ITL, we receive them at TS1 and take the necessary photos to make sure the sensors are clean without any dusts, particulates, or damage. Examples of visual inspection is shown on Figure 16. Each sensor is inspected for any obvious

mechanical defects by eye. If there are any particulates on the sensor surface, we use a single-hair brush to gently remove the particulate, and if the particulate is on the back side of the sensor or other parts, we use an ionized air blow and various brushes to clean the sensors.

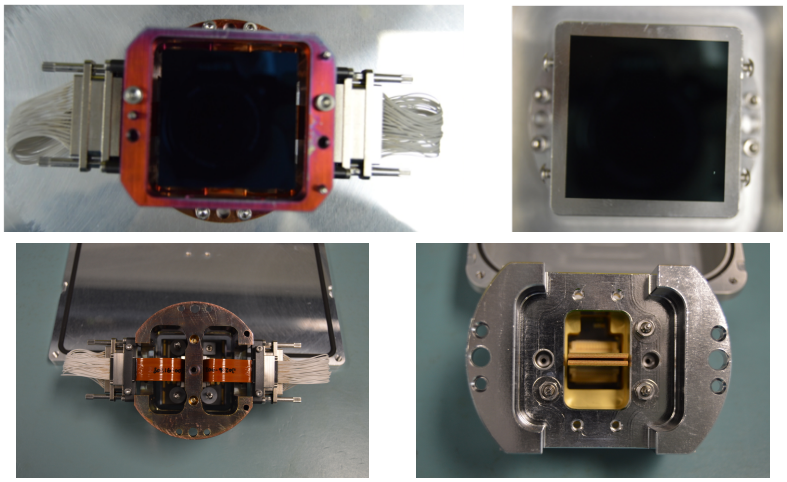

Figure 16: Top view and bottom view of e2v (left) and ITL (right) in a jig during visual inspection. e2v has its own flex cables attached, but since ITL doesn't, LSST makes flex cables for ITL and stycasts them. Three studs on the back are used to install the sensor on the raft baseplate.

## 2.4 TS2 and TS5 : Metrology

As shown in Figure 17, nine sensors are assembled into a raft at BNL and 21 rafts will be assembled into the focal plane assembly at SLAC. For each unit, we need to measure the flatness of their surface. BNL needs to test a single sensor and a raft to see if they meet the flatness tolerance requirements. TS2 and TS5 are where the metrology is measured for a single sensor and for a raft. As we can see from Figure 18, each detector module must be flat within a 5 $\mu$m PV (Peak-to-Valley) tolerance and nine modules in a raft must be flat within a 6.5 $\mu$m PV tolerance [20]. A single sensor is mounted on a 3-point ball-and-vee kinematic mount system to be placed under a coordinate measuring machine (the OGP machine) at room temperature. When we

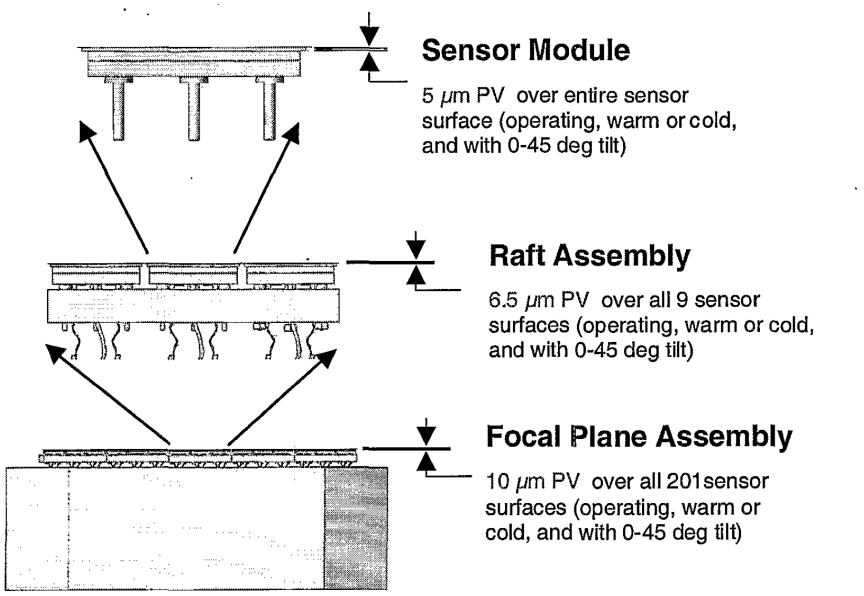


Figure 17: A diagram showing sensor to raft, raft to focal plane assembly [20].

measure the heights of nine sensors in a raft, we measure them through a window of the cryostat with the sensors cooled down to their operating temperature, which is $-100$ °C. A 2D surface profile map is produced using a beam-scanning mechanism.

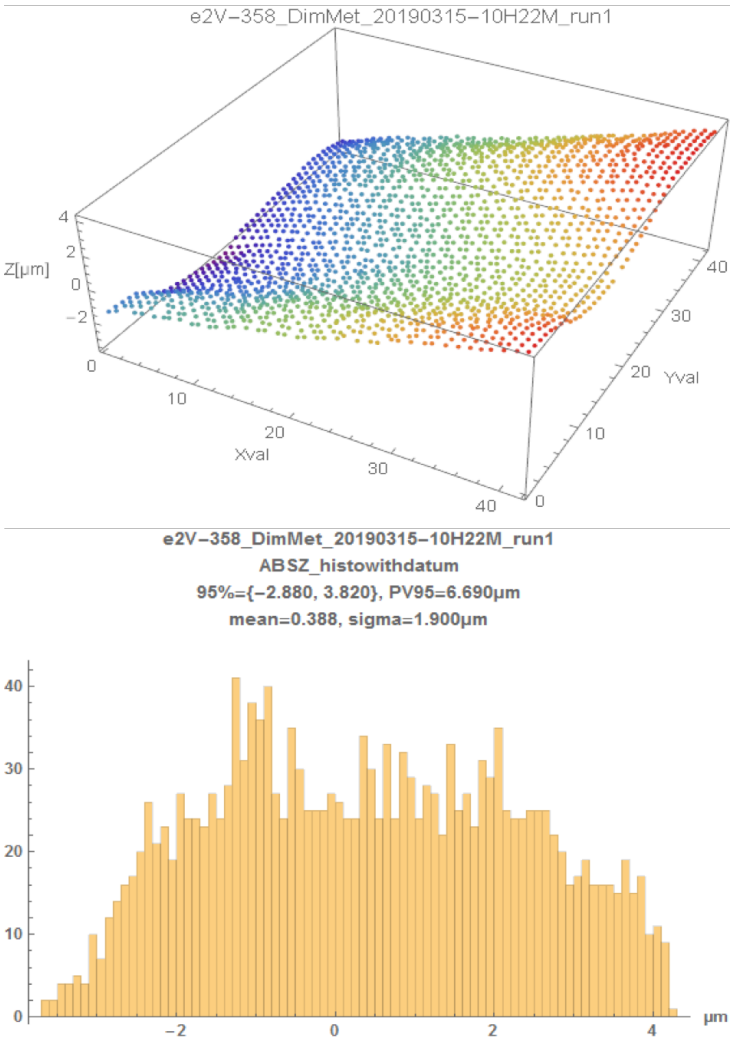


Figure 18: Absolute heights measurement for a single sensor, e2v-CCD250-358, at TS2. Top : A 3d image of surface flatness. Bottom : A histogram of absolute heights.

| Description | Specification | Measurement |
|---|---|---|
| Read noise | <8e- | 4.72 - 5.04e- |
| Blooming full well | <175ke- | 115-120 ke- |
| non-linearity | <2% | max deviation 1.7% |
| cross talk | $< 1.9 \times 10^{-3}$ | not measured |
| PRNU | $< 5\%$ | max variation 4.2% at 350 nm |
| u band QE | $> 41\%$ | 55.4% |
| g band QE | $> 78\%$ | 87.4% |
| r band QE | $> 83\%$ | 92.1% |
| i band QE | $> 82\%$ | 95.5% |
| z band QE | $> 75\%$ | 91.9% |
| y band QE | $> 21\%$ | 35.4% |
| Bright pixels | | 60 |
| Dark pixels | | 486 |
| Bright columns | | 0 |
| Dark columns | | 6 |
| Traps > 200 e- | | 0 |
| Cosmetic, sum of above | $< 0.5\%$ defective pixels | 0.08%, 12504 defective pixels |
| Dark current 95-th percentile | $< 0.2$ e-/s | 0.02 e-/s |
| Serial CTE | $> 0.999995$ | $0.999947 + / - 9 \times 10^{-6}$ |
| Parallel CTE | $> 0.999997$ | $0.9999995 + / - 6 \times 10^{-6}$ |
| Point spread function, sigma | $< 5$ micron | 3.64 micron |

Figure 19: An example of specifications for e2v sensors [17]. The quality of a sensor is characterized by these parameters in order to see the sensor performances in the following specific areas.

## 2.5 TS3 and TS7/TS8 : Electro Optical test

Two TS3s (TS3-1 and TS3-2) are used to measure the Electro Optical (EO) test on a single sensor. We can perform a warm EO to check all the 16 channels are working and check bias noise roughly. For the selected sensors we have full EO run to take images, including flat images with various wavelengths and Fe-55 images. An Fe-55 X-ray exposure device is installed inside the Dewar for calibration purposes. These images are needed to check the specifications for the LSST, such as linearity, CTEs (Charge Transfer Efficiencies), read noise, and PRNU (Pixel Response Non Uniformity). Some of specifications checked for the quality of sensors is shown in Figure 19.

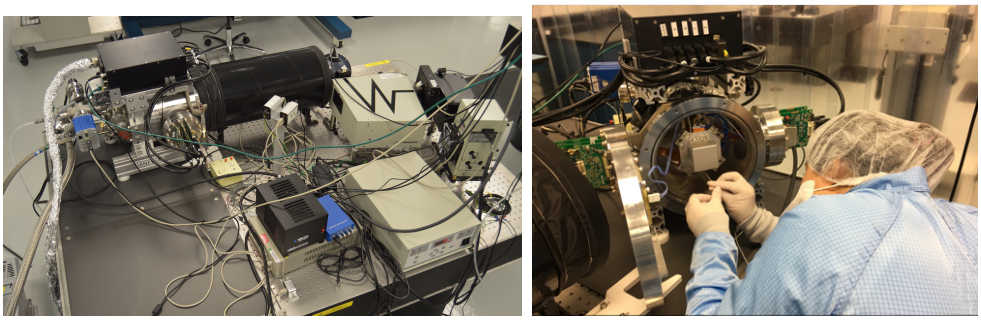

Figure 20: Left: TS3 layout showing lamp, monochromater, dark tunnel, cryostat and vacuums [17]. Right: Installing ITL sensor into the TS3-2 cryostat.

TS3 and TS7/TS8 have a similar setup (see Figure 21). A single sensor or a raft is mounted on the cryostat as shown in Figure 20. The light from the 300 W xenon arc lamp is reflected at an off-axis parabolic mirror, through a shutter and a filter wheel. The filter wheel holds two filters. A specific wavelength in need can be chosen using the Cornerstone 260 monochromator, which will split the light with a prism to choose the desired wavelength of light by the angle. Then the light with specific wavelength goes into a six inch diameter Labsphere integrating sphere so that the light loses its spatial information. The uniform light exits from the sphere and enters a drift space (a dark tunnel). The drift space distance was chosen to optimize the uniformity versus sacrificed flux. The light enters a BNL custom designed cryostat, which holds the CCD in vacuum and at its operating temperature of $-90\ ^{\circ}C$ or $-100\ ^{\circ}C$ [21].

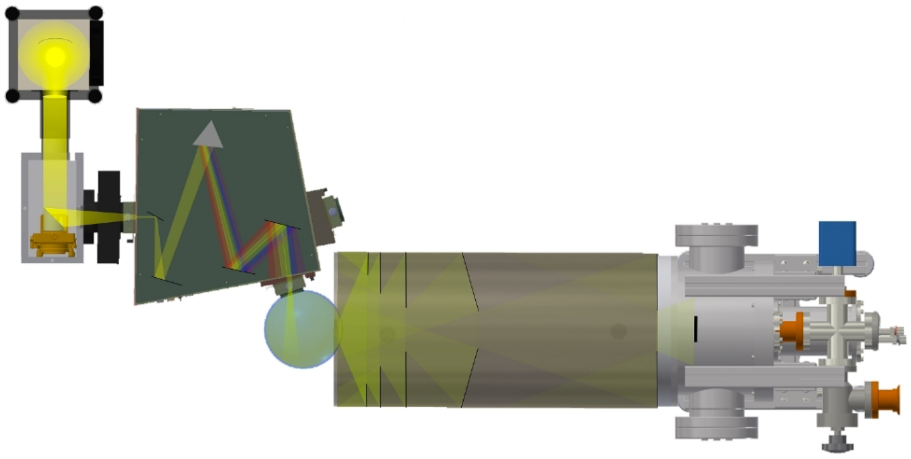

Figure 21: Sketch for TS3 setup to measure a single sensor EO [21].

Similar to the single sensor EO, raft EO also takes multiple flat images with different wavelengths and Fe-55 images of all nine sensors combined in a raft. TS3 and TS7/TS8 have same the setup, from the lamp to the sensor (or raft for TS7) in the cryostat. Internal details of TS7 cyrostat are shown in Figure 23. It is connected to heating control and vacuum control to test the EO and metrology under vacuum and at temperature $-90\ ^{\circ}C$ and $100\ ^{\circ}C$.

Connectivity test for a raft (Figure 24) is done before the EO test, to check all the channels working and to check all the parts including the sensors and three REBs (Raft Electronics Boards) were not damaged during the assembly.

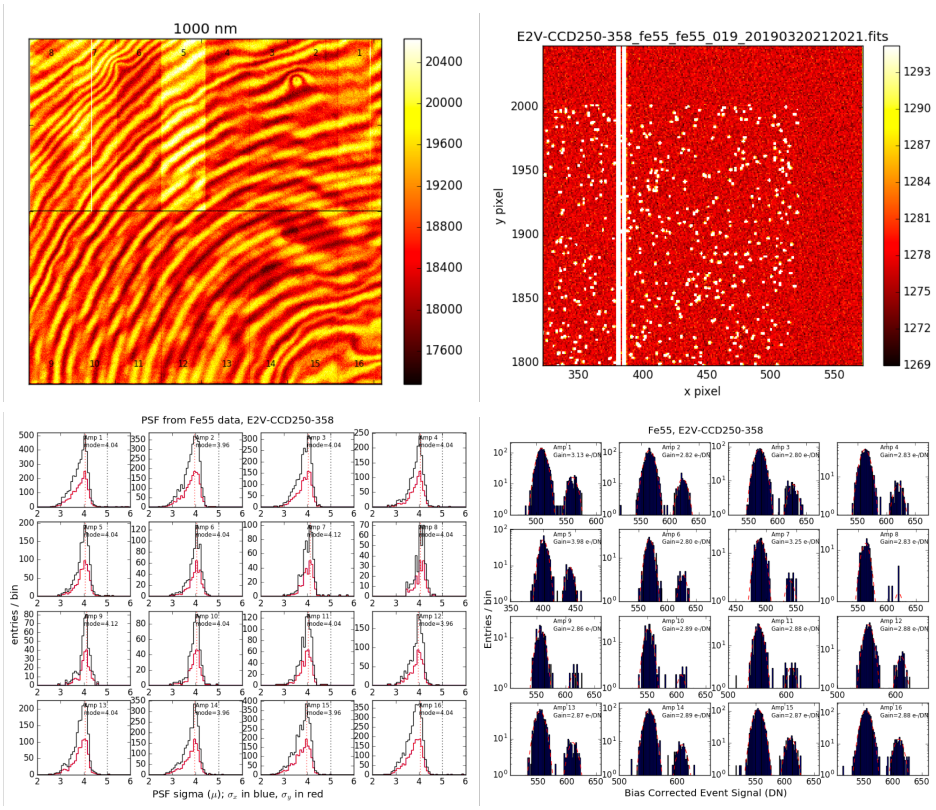


Figure 22: Top: Examples of flat image and Fe-55 image for single sensor EO. Bottom: Example of PSF and Fe-55 analysis using Fe-55 images taken for a single sensor EO.

## 2.6 TS4 : RSA assembly

BNL and SLAC are the main two laboratories involved in LSST camera building. At BNL, all of the 189 LSST production sensors are tested after the installation on a raft baseplate to build 21 RSA (Raft Sensor Assembly) and then a RTM (Raft Towel Module). Extra RTMs, two ETUs (Engineering Testing Units) and a spare, were also built at BNL. ETUs were built for construction validation purposes. Four corner rafts with three sensors on each raft were built at SLAC. After building 21 RTMs (and the spare RTMs), we test them for EO and metrology, then send them to SLAC. For the whole focal plane, 21 RTMs and 4 corner rafts will be assembled together at SLAC.

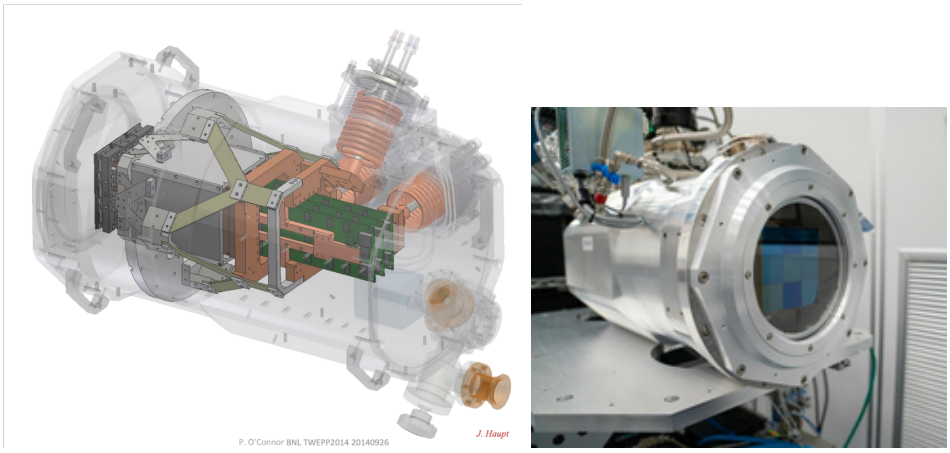


Figure 23: Left: Internal details of TS7 cryostat. Right: TS7 cryostat with a RSA (Raft Sensor Assembly) installed.

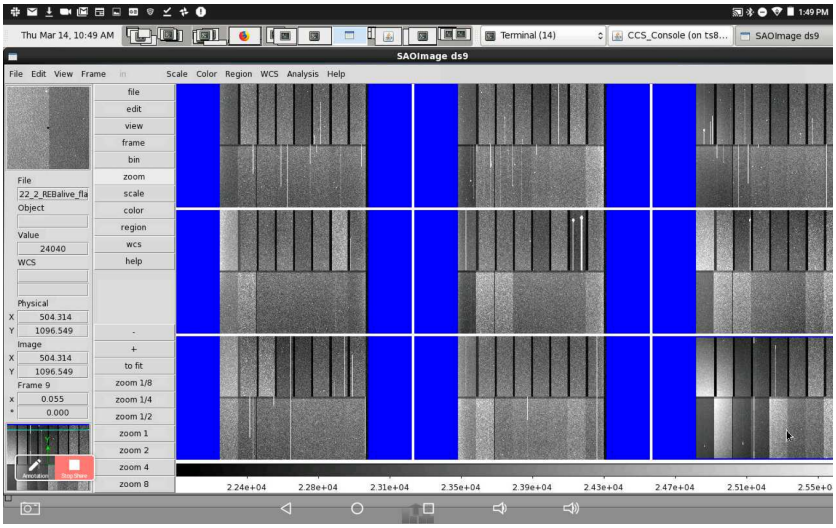


Figure 24: An example of a connectivity test image from a RTM.

(see Figure 25)

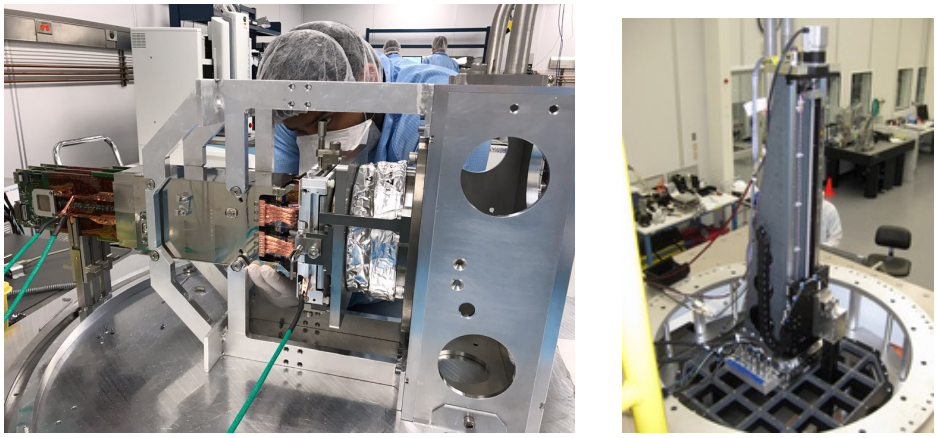

Figure 25: Left: Raft Towel Module (RTM) built at BNL. Right: RTM installed on focal plane base plate at SLAC.

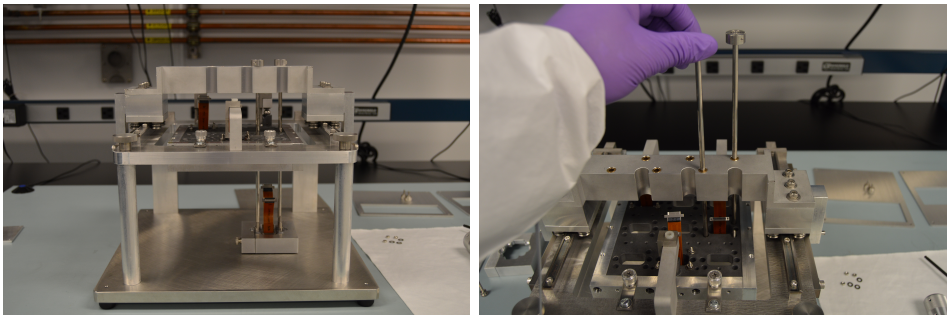

Figure 26: When installing sensors to assemble RSA (raft sensor assembly), sensor originally in a jig is moved to MF07 by pulling it out from jig, then it is connected to the baseplate (MF08) using MF06.

TS4 has a laminar flow hood for the cleanliness, so all assembly and disassembly activities are performed here. We use tools called MF07A (for e2v) and MF07B (for ITL) to grab a sensor, cover the sensor surface, and pull it out from the jig. These jigs are custom made from vendors to hold

the sensors while shipping and storing. When we assemble the RSA (Raft Sensor Assembly), nine sensors are installed on the baseplate (MF08) using a mechanical fixture (MF06). As shown in Figure 26, CCD control rods are used to connect three studs on the back side of the sensors. To prevent the parts falling out, especially during the shipping process, we stycast (bond) flux cables to the sensors, heating coils and nuts holding the sensor to the baseplate. After the RSA is built with nine sensors installed on the baseplate, we connect three Raft Electronics Boards (REBs) to the sensors. Three sensors are readout and controlled by one REB. The RTM structure is shown in Figure 27.

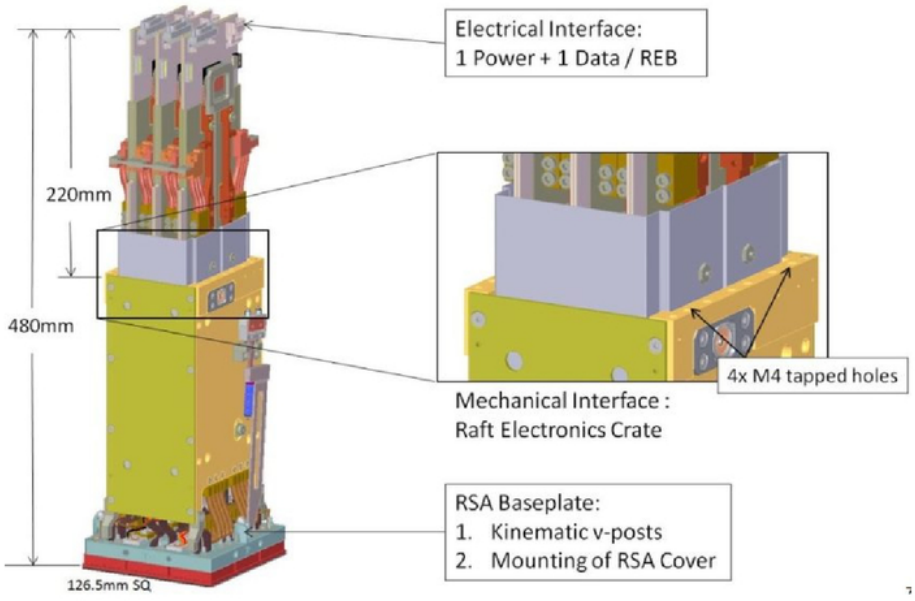


Figure 27: Structure of the RTM of LSST. Pictures adapted from T. Lange et al. [41].

# 3 Tree Rings

## 3.1 Introduction

Tree ring is one of the major sensor effects LSST is concerned about. The manufacturing process of growing a mono-crystal silicon boule leads to a circularly symmetric variation of dopant concentration. It results in a parasitic electric field in the direction orthogonal to the drift of photoelectrons causing a systematic displacement from their nominal trajectories, towards the CCD gates and also may lead to the position-dependent distortions of the point spread function (PSF)[9, 10]. Figure 29 shows the dopant variation, the transverse electric field and corresponding PSF shape as a function of position on the sensor normalized to the tree ring period. The effect will also result in the tree-ring-like pattern visible in images taken at uniform illumination. During the manufacturing, the silicon wafer is cut into four sensors and, therefore, there are four types of tree ring orientation, which depend on sensor position on the wafer. This position can be determined from information provided by vendors.

The tree rings have been previously studied for different types of LSST sensors and in different conditions [5, 9, 16]. In this study, for the first time, we used the full statistics of more than 200 sensors of LSST from both ITL and e2v vendors to systematically study the tree ring effect. We used the results of all available electro-optical tests for individual sensors and for the 21 LSST production Science Rafts, which included the datasets with various back bias voltage settings. In particular, we studied the tree ring amplitudes and periods (distance between the adjacent bright regions of the pattern) as a function of the radius (distance from the tree ring center), wavelength of the light source and back bias voltage.

Qualitatively, we expect the tree ring amplitude to increase and the period to decrease for larger radii, since the dopant concentration varies more in the outermost part of the wafer. The longer wavelength light penetrates deeper into the silicon and electrons move faster with higher back bias voltage. Therefore in both cases there is less chance for the electrons to deviate from the nominal path and to cause the tree ring effect. Thus we can expect that the tree ring amplitude will be smaller for longer wavelength and larger back bias voltage, while the tree ring pattern should remain unchanged as it is determined by the configuration of the transverse electric field.

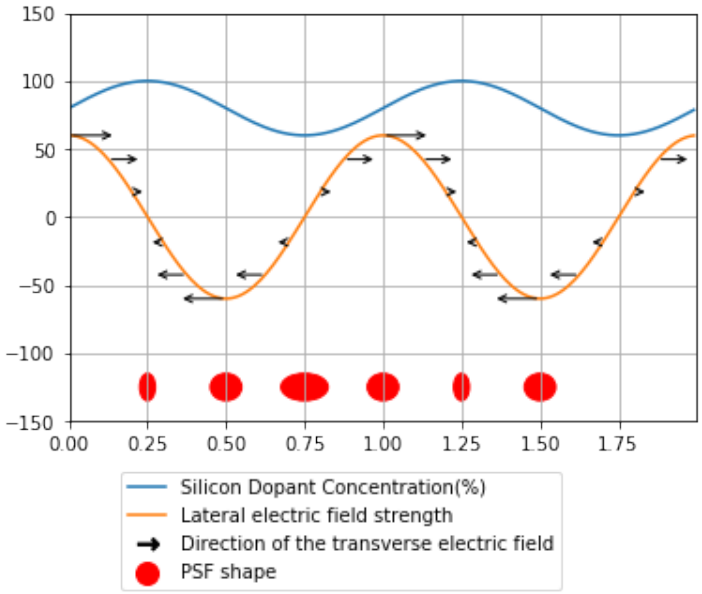


Figure 28: The tree ring effect caused by manufacturing process of silicon wafer. Shown are the dopant variation (blue curve), the transverse electric field (orange curve and black arrows) and corresponding PSF shape (red ellipses) as a function of the position on the sensor normalized to the tree ring period.

## 3.2 Methods

### 3.2.1 Reduction of flat images

We used "superflat" images to study the tree rings and to characterize their amplitudes and periods. Superflat image is a set of 25 images of the same exposure time, acquired at 500 nm (for the single sensor EO tests) and 625 nm (for the raft EO testing). Each sensor is composed of 16 segments, and the data includes an overscan region for each segment, which we used to remove the amplifier offsets. As we are interested only in relative variations of flat field intensity for the study of tree rings, we applied a FFT-based high-pass filter using AstroCCD code [53] to every segment, and then divided the result by the unfiltered image. Thus all the segments were converted to a common scale to show relative high-frequency variations. This approach is insensitive to both smooth variations of sensitivity over the segment, and

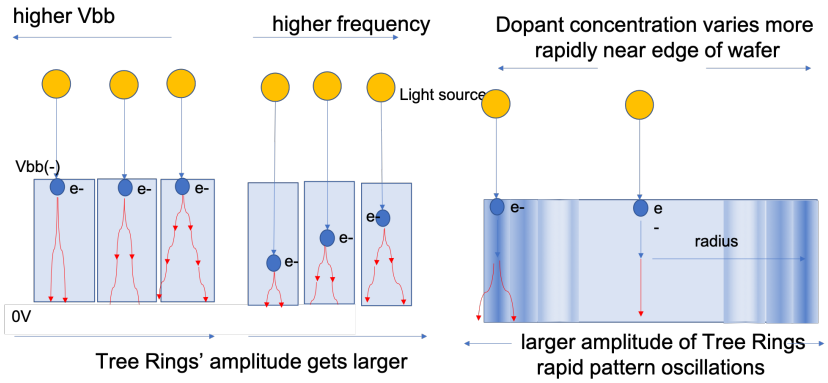


Figure 29: Tree Rings dependence on back bias voltage, frequency of the light, and radius.

also to the gain difference of different segments. Next, we assembled all 16 segments into a single image, and finally excluded from the analysis the regions with extended large-amplitude deviations mostly caused by the dust particles on the cryostat window.

### 3.2.2 Measuring amplitudes and periods of Tree Rings

For the centers of the tree rings we used the "center of the ring" method as in our previous study [5], as well as the automated method based on the minimization of the tangential variance [54], which provided very similar results. In our two papers ([5], [8]), we picked three points in one visible ring and calibrated the center of the ring that passes all three points. We have measured it several times for each die number and used the average position of the center in all sensors. The orientation of the pattern and position of the ring center according to the die location on the silicon wafer is shown in Figure 30.

Based on images of relative deviations derived from the superflats, and the ring centers, we constructed the mean deviation as a function of radius to reveal the radial pattern. The amplitude was calculated as a peak-to-peak difference by subtracting the amplitude of a lower peak from the amplitude of the previous higher peak in the pattern. Not to misidentify noise as a peak, we smoothed the pattern and introduced minimum and maximum distances to define adjacent peaks, see Figure 31 for comparison of the amplitude

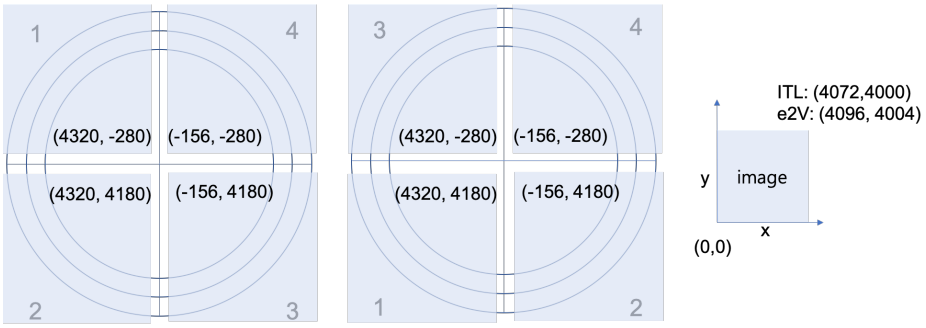


(a) (b)

Figure 30: Orientation of the tree ring pattern and position of the ring center in the image, according to die number for (a) e2v and (b) ITL.

pattern before and after the smoothing procedure. Since the tree ring amplitude increases with radius (corresponding to the regions near the edge of the wafer) and maximum amplitude on the very edge of the sensor is noisy and inconsistent among different sensors, we measured the median amplitude in the radius range of 5400-5600 pix.

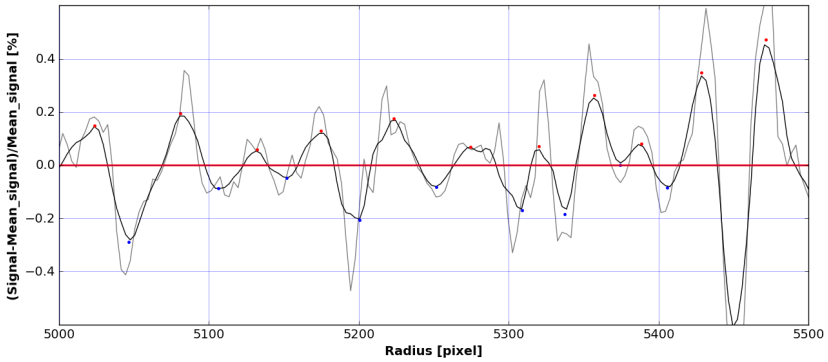


Figure 31: We used smoothing and defined minimum and maximum distance between the neighboring peaks, to avoid considering noise as peaks.

## 3.3 Results

### 3.3.1 Radius dependence

We expect the silicon resistivity variation, responsible for the tree ring pattern, to be larger for the larger radii, which is in agreement with the evidence of the tree ring amplitude increasing towards the outer part of the silicon wafer [5]. With more statistics, we can characterize it by fitting the radial profile of intensity variations with a second-order polynomial starting from the radius of 4000 pixels.

As shown in Figure 32, the tree ring amplitude starts to increase around the radius of 4000 pixels. In this figure the 0V back bias voltage data was used to see a dramatic increase in the amplitude. Collecting all 189 LSST production sensors used to build 21 Science Rafts with back bias voltage of 50V, we have fitted 2nd order polynomial function with minimum at 4000 pixels. For ITL and e2v separately, mean fitted functions are shown in Figure 33.

The radial profile of deviations clearly shows a quasi-periodic structure with the period decreasing towards larger distances from the ring center. To characterize it, we constructed a position-resolved periodogram using radially sliding window with 500 pixels size [54]. The upper panel of Figure 34 shows an example of such periodogram for an e2v sensor represented as a two-dimensional map with horizontally stacked Lomb-Scargle periodograms [42] corresponding to a given radius. The lower panel of the same Figure displays the periodograms at several radii, revealing a clear radial evolution of the peak corresponding to the dominating period from $\sim$100 pixels in the center of the chip to $\sim$50 pixels at the far edge.

The radius-resolved periodogram shown in Figure 34 clearly shows that the primary period of the tree rings evolves with radius, becoming shorter towards the edge of silicon wafer. This behaviour is seen for all CCDs we studied, both of e2v and ITL types. To characterize typical periods of oscillations we decided to estimate them at a fixed radius, chosen to be 5500 pixels from the tree rings center. We used the position of the primary periodogram peak as an estimator for the period. The distribution of periods over all experiment runs is shown in the upper panel of Figure 36. The dependence of the periods on the back bias voltage is shown in the lower panel of the same Figure 36. The periods for e2v and ITL chips differ slightly, but mostly remain in the range between 55 and 65 pixels, and do not show any

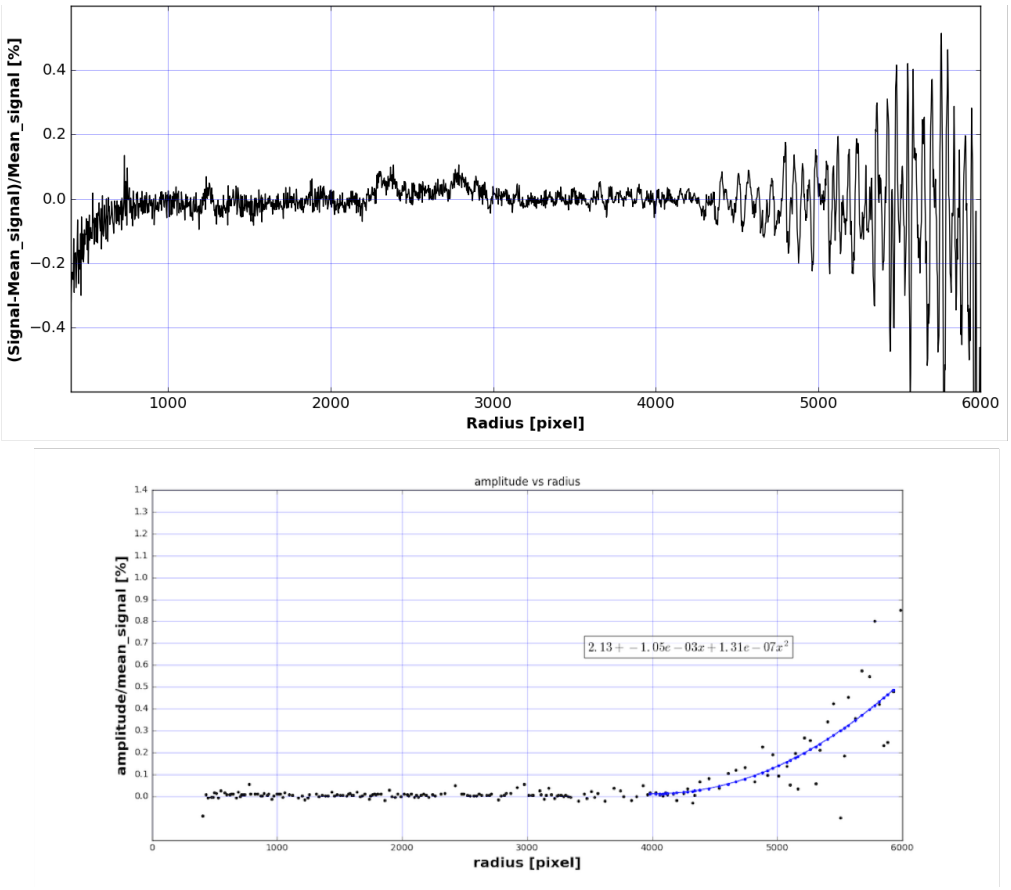


Figure 32: Amplitude of Tree Rings increase as radius gets larger. Top: The signal on radius from the center of the rings. Bottom: Peak-to-peak amplitude on radius. Blue line shows a second-order polynomial fit.

dependence on the back bias voltage.

There is, however, a subset of sensors from both vendors, displaying oscillations about twice as fast. To better understand that difference, we are showing in Figure 37, side by side, examples of "slow" (period of ∼60 pixels) and "fast" (period of ∼40 pixels) oscillations, both as periodograms and as original variations of intensity around the 5500 pixels radius. It is clear that the general behaviour is the same for both, but the "fast" case is dominated by a few closely placed tree rings. Both cases display a number of components

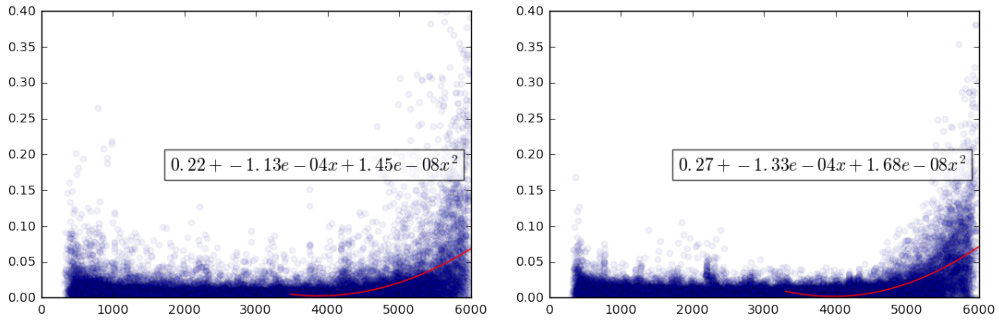


(a) (b)

Figure 33: Average 2nd order polynomial function for all 189 production sensors of LSST, with back bias voltage -50 V (a) ITL (B) e2v.

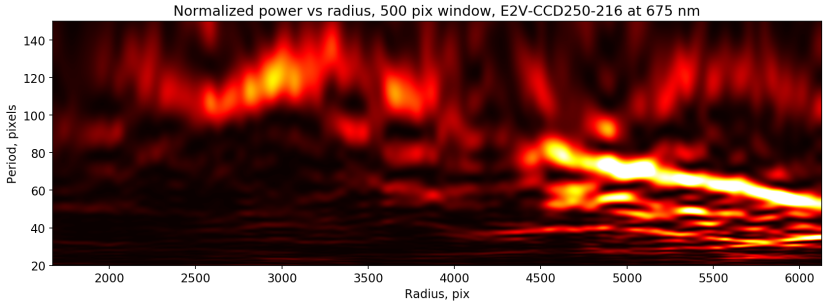


Figure 34: An example of the radius-resolved tree ring periodogram in an e2v sensor. The change of primary period with radius increase is clearly seen.

with different distances between the peaks of 30 and 70 pixels with different amplitudes. We conclude that the difference between the "fast" and "slow" cases can be attributed to the natural variability of the tree ring pattern that can have fast oscillations starting from the period of 30 pixels.

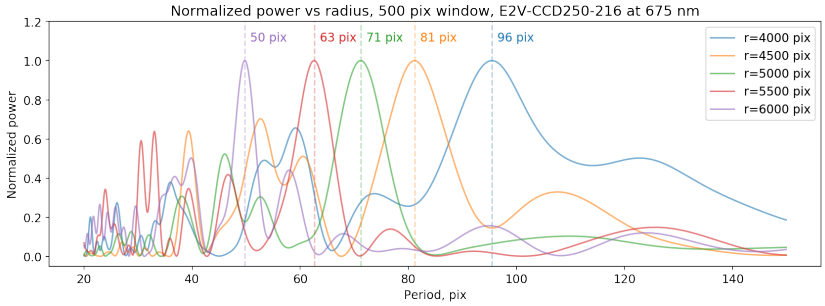


Figure 35: Lomb-Scargle periodograms [42] of the tree rings for the same sensor on several radii, with marked positions of the primary peak, which drifts to lower periods towards the edge of silicon wafer.

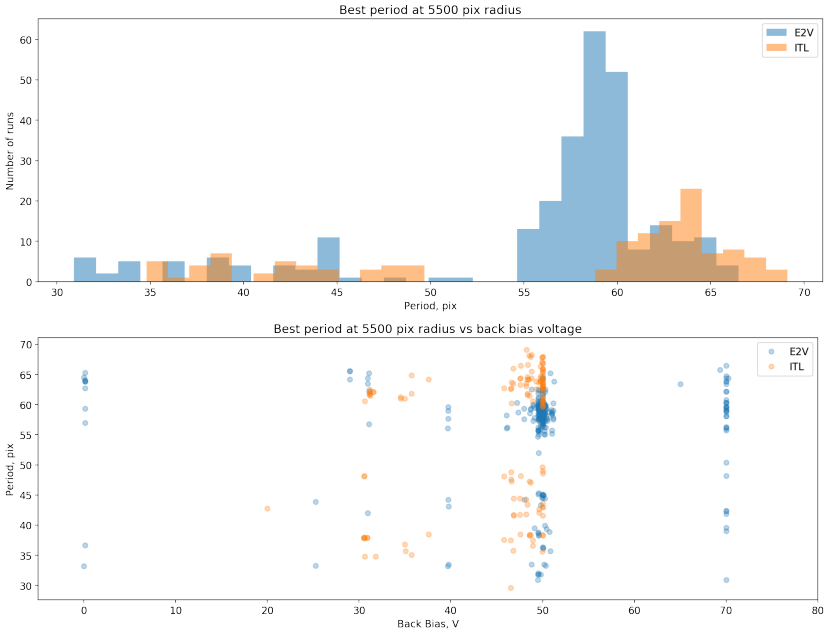


Figure 36: Top: distribution of best Tree rings periods measured at 5500 pixels radius using position of primary peak of periodogram for all runs we studied. Bottom: dependence of these periods on back bias voltage.

### 3.3.2 Wavelength dependence

We expect that the amplitude of the tree rings gets smaller at longer wavelengths because these photons convert deeper in silicon so the respective

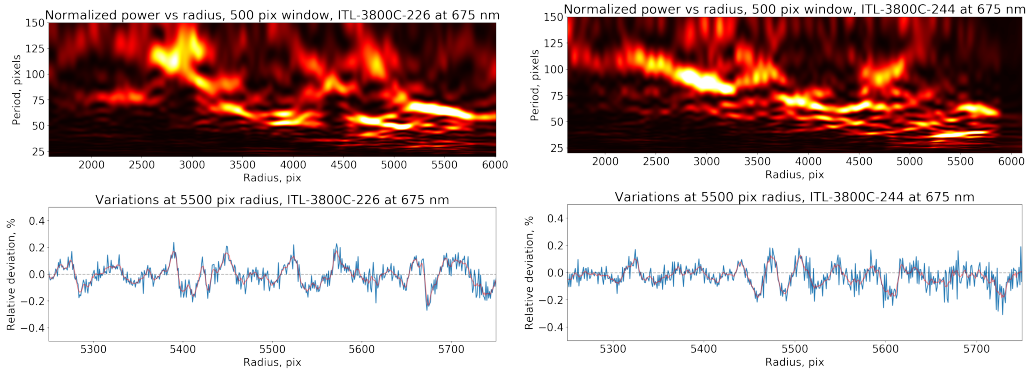


Figure 37: Radius-resolved periodograms for ITL chips displaying "slow" (∼60 pixels period, left panel) and "fast" (∼ 40 pixels period, right panel) oscillations at around radius of 5500 pixels. Lower panels display the relative deviations curve around this radius.

photoelectrons have less distance to drift hence less chance to deviate from their nominal paths [5].

Structures in the 320 nm image are explained by much shorter penetration of UV light into the sensor, which then becomes more sensitive to the surface unevenness. Fringes in IR originate from the varying thickness of the silicon wafer. In the shorter wavelength region, before fringes start to dominate, the tree rings are visible, caused by variation in the wafer resistivity as discussed before. Fringe pattern starts to dominate over tree rings around 880 nm and shows maximum impact around 970 nm. Therefore we chose 375 nm, 500 nm, 625 nm, 750 nm, and 875 nm in the first paper in 2017 [5] to see the wavelength dependence on Tree Ring amplitude.

We used datasets for two ITL rafts (total nine sensors each) with the illumination wavelengths 400nm, 500nm, 600nm, 700nm, and 800nm to study dependence of the tree ring amplitude on the wavelength. The short wavelength light (below 400nm) is sensitive to non-uniformities of the sensor surface, and fringe patterns dominate the tree ring pattern at long wavelengths (above 900nm), so these datasets were not used for this study. We found that the pattern did not change leading to conclusion that the period does not depend on the wavelength. However the amplitude of the tree rings decreased from 0.052% (400nm) to 0.042% (800nm) as expected though the change was not very significant. Mean and median amplitudes with back

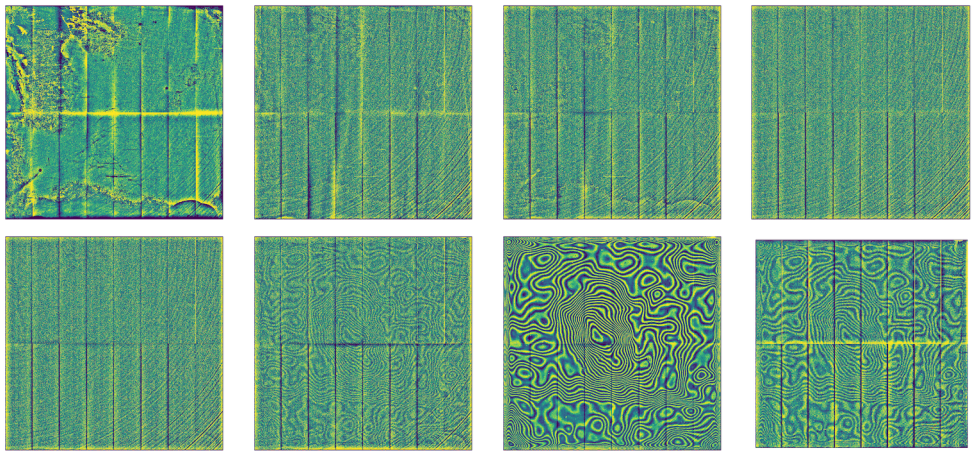

Figure 38: Uniformly illuminated images for the sensor ITL-3800C-017 taken at different wavelengths: 320, 400, 540, 770, 850, 900, 970, and 1080 nm (from top-left to bottom-right) with 35V of back bias voltage.

bias voltage 50V at radius 5500nm is shown in Figure 39 as a function of the wavelength. Figure 40 compares the tree ring pattern for the same sensor at different wavelengths, illustrating that the pattern itself does not change.

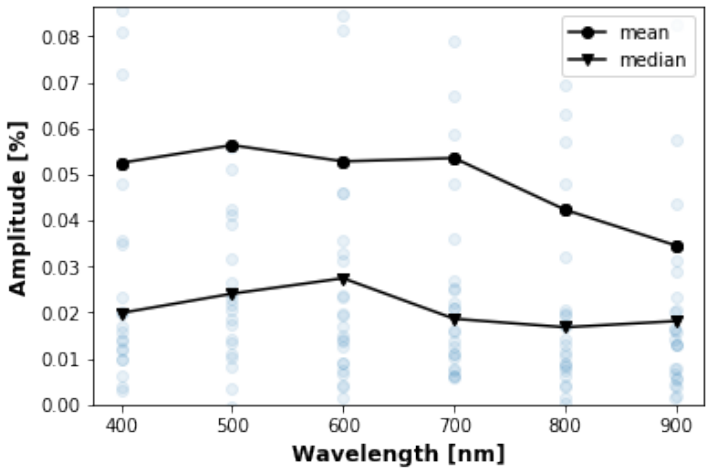


Figure 39: Tree Rings amplitude as a function of wavelength at radius 5500 pixel and with back bias voltage 50 V.

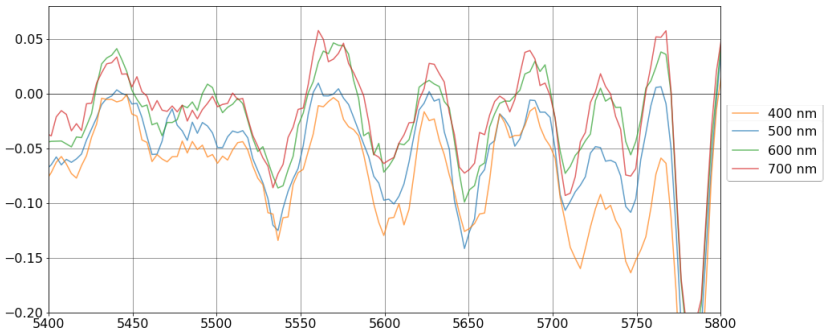


Figure 40: Tree Rings pattern doesn't change with wavelength. Period of Tree Rings does not depend on wavelength.

### 3.3.3 Back bias voltage dependence

The back bias voltage drives electrons to the CCD gates in the sensor. The electrons drift faster with higher back bias voltage and have less deviations so the tree ring pattern is the most pronounced for small values of the voltage as illustrated in Figure 41.

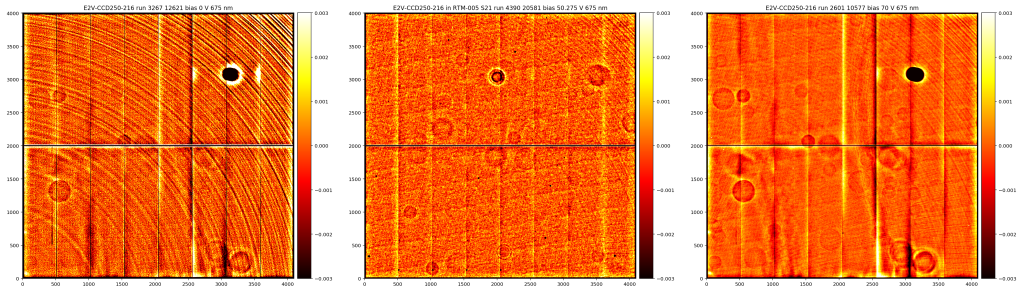

(a) (b) (c)

Figure 41: Tree ring pattern of e2v-CCD250-216 with different back bias voltage settings: (a) 0V (b) 50V (c) 70V.

Tree ring amplitude decreases from 0.075% (27V) to 0.03% (70V) for e2v and from 0.4% (35V) to 0.04% (50V) for ITL as shown in Figure 42, which is based on the superflat data for a large sample of sensors with 500nm wavelength taken at BNL and SLAC.

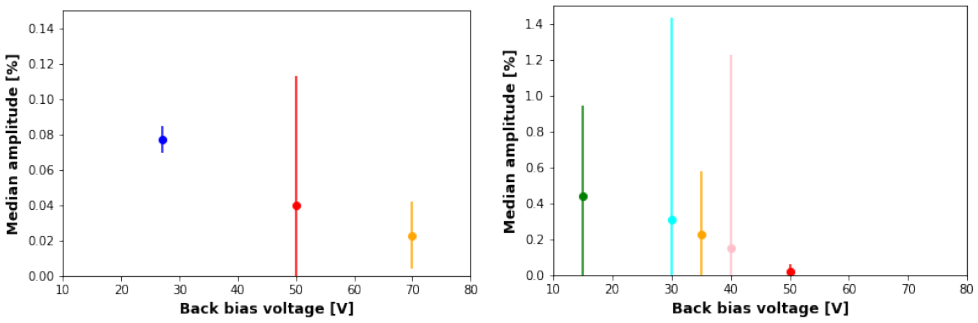


(a) (b)

Figure 42: Tree rings amplitude with different back bias voltage settings: (a) median amplitude for each back bias voltage settings of e2v sensors. (b) median amplitude for each back bias voltage settings of ITL sensors. The error bars correspond to standard deviations of the amplitude values.

At last, Figure 43 shows the raft EO test results for all 21 rafts tested at BNL (189 sensors) with back bias voltage 50V and 500nm wavelength. 50V and 70V are the nominal back bias voltage settings for ITL and e2v. Figure 43-(a) shows the results with the nominal back bias voltage showing what we can expect in real LSST observations. Figure 43-(b) shows the results of e2v and ITL with same back bias voltage of 50V showing e2v and ITL will have similar Tree ring amplitude at 50V.

## 3.4 Conclusion

We used the full statistics of the LSST production sensors to study one of the major sensor effects called tree rings. We have determined that the tree ring amplitude gets larger for the larger radii, smaller wavelength and smaller back bias voltage. The period between the patterns decreases away from the center of the rings and does not depend on the wavelength and back bias voltage. With the suggested back bias voltage settings that LSST will use, 50V for ITL and 70V for e2v, we measured that the average tree ring amplitude of 0.03 % for the e2v and 0.04 % for the ITL sensors, and period of 60 pixels near the radius of 5500 pixels.

These results can be used as inputs to the LSST simulations tools: PhoSim [36], imSim and GalSim [34], to determine how significant the astrometric

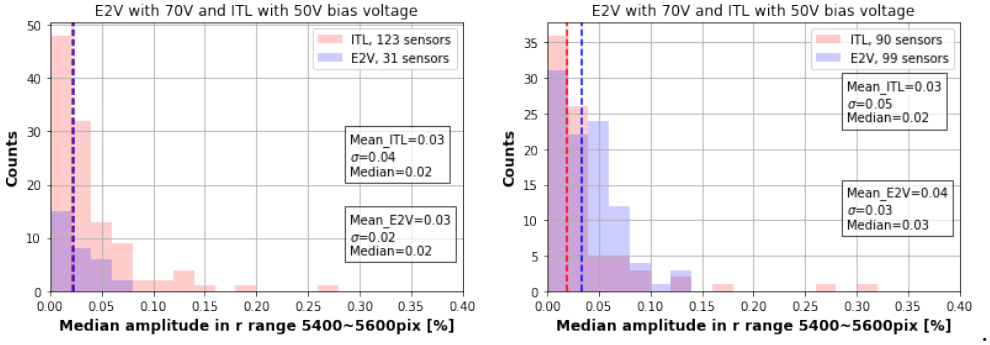


(a) (b)

Figure 43: Median amplitude for radii in the range 5400∼5600pix for e2v and ITL with (a) proposed back bias voltage settings: 70V(E2V) and 50V(ITL) and (b) both 50V of back bias voltage.

shifts and shape distortions from the tree rings may be and what effect they may induce for measurements of various cosmological observables.

All the 21 raft images (189 sensors) of Tree Rings for the whole focal plane of LSST using BNL raft EO data taken by February 2019 with 50 V of back bias voltage and -90 C temperature settings are shown in Appendix A.

# 4 Charge Transfer Efficiency

## 4.1 LSST Sensor Design

As mentioned earlier, each CCD sensor of LSST has 4 k x 4 k pixels (4000 pix by 4072 pix for ITL and 4004 pix by 4096 pix for e2v - size in pixels are written in order of y axis by x axis) and 4 cm x 4 cm size. Each sensor is divided into 16 segments and all the segments collect data at the same time with a readout time of 2 seconds [12].

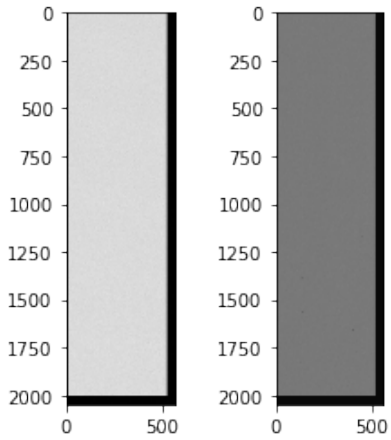


Figure 44: An example of pre-scan and over-scan region in one segment. Black region shows pre and over-scan and brighter part is the main image region for e2v (left) and ITL (right) sensors.

In the output image files from the EO tests, there are "pre-scan" and "over-scan" regions before and after the main imaging area. As shown in Figure 44, each segment has its own pre- and over-scan region. When we collect information from pixels, we move electrons pixel by pixel from one column (row) to the next column (row). Even after transfering 4k colums and 4k rows, we collect extra columns and rows to collect left over electrons, and we call these extra area "overscan" regions (see Figure 44). Similarly, we call extra columns (rows) collected before imaging area "prescan".

For ITL, there are 3 pixels before and 50 pixels after the main image region in x axis and 48 pixels after the main image region in y axis. For e2v,

pre-scan has 10 pixels on the x axis and over-scan has 50 pixels and 46 pixels for x and y axis. Here x axis is in the direction of read-out.

With the pre-scan and over-scan, each segment of e2v and ITL gets an image size of (2048, 572) pix and (2048, 562) pix when the photon collection area is of size (2002, 512) pix and (2000, 509) pix. Figure 45 shows the orientation of each amplifier following the direction of the read-out.

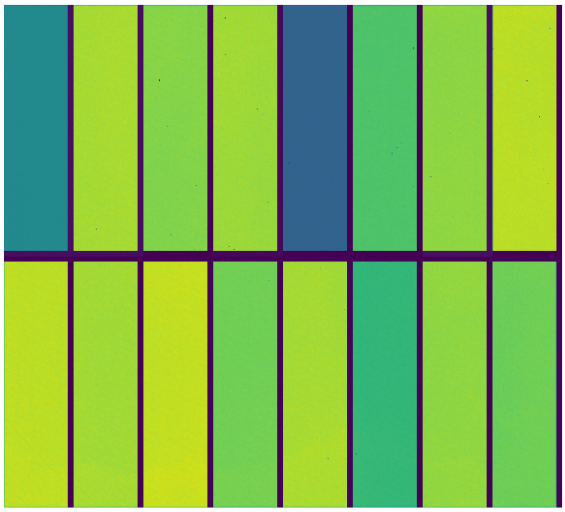

Figure 45: A full sensor image including pre-scan and over-scan region in the coordinates of each amplifier according to the position of the origin and read-out. The color indicates flux on flat image, showing pre-scan and over-scan as the dark area on the edge of each segment.

## 4.2 Charge Transfer Efficiency

During the readout, information on each pixel's potential well is moved one pixel by one pixel, in the serial direction and in the parallel direction towards the output node [25]. As shown in Figure 46, electrons in each pixel flow to next pixel due to potential changes.

Charge Transfer Efficiency (CTE) or Charge Transfer Inefficiency (CTI) is one of the specification needed to check the quality of the sensor, measuring ratio of the electrons remaining behind when transferring electrons from one

column to the next column or from one row to the next row. They are called as "serial CTE (HCTE: Horizontal CTE)" and "parallel CTE (VCTE: Vertical CTE)" accordingly.

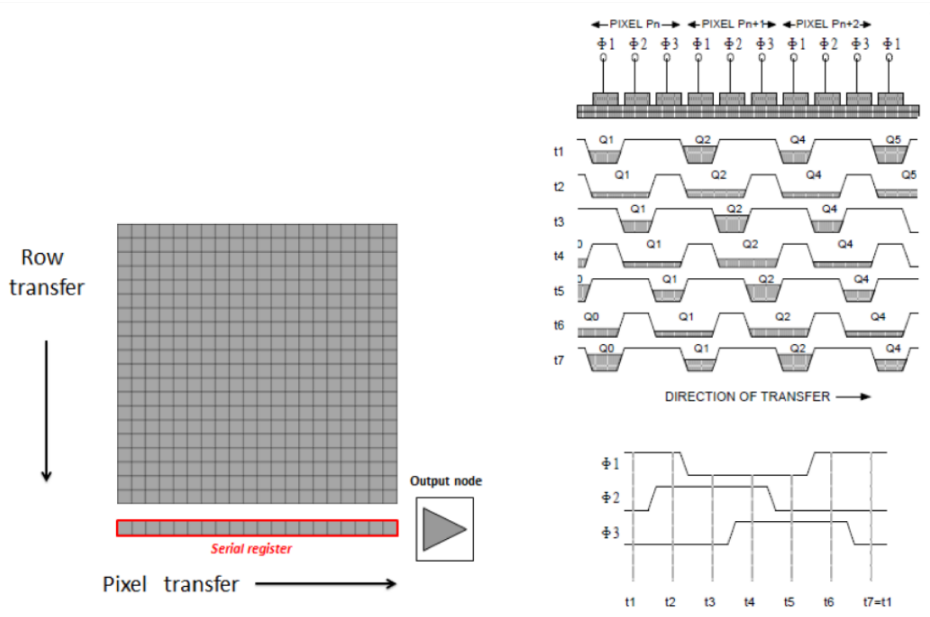


(a) CCD frame transfer (b) Three-phase parallel transfer

Figure 46: CCD readout process [25].

## 4.3 Methods

### 4.3.1 Extended Pixel Edge Response (EPER)

The Extended Pixel Edge Response (EPER) method uses the overscan region we mentioned above. We use the first two columns (rows) in the overscan region and compare them to the last column (row) of the imaging region. CTE is calculated as:

$$CTE = 1 - \frac{F_0}{F_i N_i} = 1 - CTI \tag{46}$$

where $N_i$ is the number of image columns (rows) plus the number of prescan columns (rows), $F_i$ is the sum of all pixels in last imaging column and $F_0$ is

the sum of all pixels in first and second overscan columns (rows) after the last imaging column (row).

### 4.3.2 Fe-55 X-ray Transfer

This method is using Fe-55 images to see its linear relation between signal and number of pixels transferred. X-ray exposure image shown in Figure 47 is taken for LSST sensor testing for multiple purposes including gain calibration. We can use this for shape distortion study as a comparison to the simulation, in Chapter 6.

Fe-55 hits have two peaks in wavelength due to $K_\alpha$ and $K_\beta$ X-rays of 5.9 keV and 6.5 keV emitted as shown in Figure 48.

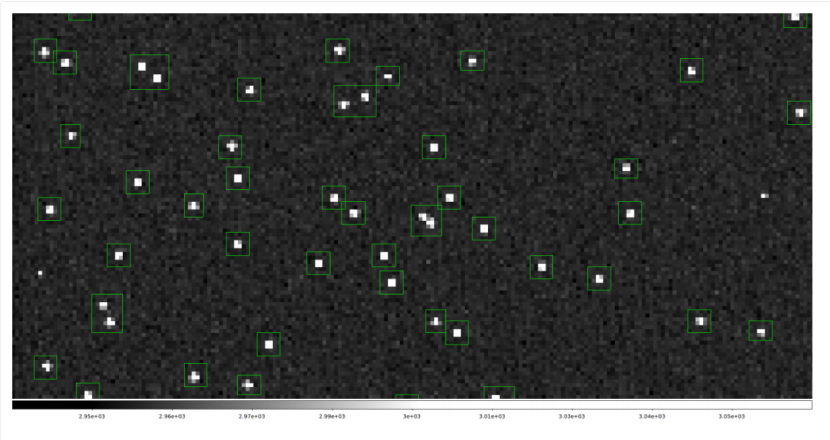

Figure 47: Footprints found in X-ray exposure image [47].

Since $K_\alpha$ peak is larger, we are measuring signal of 5.6 keV, which is about 1600 electrons with the gain calibration of LSST sensors. Due to electrons left behind, flux of Fe-55 hit points will decrease as larger number of pixels transferred. The CTE as measured by X-rays is defined with Equation (47), where $X$ is the X-ray signal and $S_D$ is the average charges loss after $N_P$ pixel transfers,

$$CTE = 1 - \frac{S_D}{XN_P} = 1 - CTI. \tag{47}$$

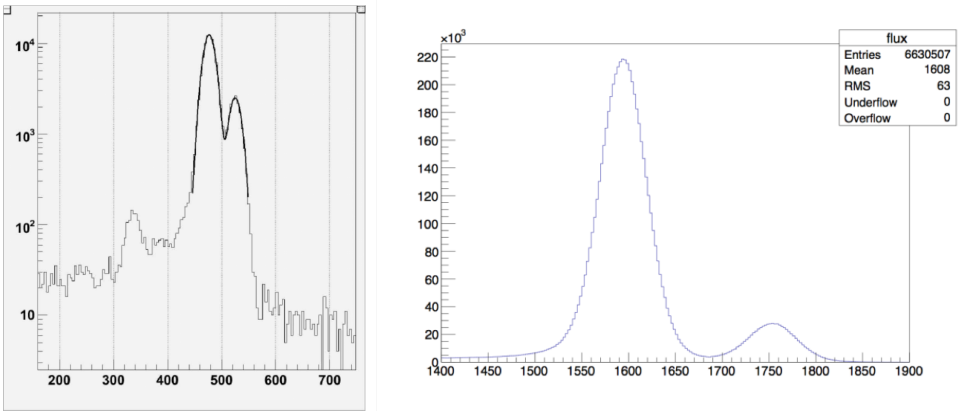


Figure 48: Left: Fe=55 X-ray spectra with fit to $K_\alpha$ $K_\beta$ lines. It shows the number of events on each cluster amplitude in ADU [44]. Right: Distribution of measured flux in electrons[47]

### 4.3.3 Other methods

Charge in Variance in Flat field (CVF) uses flat fields to measure the relation between variance and column (row) number. It requires two flat images and two bias images. The variance of the signal of the line $i$ can be expressed as:

$$\begin{aligned}\sigma_e^2(i) =& a^{2i}N_e + \binom{i}{1}^2 a^{2i-2}b^2N_e + ... + \binom{i}{i-1}^2 a^2b^{2i-2}N_e \\ =& a^{2i}N_e + O(b^2)\end{aligned} \tag{48}$$

where $N_e$ is the number of electrons, $a$ is CTE, $b$ is CTI, and $O(b^2)$is the residual. Here $O(b^2)$ is much smaller than $a^{2i}N_e$.

Using $CTI = 1 - CTE$, variance can be written as Equation (49), and Equation (50) in ADU (Analog Digital Unit) with $g$ for gain [6].

$$\sigma_e^2(i) = N_e - 2ibN_e + O(b^2) \tag{49}$$

$$\sigma_a^2(i) = \sigma_{a0}^2 - 2b\sigma_{a0}^2 i + O(b^2) \tag{50}$$

Using two flat images and two bias images, we make new image R as:

$$image\ R = \frac{flat1 - bias1}{flat2 - bias2} < flat1 - bias1 > \tag{51}$$

then we can calibrate CTE by:

$$\begin{aligned} \sigma^2_{flat,i} =& \frac{\sigma^2_{R,i}}{2} = \mu - \nu i \\ CTE =& 1 - \frac{\nu}{2\mu} \end{aligned} \tag{52}$$

where $\mu = \sigma^2_{a0}$ and $\nu = 2b\sigma^2_{a0}$.

## 4.4 Results

### 4.4.1 CTE in LSST

LSST specifiation for CTE requires both e2v and ITL sensors to have HCTE (Serial) $1 - 5 \times 10^{-6}$ and VCTE (Parallel) $> 1 - 3 \times 10^{-6}$. HCTE has a soft specification limit of $1 - 30 \times 10^{-6}$. For the EO (Electro Optics) test, LSST used EPER method to calibrate serial and parallel CTE. BNL has tested all 21 RTMs (Raft Tower Module) and measured CTE of every segment. Both e2v and ITL sensors are 4k x 4k pixel format, with 16 amplifier segments of 512 X 2k pixels.

Median CTI of all 189 LSST production sensors measured was $1.6 \times 10^{-6}$ for HCTE and $0.6 \times 10^{-6}$ for VCTE [52]. The serial and parallel CTI values for all 3024 segments of 189 CCD sensors in 21 RTMs are shown in Figure 49. Green shows e2v and orange shows ITL.

We could check that most of the segments satisfy the soft specification limit of the serial CTI of $30 \times 10^{-6}$, and the median CTI passes the hard specification limit, $5 \times 10^{-6}$. In average, the serial CTI for twelve e2v rafts was $(1.52 \pm 6.6) \times 10^{-6}$ and for nine ITL rafts was $(2.07 \pm 45) \times 10^{-6}$. ITL sensors had larger variance in EO parameters including CTI as shown in Table 1.

Mean parallel CTI of twelve e2v rafts and nine ITL rafts are $0.02 \times 10^{-6} \pm 1.13 \times 10^{-6}$ and $0.75 \times 10^{-6} \pm 23 \times 10^{-6}$. Both satisfy the VCTI limit of $3 \times 10^{-6}$.

CTE will vary with back bias and clock rail voltages [51]. We have used -50V as a back bias voltage in these tests.

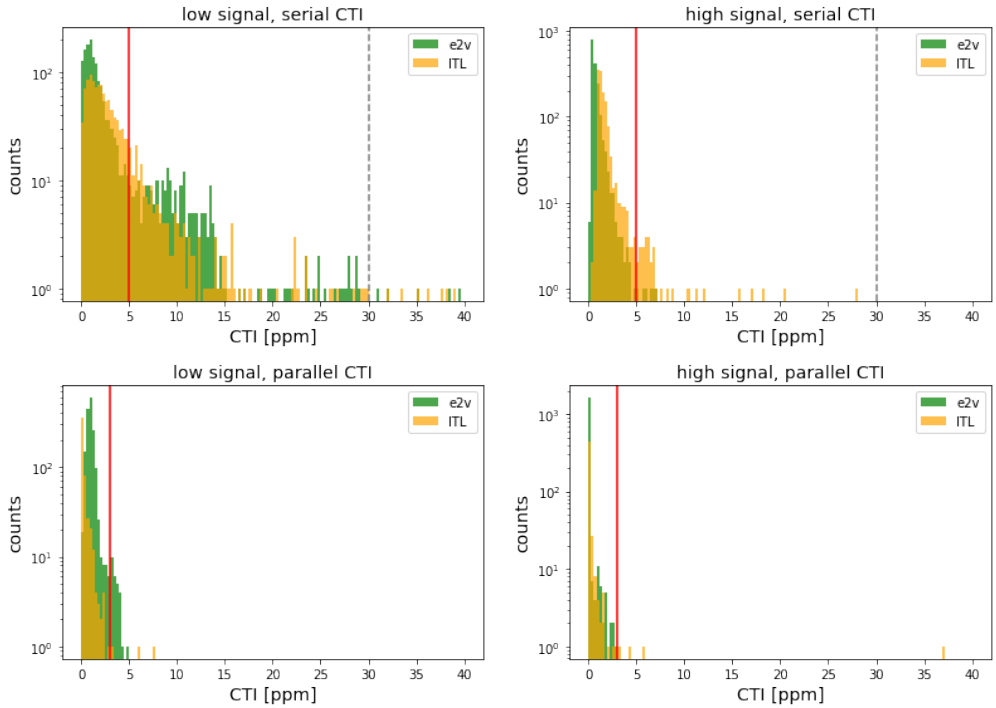


Figure 49: Histogram of serial (top images) and parallel (bottom images) CTI results: e2v (green) and ITL (orange). Dashed line indicate hard (red) and soft (grey) specification limits. The left images are CTI results from the low signal images and the right images are from the high signal image.

### 4.4.2 EPER and Fe-55 methods comparison

We have studied three methods to measure CTE, which are EPER, X-ray Transfer and CVF. All three have small correlation, although they do not differ much. Figure 50 shows CTE values calculated with three different methods, for ITL-3800C-001 in 2016.

## 4.5 Conclusion

Three methods of CTE measurements, the EPER, Fe-55, and CVF, were compared and show no correlation. From the Elecro Optics (EO) tests on all 189 LSST production sensors, we conclude that the average CTE values are $1 - 0.6 \times 10^{-6}$ for vertical direction and $1 - 1.6 \times 10^{-6}$ for parallel direction.

| Parameter | $\overline{e2v}$ | $\overline{ITL}$ | $\sigma_{e2v}$ | $\sigma_{ITL}$ | unit |
|---|---|---|---|---|---|
| QE-u | 69.8 | 62.2 | 6.3 | 7.8 | % |
| QE-g | 89.9 | 88.4 | 2 | 3.4 | % |
| QE-r | 95.6 | 94.3 | 2.4 | 3.4 | % |
| QE-i | 95.1 | 99.4 | 3.6 | 4.4 | % |
| QE-z | 84.2 | 92.7 | 2.4 | 4.6 | % |
| QE-y | 25.9 | 31.5 | 3.5 | 4.2 | % |
| read noise | 4.7 | 6.1 | 0.23 | 1.8 | e-rms |
| gain | 0.69 | 0.94 | 0.034 | 0.11 | e-/ADU |
| full well | 144 | 186 | 8 | 40 | ke- |
| dark current 95 % | 0.013 | 0.038 | 0.03 | 0.048 | e-/pix/s |
| diffusion PSF | 4.12 | 4.48 | 0.14 | 0.28 | um rms |
| CTI-serial | 1.52 | 2.07 | 6.6 | 45 | ppm |
| CTI-parallel | 0.02 | 0.75 | 1.13 | 23 | ppm |

Table 1: Population statistics for all LSST Science Rafts [52]. $\sigma$ indicates a standard deviation.

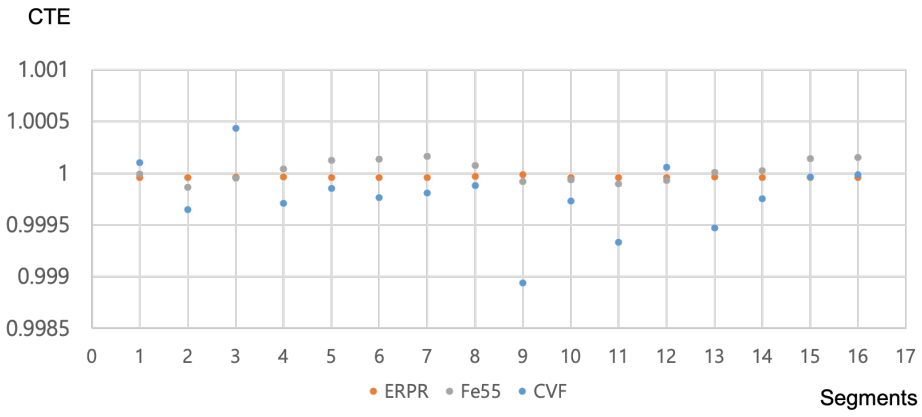


Figure 50: Comparing three different methods of calibrating CTE values.

These are the results calculated by EPER method.

We will rely on CTE values from EPER method, but Fe-55 images can be used to compare shape distortion from CTE in real data and in the sim-

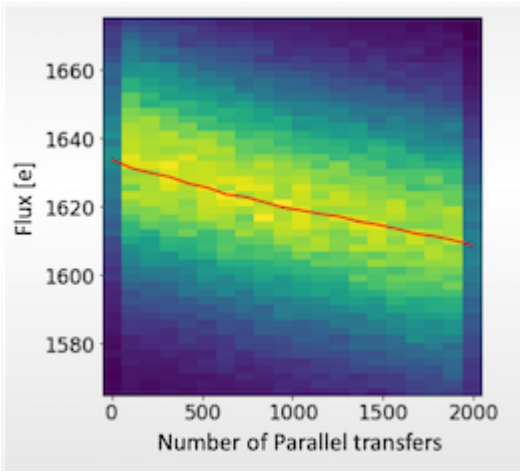


Figure 51: CTE measurement with Fe-55 method. It shows the flux decreasing as the number of pixels transferred increases. The figure is adapted from the A. Christov [61].

ulations in the Chapter 6. For the PhoSim and GalSim simulations in Chapter 6 will also uses the EPER CTE values to see expected shape distortion due to CTE from the LSST sensors. The shapes of the circular sources are expected to become more elliptical in vertical and horizontal directions when VCTE and HCTE decreases, due to more electrons left behind in the direction of electron transfer.

# 5 Photometric Redshift and De-blending

Collaboration between the photo-z estimation (PZ) and Large Scale Structure (LSST) working groups of DESC has the official project on developing tools to estimate photo-z better and to de-blend merged objects [13]. In this study we will talk about photometric redshift estimation and truth-coadd catalog matching for DC2.

## 5.1 Photometric Redshift

There are two techniques used by astronomers to measure a redshift: Photometry and Spectroscopy. LSST uses photometry with u, g, r, i, z, and y bands.

Spectroscopy uses a spectrometer to spread light into its wavelength, in order to see the emission and absorption lines to distinguish atoms and molecules of the observed object. The intensity, width and position of the spectral lines give information about the object's temperature, density, and motion.

On the other hand, LSST has five filters to separate the light into the range of the wavelengths broadly. CCDs measure the flux of the light at each color (wavelength range) and photometry uses their pattern, including information of the Quantum Efficiency (QE) of the sensor and the amount and ratio of the light on each band, to estimate the redshift. As shown in Figure 52, LSST uses the pattern of transmission curves to calibrate photometric redshifts.

LSST Project has defined specific photo-z requirements as listed in the Science Requirements Document (SRD) [7] for a sample of galaxies with magnitude in i band less than 25, in $0.3 < z < 3.0$.

Mainly driven by LSS group of DESC needs:

(a) RMS scatter $\sigma_z/(1+z) < 0.03$ for individual galaxies, meaning the Gaussian distribution of the photo-z should fit in the $0.03(1+z)$ limit.

(b) the bias must be $\delta < 0.003$ (1+z). It means the systematic uncertainty in the mean redshift of each tomographic bin, the photo-z bin of the source galaxies by using the depth information, should be less than $0.003(1+z)$.

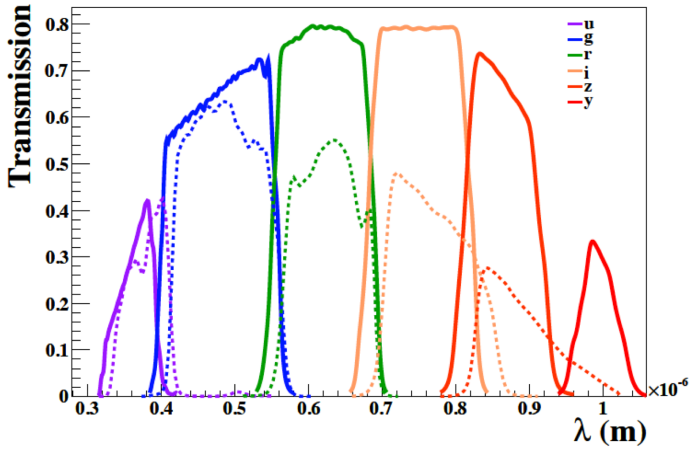


Figure 52: Image adapted from [15] showing an example of photometric redshift calibration. LSST transmission curves shown by the solid lines and CFHTLS transmissions shown by the dashed lines. The transmission includes the transmission of the filter itself, the expected CCD quantum efficiency, and the telescope optical throughput.

## 5.2 Blending

Blending means multiple objects overlapping due to faint objects merged by a bright object nearby, or due to a blurred image with high noise. As mentioned by Dawson et al. [24], there are three classes of blends, according to how significant the blending affects properties of the objects. If two or more objects are detected as a single object, we call it "ambiguous blends". When they are detected as individual objects, we call it "conspicuous blends". Lastly, "innocuous blends" means that overlap brings very small changes. Ambiguous blends are most concerning. LSST will be observing deeper than any other survey, which means the projected surface number density of objects in a field will increase, and therefore it will have worse systematic uncertainty with object blending. Object blending will depend on the point spread function (PSF), object projected separation ($\theta$), object surface brightness profiles, pixel noise background level, and object number surface density (n).

Blended object will increase noise in the mass distribution since it will cause errors in counting the number of objects and their position. It will

also increase shear noise not only because merged objects will have different shape, but also because fainter objects are neglected from shear analysis. Therefore, de-blending these objects is very important in simulation, as well as in real observation, to reduce the noise when measuring galaxy mass and shape distribution.

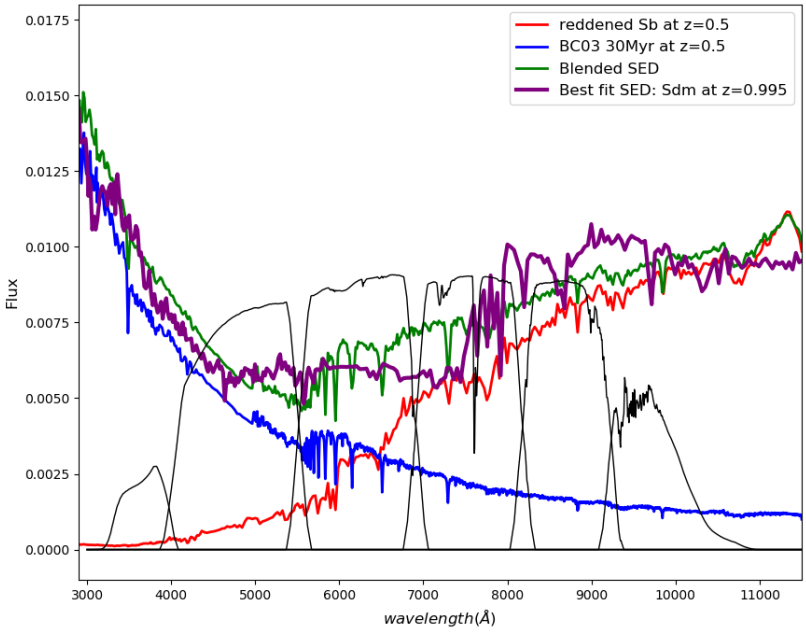


Figure 53: When two objects with redshift z = 0.5 (red and blue lines) are blended, calibration of photometric redshift on a merged output object (green line) will turn out to be very different, z = 0.995 (purple line).

When objects are blended, it brings significant change in redshift estimation. For example, when two objects both with a redshift of 0.5 are blended, the redshift of a detected object is estimated to be 0.995 (see Figure 53).

Thus blended objects can cause serious error in redshift estimation. We are going to compare the spec-z of input objects and photo-z of output objects in DC2 simulation to show how significantly the blended objects affect the photo-z estimation. The PZ (photo-z) and LSS (large scale structure)

working group of DESC started to work together to improve photometric redshift estimation and de-blending, with DC2 (Data Challenge 2) truth (input) and coadd (output) catalog matching.

### 5.2.1 Power Spectrum

From the flux information of six bands, the covariance matrix and inverse covariance matrix of the band averaged P(k) can be produced to find the value to minimize $\chi^2$. Estimating the covariance matrix and the inverse covariance matrix accurately is crucial for both spectroscopic and photometric surveys for cosmological parameter estimation. In this study we are going to see how precise photometric redshift calibration can be done. Due to the issue with the color information in DC2 1.2 catalog, the study of how photo-z estimation will correlate with blending and power spectrum will be discussed later with 2.1 catalogs. The tool development for the photo-z estimation and input-output catalog matching will be handled in this paper as a preparation for the new version, 2.1, of the DC2 catalogs.

## 5.3 Methods

### 5.3.1 FoF matching for DC2 catalogs

We used Friends of Friends (FoF) matching algorithm to compare input (truth) and output (coadd) catalogs of DC2. Input and output catalogs mean the catalogs used for the p and i simulations. We used 1.1p, 1.2i and 2.1i for the coadd catalogs. Here the number on catalog name means the version of the simulation and "p" and "i" notations mean that the coadd catalogs are from the PhoSim and ImSim, respectively. FoF matching put all the objects from input and output together on the same page and group them by minimum distance to nearby (friend) objects. Then we bin the groups by the number of input objects to number of output objects in each group. Schematic for FoF matching is shown in Figure 54.

When we apply FoF matching, a perfect match will lie on the n_input = n_output group, blended objects will have n_input > n_output, and mis-detected objects will be in n_input < n_output group. We chose [1-1], [2-1] and [1-2] groups to represent perfect match, possible blended objects, and possible mis-detected objects.

We also applied filters to the coadd catalogs to cut out the magnitudes

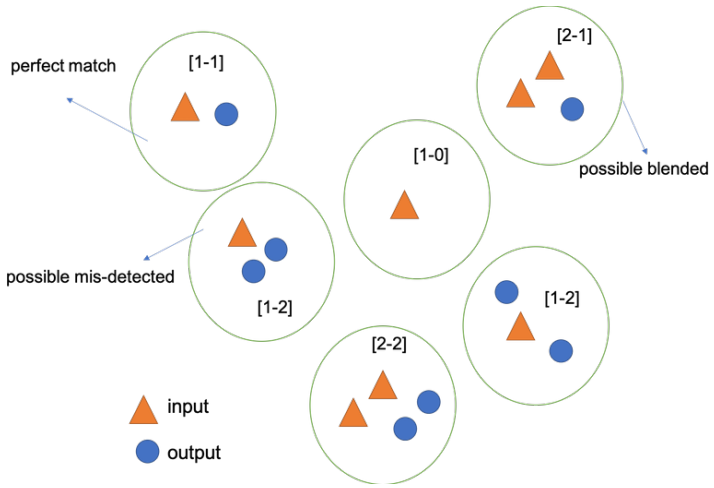


Figure 54: Diagram showing how FoF matching works.

larger than 25.5, and applied Subaru Hyper Suprime-Cam (HSC) lensing cuts based on the HSC survey paper [30]. Options for lensing cuts are shown in Table 2. The change of the number of objects in the output catalog due to each of lensing cut filters will be discussed in 5.4.

### 5.3.2 MLZ and BPZ

MLZ (Machine Learning for photo-Z) is a photometric redshift estimation tool developed by M. C. Kind [46] [60]. On MLZ there are four main variables that change run time and precision of photo-z estimation: NTree, NRandom, Natt and MinLeaf. Total number of trees is NTree x NRandom. NRandom is the number of random realizations and NTrees means the number of trees or maps. We gave six bands of information as Att (attribution): u, g, r, i, y, z, u-g, g-r, r-i, i-y, y-z, eu, eg, er, ei, ey, and ez. “e” before each band means error. Natt is the number of attribution randomly chosen from the Att list. ”MinLeaf” is the minimum number of terminal leaf satisfying in each tree. Increasing NTree, NRandom and Natt will increase run time but output of photo-z estimated will be more precise. Larger MinLeaf will reduce run time.

BPZ is the tool developed by S. Schmidt for LSST-DESC to do photometric redshift estimation. While we are developing BPZ and DC2 to proceed to 2.1 catalogs, we will focus on 1.2i results and MLZ in this study.

| Quantity | Meaning | Option |
|---|---|---|
| i_modelfit_CModel_instFlux | flux of filter i | not nan |
| ext_shapeHSM_HsmShapeRegauss_resolution | resolution from HSM gaussian shape measurement | not nan |
| ext_shapeHSM_HsmShapeRegauss_e1 | e1 from HSM gaussian shape measurement | not nan |
| ext_shapeHSM_HsmShapeRegauss_e2 | e2 from HSM gaussian shape measurement | not nan |
| i_SN_cmodel | Signal to noise on filter i | >= 10 |
| detect_isPrimary | Primary object | True |
| deblend_skipped | deblending process skipped | False |
| base_PixelFlags_flag_edge | List of flags which cause a source to be rejected as bad | False |
| base_PixelFlags_flag_interpolatedCenter | | False |
| base_PixelFlags_flag_saturatedCenter | | False |
| base_PixelFlags_flag_crCenter | | False |
| base_PixelFlags_flag_bad | | False |
| base_PixelFlags_flag_suspectCenter | | False |
| base_PixelFlags_flag_clipped | | False |
| ext_shapeHSM_HsmShapeRegauss_flag | | False |
| HSM_res | residulas of HSM | >= 0.3 |
| HSM_ell | ellipticity of HSM | < 2.0 |
| ext_shapeHSM_HsmShapeRegauss_sigma | sigma of HSM gaussian shape measurement | <= 0.4 |
| mag_i_cModel | magnitude of filter i | < 24.5 |
| base_Blendedness_abs_instFlux | absolute flux of blendedness | $< 10^{0.375}$ |

Table 2: Lensing cut option based on HSC [30].

Both tools train the catalogs with known spec-z, to categorize the pattern of the flux in six bands. The best fit of the pattern in the test catalog will be matched to the trained categories.

## 5.4 Results

### 5.4.1 Flux comparison for each groups

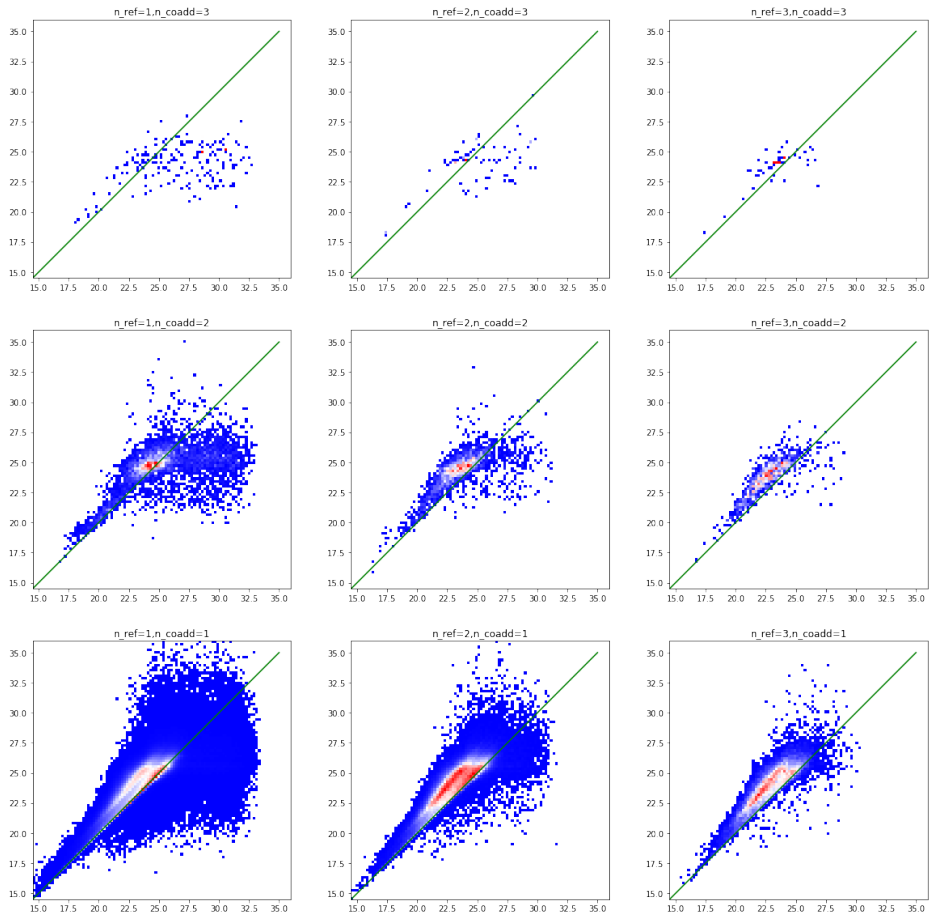


Figure 55: Total magnitude (from total flux) comparison in FoF bins without raw catalog with lensing cut filters. FoF matching length = 1.0 arcsec was used.

In Figure 55, 56, and 57, example of the flux of truth object(s) and the

flux of coadd object(s) comparison is shown for each FoF bin. Figure 57 had lensing cut filters applied and we can check that magnitude $< 25$ was applied. If there are multiple objects either in truth or coadd catalogs, we have used maximum flux or the total flux calibrated by multiple objects' magnitudes. As expected, possible perfect match in the [1-1], [2-2], and [3-3] groups showed counts lying on the diagonal line, meaning the flux of input object matches with the flux of output object.

In order to define deblending efficiency, if the separation between the truth and coadd objects is less than 0.4 arcsec and the difference between the i filter magnitude of truth and coadd object is less than 0.3, we declared it as a good match. With this definition, 1.2i had overall a success rate of 26 % without lensing cuts. The catalog 1.2i had magnitude problem compared to 1.1p which had overall a success rate of 71 %.

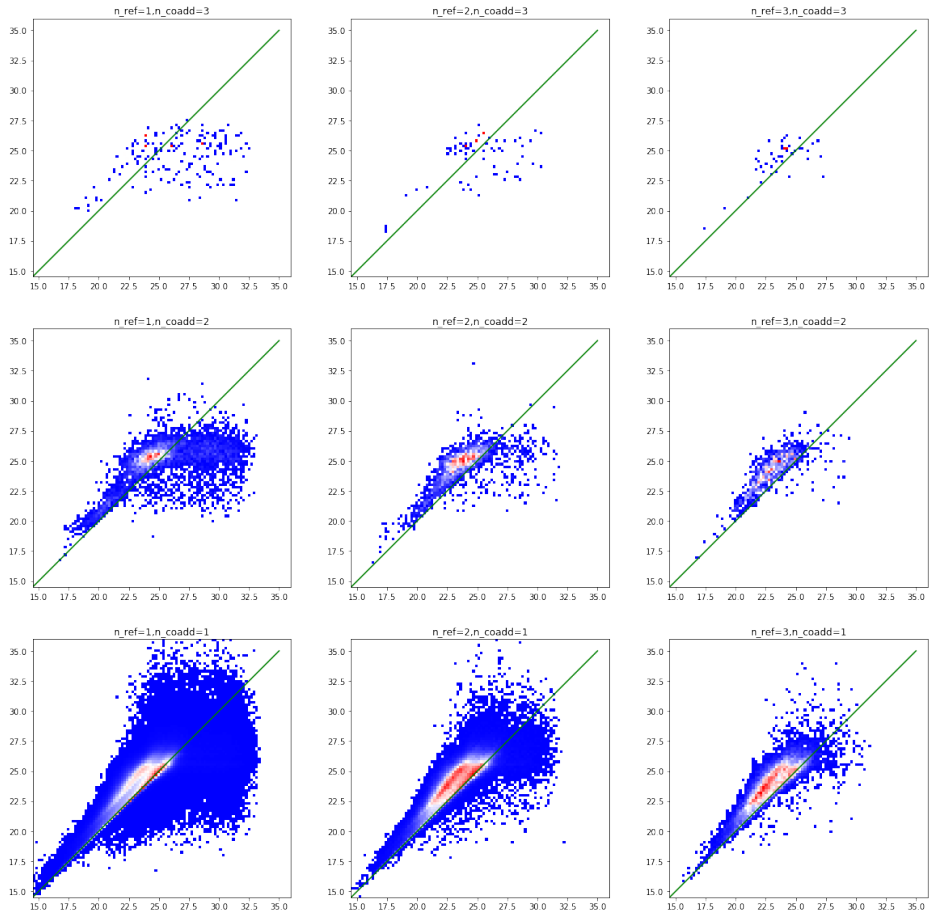


Figure 56: Minimum magnitude comparison in FoF bins with raw catalog without lensing cut filters. FoF matching length = 1.0 arcsec was used.

### 5.4.2 The lensing cut filters on the output catalog

Applying the lensing cuts on the coadd (output) catalog one by one following the Table 2, we have compared the number of objects in the coadd catalog. As shown in Figure 59, we could check that option of $HSM_{ell} < 2.0$ affects the most, while 6th to 14th options don't change much in the number of objects.

With all filters of HSC lensing cuts, number of coadd objects decreases and ratio of each group changes as shown in Figure 58. We have also compared the number of output objects in the [1-1] and [2-1] groups with each

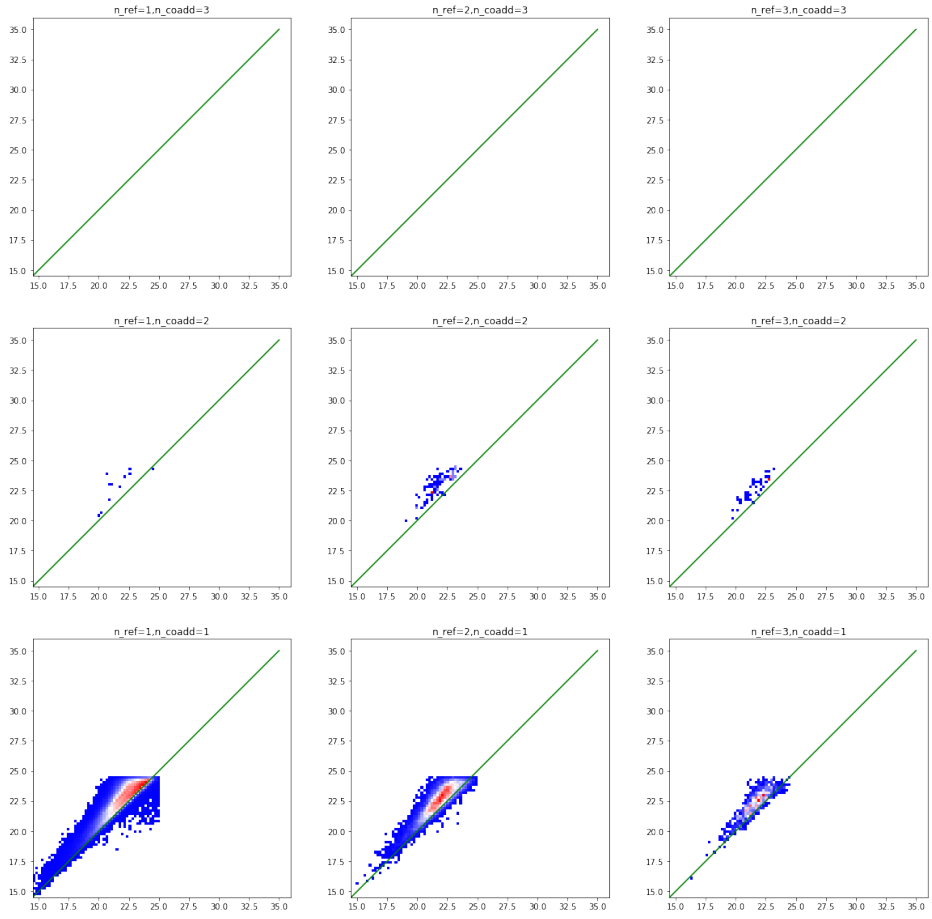


Figure 57: Minimum magnitude comparison in FoF bins with raw catalog with lensing cut filters. FoF matching length = 2.0 arcsec was used.

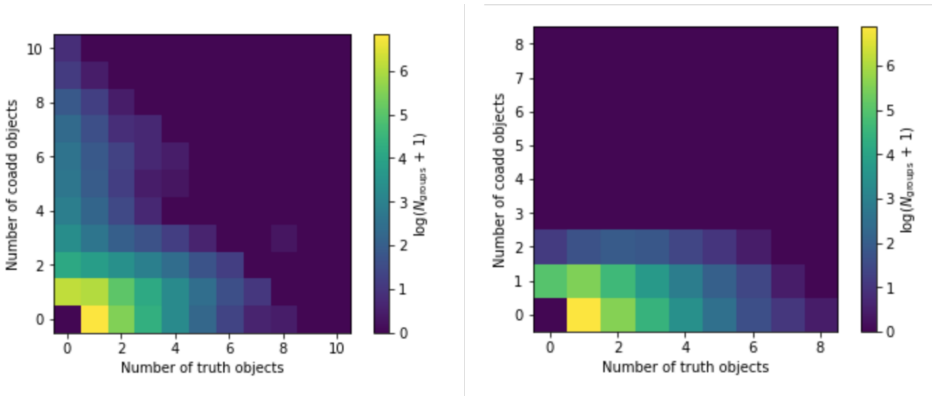


Figure 58: 2d histogram showing number of each groups [0-0] to [10-10]. Left: without any cuts. Right: with all lensing cut options applied.

option applied separately. Figure 60 shows the result with orange circular marks for [1-1] and green star marks for [2-1].

### 5.4.3 MLZ with various options

We ran MLZ with a few different combinations of NRandom, NTree, NAtt, and MinLeaf. Increasing NRandom, NTree and NAtt multiplied running time, and MinLeaf decreased running time and accuracy. Due to large dataset we are using, we used a large MinLeaf to reduce the running time, since we expect a small variance in the terminal nodes. As suggested by the MLZ builder, M. C. Kind, we used NRandom = 6, NTrees = 10, NAtt = 5, and MinLeaf = 10. Comparison between photo-z and spec-z with different options of NRandom, NTrees, NAtt, and MinLeaf are shown in Figure 61. These options affected the time of running and the accuracy of the result. (6, 5, 6, 100) took 8 hours to run, (2, 5, 5, 100) took 2 hours 30 minutes, and (2, 2, 5, 10) took 53 minutes.

### 5.4.4 Perfect match of 1 truth : 1 coadd and 2 truth : 2 coadd

In Figure 62, we compared estimated photo-z of coadd object with spec-z of truth object, then in the bottom images we showed mean and standard deviation at each spec-z.

For the two truth objects and two coadd objects in [2-2] group, we have

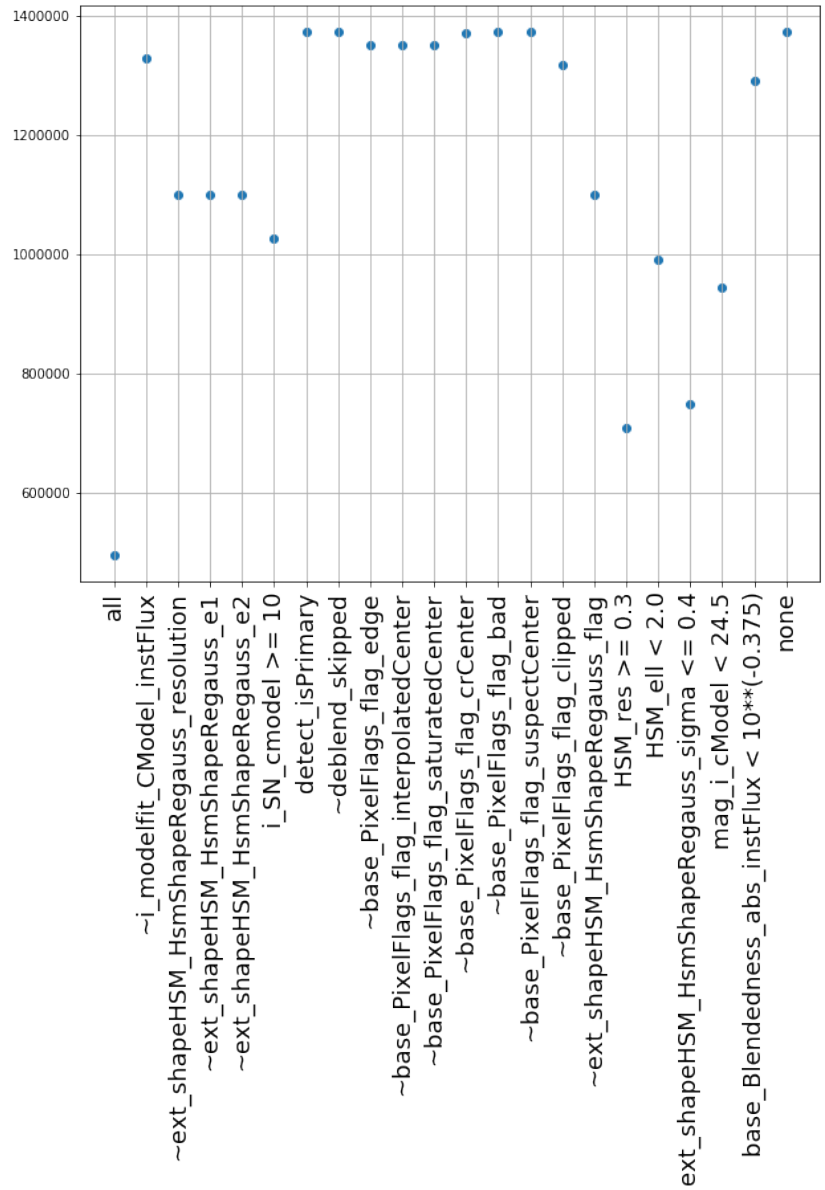


Figure 59: The number of output catalog objects with each option of lensing cut filters applied one at a time.

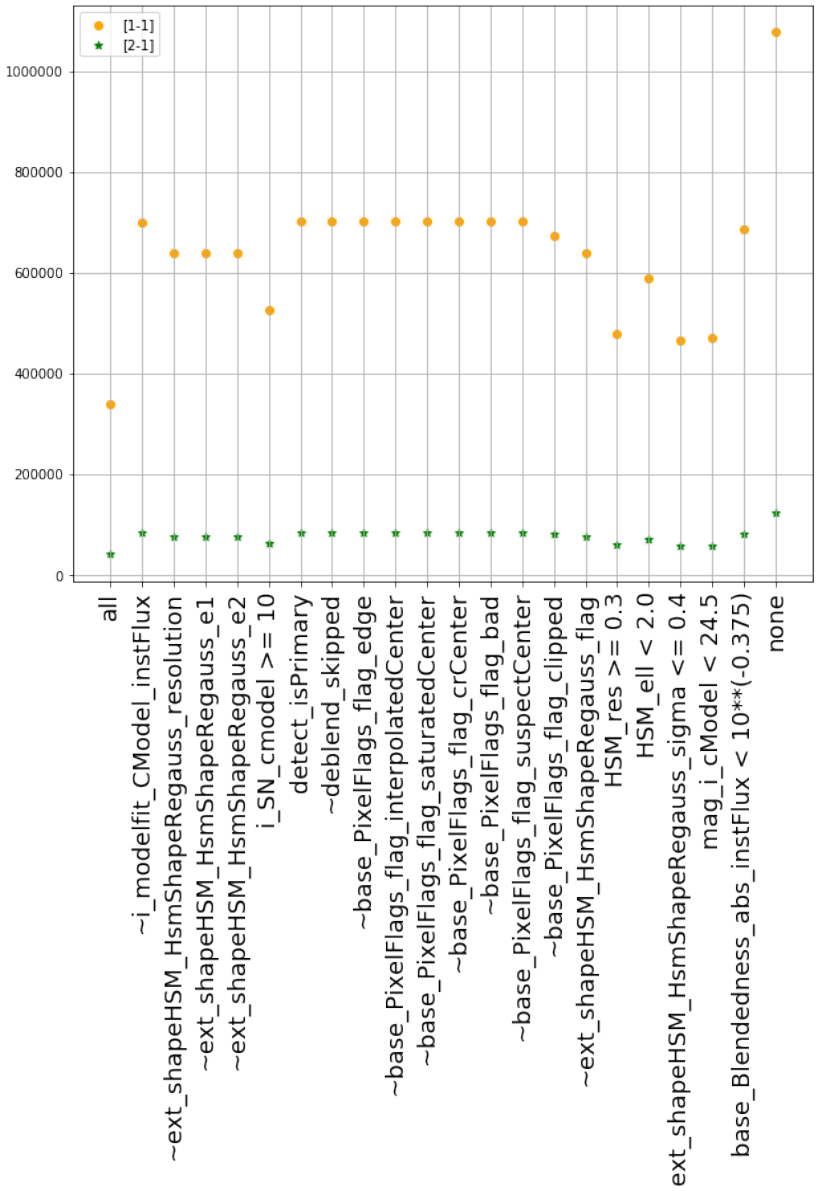


Figure 60: a
nd [2-1] groups]The number of output catalog objects in [1-1] (orange) and [2-1] (green) groups with each option of lensing cut filters applied one at a time.

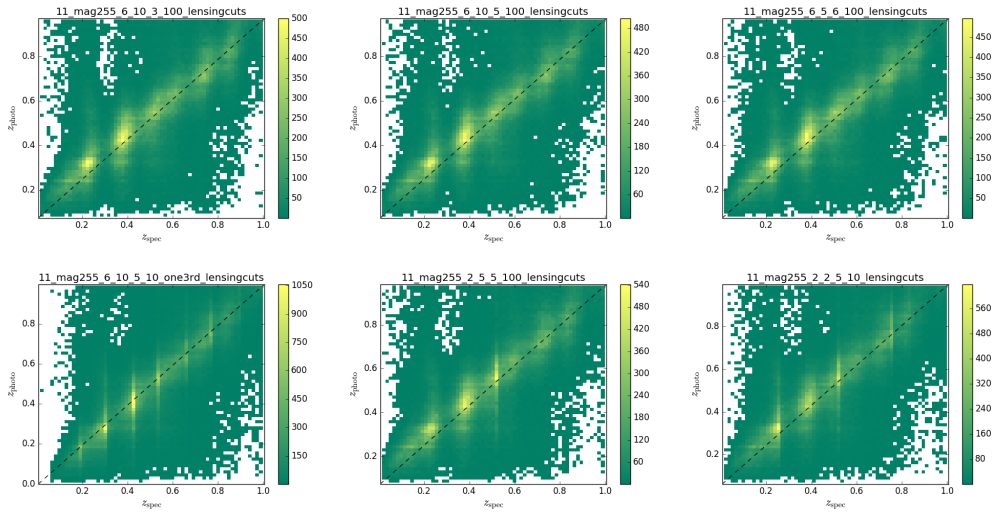


Figure 61: Photo-z estimation with MLZ for 1 truth : 1 coadd object group. The images show pdf plots comparing spec-z of truth objects and photo-z estimated. Lensing cuts were applied to these results. From top left to bottom right, NRandom, NTrees, NAtt and MinLeaf were (6, 10, 3, 100), (6, 10, 5, 100), (6, 5, 6, 100), (6, 10, 5, 10), (2, 5, 5, 100), and (2, 2, 5, 10)

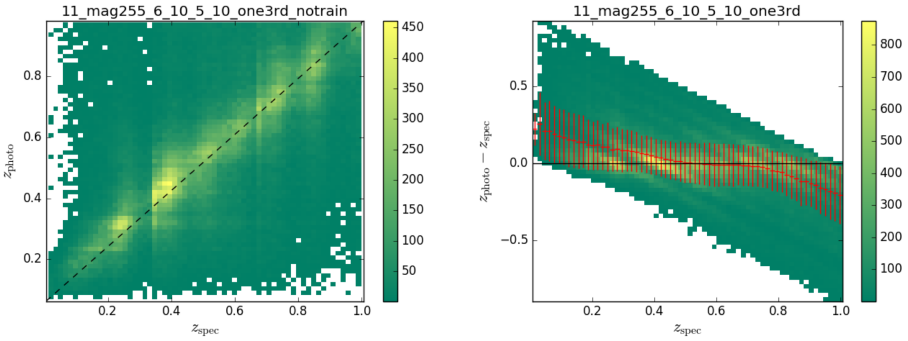


Figure 62: Comparison between photo-z and spec-z for 1-1 matching without lensing cuts. Right plot shows the subtraction of spec-z from photo-z. We are going to use (6, 10, 5, 10) for NRandom, NTrees, NAtt, and MinLeaf.

made two group of the brighter truth object to the brighter coadd object, and the fainter truth object to the fainter coadd object. After the lensing cuts and truth magnitude cut, only 38 objects remain in [brighter 2-2 brighter] and [fainter 2-2 fainter] group. The comparison for estimated photo-z and spec-z are shown in Figure 63

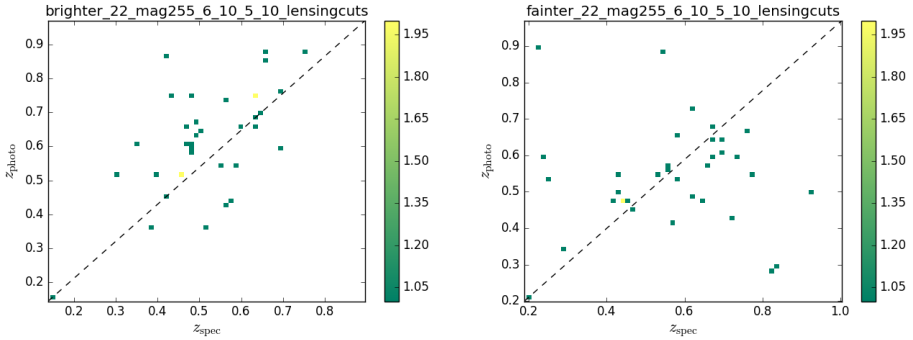


Figure 63: Photo-z estimation with MLZ for brighter and fainter object of 2 truth : 2 coadd object group. These are the results with lensing cut options.

### 5.4.5 Possible blended objects of 2 truth : 1 coadd and 3 truth : 1 coadd

The bigger difference between calibrated photo-z and spec-z near the 0 and 1 of spec-z could come from the bias of having more possible area above the diagonal line when spec-z is smaller than 0.5, and more below the diagonal line when spec-z is larger than 0.5. Hence we selected the data symmetrically between upper and lower the diagonal line as shown in Figure 64. Since we have two truth objects in [2-1] group, one has to be chosen when plotting pdf comparing spec-z of truth objects and photo-z estimated. We've made two lists of spec-z, one for brighter object and the other for fainter object between two truth objects. In Figure 69, we can clearly see that photo-z estimation of fainter object from 2 truth objects are more random and further from the diagonal line compared to the results using the brighter object. As we expected, most of [2-1] group will be a blended object with the fainter object merged into the brighter object nearby.

We also separated [2-1] groups into similar spec-z and different spec-z

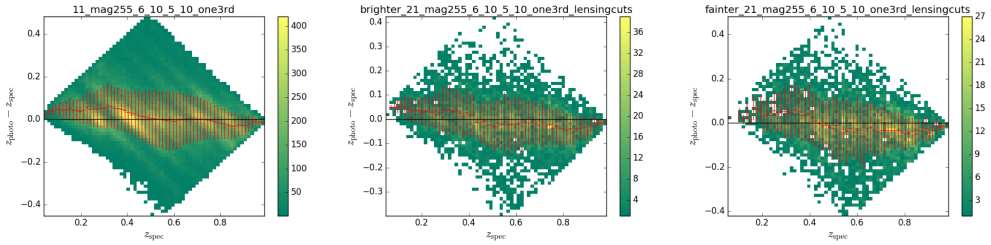


Figure 64: We selected the data symmetrically between upper and lower the diagonal line to remove bias. Left: 1-1, middle: brighter 2-1, right: fainter 2-1.

comparing spec-z of the brighter and fainter object. We defined "similar" if difference between brighter and fainter spec-z is less than 0.003. Obviously the "similar" group showed similar results both for the brighter and fainter objects. The "different" group showed visible change in the result of fainter object, more randomly spread while brighter object still estimated photo-z close to spec-z.

We can also see the photo-z estimation of the brighter object matches better with spec-z than the estimation from the fainter object in Figure 67.

With [3-1] group, we have categorized 3 truth objects into brightest, middle, and faintest object. Figure 68 shows that the photo-z estimation from the brightest object matches best with spec-z, and it gets worse and more random when we used fainter object.

### 5.4.6 Possible mis-detected objects of 1 truth : 2 coadd

With lensing cuts and magnitude 25.5 cut, only 20 objects remain in [1-2] group. Figure 69 shows the comparison of photo-z and spec-z. In this case, we have two coadd objects needed to be compared with one truth object's spec-z. We divided two coadd objects into brighter and fainter ones as we did for the possible blended object groups.

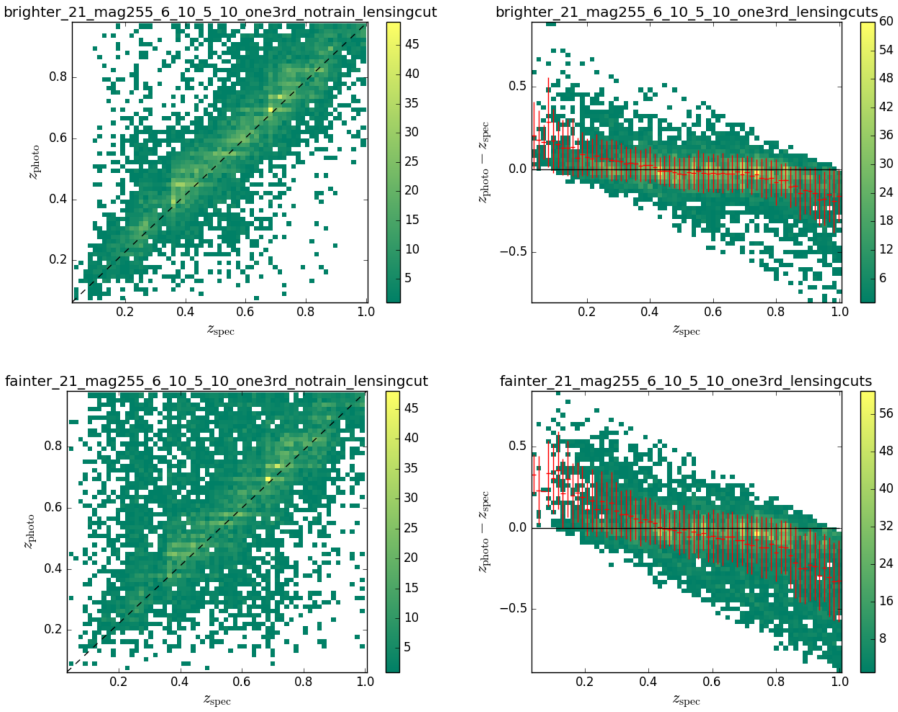


Figure 65: Photo-z estimation with MLZ for the 2 truth : 1 coadd object group. These are the results with lensing cut options and 3rd column shows the cut-off results to make upper and lower the diagonal line symmetric. Top: Spec-z of brighter object of truth catalog and Bottom: Spec-z of fainter object of truth catalog were used.

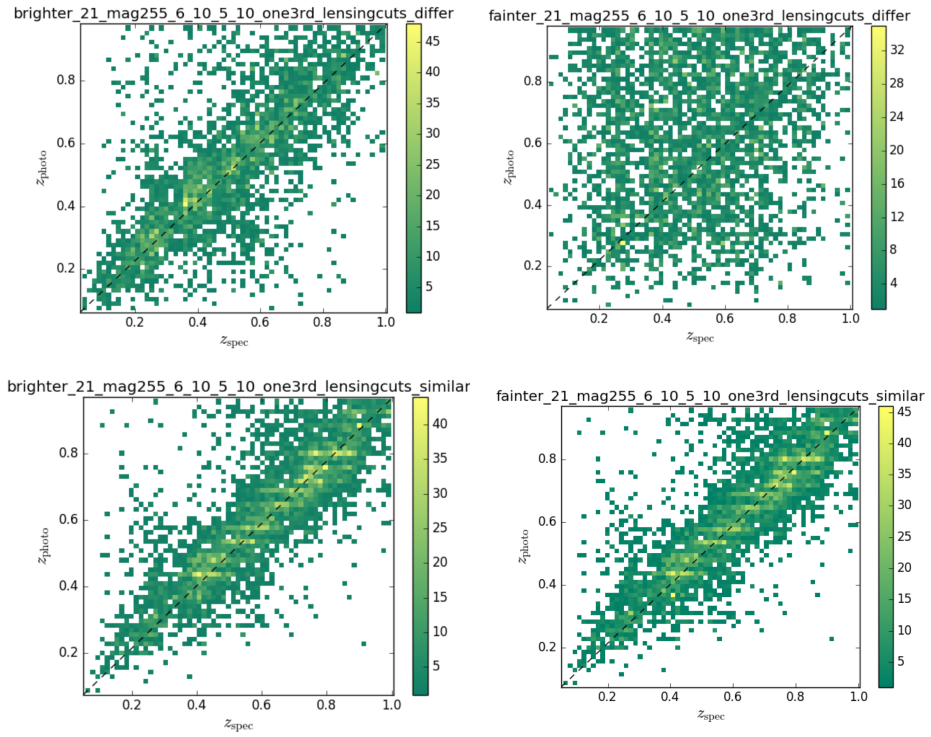


Figure 66: Photo-z estimation with MLZ for the brigher and fainter object in 2 truth : 1 coadd object group. These are the results with lensing cut options. Top: "different" spec-z group results. Bottom: "similar" spec-z group results.

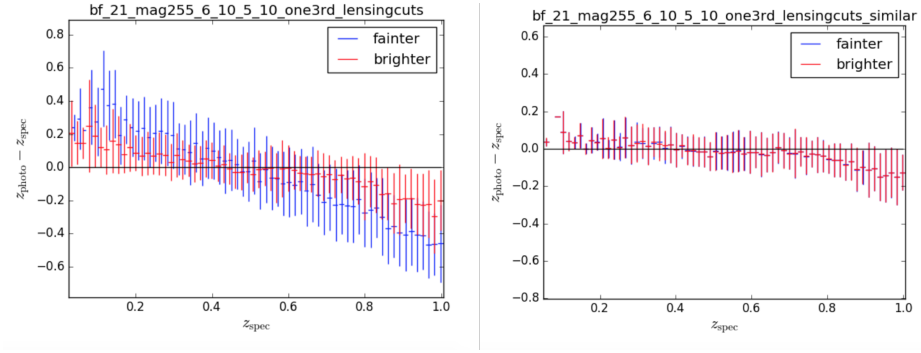


Figure 67: Photo-z estimation with MLZ for the 2 truth : 1 coadd object group. These are the results with lensing cut options. Comparison of brighter and fainter object results in one plot. Left: "different" spec-z group results. Right: "similar" spec-z group results.

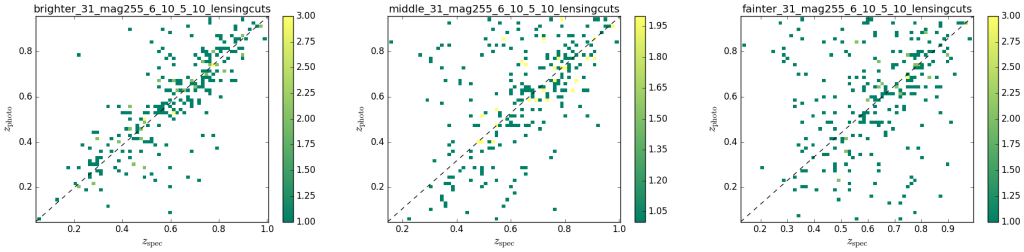


Figure 68: Photo-z estimation with MLZ for the 3 truth : 1 coadd object group. These are the results with lensing cut options. Left to right: brighter, middle, and fainter objects among 3 objects in truth catalog.

### 5.4.7 Statistics for all groups

After FoF matching, with the lensing cut and magnitude cut at 25.5 for truth objects, 339196, 43356, 5692, 98, and 174 coadd objects were matched in [1-1], [2-1], [3-1], [1-2] and [2-2] groups. Figure 70 shows the range of $\sigma$, $2\sigma$ and $3\sigma$ for each group, representing 68 %, 95 % and 99.7 % of coadd objecs lie in the range of photo-z.

The histogram in Figure 71 and Figure 72 shows the distribution of the photo-z estimated in each group. The mean and standard deviation of each

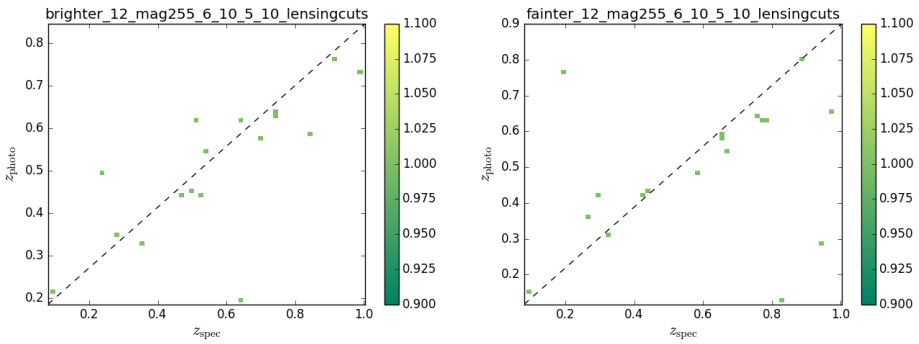


Figure 69: Photo-z estimation with MLZ for brighter (left) and fainter (right) object of 1 truth : 2 coadd object group. These are the results with lensing cut options.

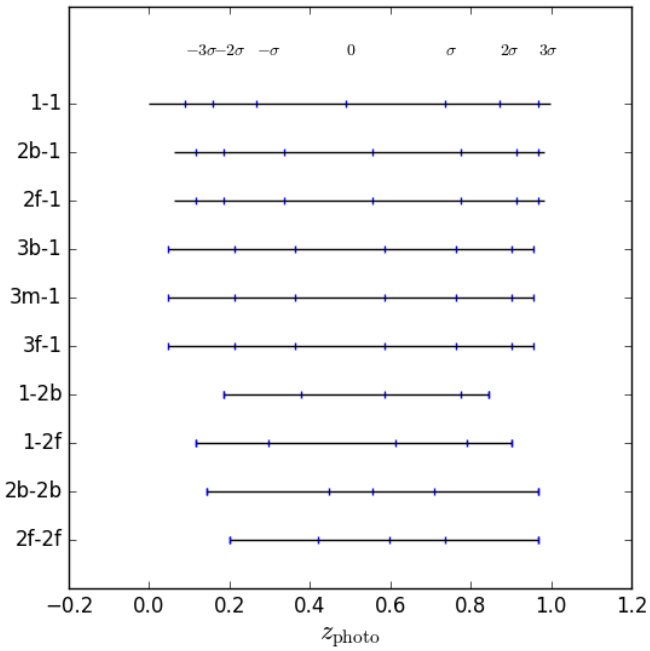


Figure 70: 1d histogram on a line showing -3$\sigma$ to +3$\sigma$ for each groups.

group are shown in Table 3.

| FoF group | option for multiple objects | mean | std |
|---|---|---|---|
| [1-1] | - | 0.50 | 0.20 |
| [2-1] | brighter | 0.56 | 0.20 |
| [2-1] | fainter | 0.58 | 0.19 |
| [3-1] | brighter | 0.58 | 0.19 |
| [3-1] | middle | 0.58 | 0.19 |
| [3-1] | fainter | 0.58 | 0.19 |
| [1-2] | brighter | 0.56 | 0.18 |
| [1-2] | fainter | 0.56 | 0.22 |
| [2-2] | brighter | 0.57 | 0.15 |
| [2-2] | fainter | 0.57 | 0.19 |

Table 3: The mean and standard deviation of the estimated photo-z for each group.

| FoF group | option for multiple objects | mean | std |
|---|---|---|---|
| [1-1] | - | 0.49 | 0.10 |
| [2-1] | brighter | 0.48 | 0.10 |
| [2-1] | fainter | 0.48 | 0.13 |
| [3-1] | brighter | 0.49 | 0.09 |
| [3-1] | middle | 0.47 | 0.12 |
| [3-1] | fainter | 0.51 | 0.13 |
| [1-2] | brighter | 0.30 | 0.00 (not enough samples) |
| [1-2] | fainter | 0.54 | 0.00 (not enough samples) |
| [2-2] | brighter | 0.52 | 0.11 |
| [2-2] | fainter | 0.53 | 0.17 |

Table 4: The mean and standard deviation of the estimated photo-z for each group in 0.45<spec-z<0.55 range.

The difference between brighter and fainter results are shown better in spec-z of 0.45 to 0.55 range. Table 4 and Figure 72 show the mean and standard deviation of the estimated photo-z of each group with spec-z of 0.45 and 0.55 range.

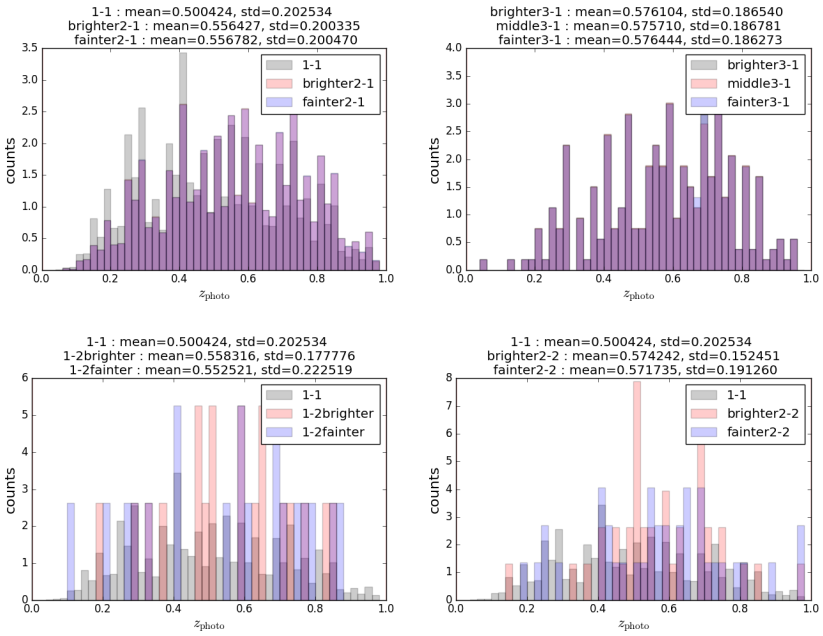


Figure 71: Distribution of the photo-z. Mean and standard deviation for each group are written above the histogram.

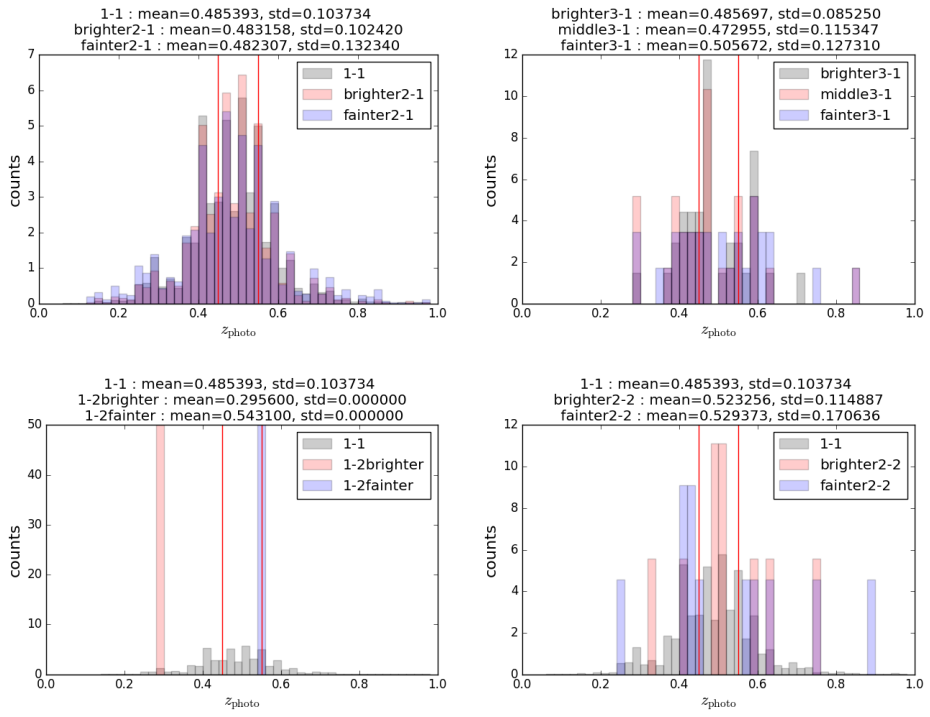


Figure 72: Distribution of the photo-z. Mean and standard deviation for each group are written above the histogram. These show the selected objects with spec-z range of 0.45 to 0.55.

### 5.4.8 Result from BPZ

Figure 73 shows the plot of PDF comparing spec-z and photo-z from BPZ of [1 truth : 1] coadd group.

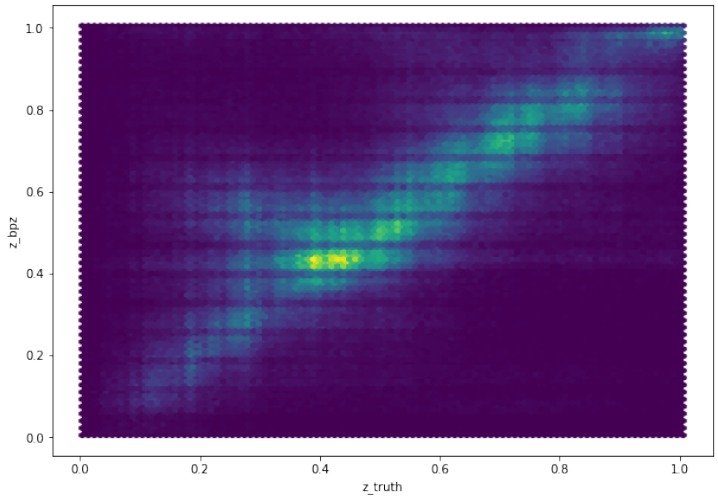


Figure 73: g
roup]Photo-z result from BPZ and spec-z comparison for [1-1] group.

Using the catalog of 'dc2_object_run1.2i_with_photoz', which has all the photo-z results from BPZ on each object of coadd catalog, all the PDF plots for each groups, [1-1], [2-1], [3-1], [1-2] and [2-2], were drawn as in Figure 74 and Figure 75. These plots look similar to MLZ results. Comparing brighter, middle (for [3-1]), and fainter truth object results, photo-z matched better with brighter object's spec-z.

To compare MLZ and BPZ results, difference between photo-z and spec-z were plotted together as in Figure 76 for [1-1] and [2-1] groups. The red line shows the result from BPZ and the black line shows the MLZ result.

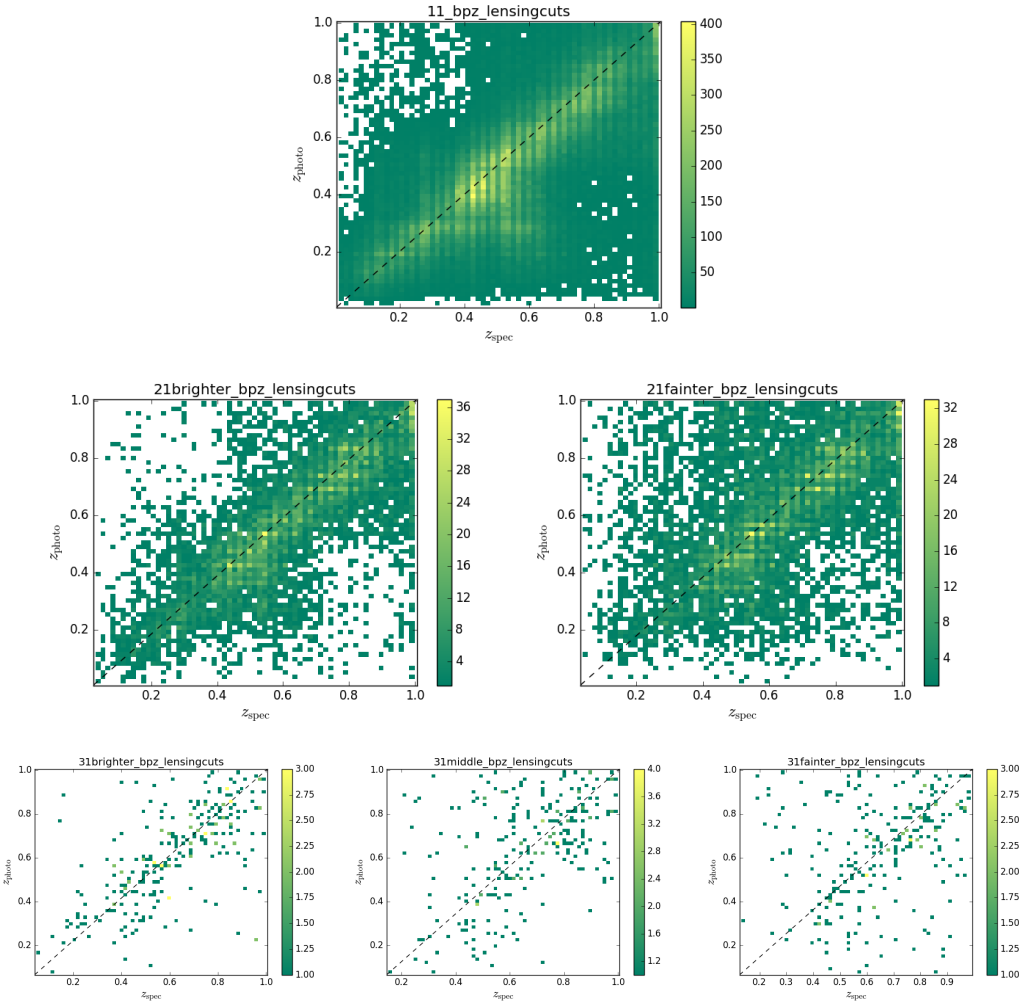


Figure 74: ,
[2-1], and [3-1] group] The plots of PDF from the BPZ results. From the top row, plots are showing [1-1], [2-1], and [3-1] group.

## 5.5 Conclusion

Using FoF matching, we have compared input and output catalogs of DC2, 1.2i, and grouped them by the number of input objects and the number of output objects. Assuming the larger number on the input objects than the

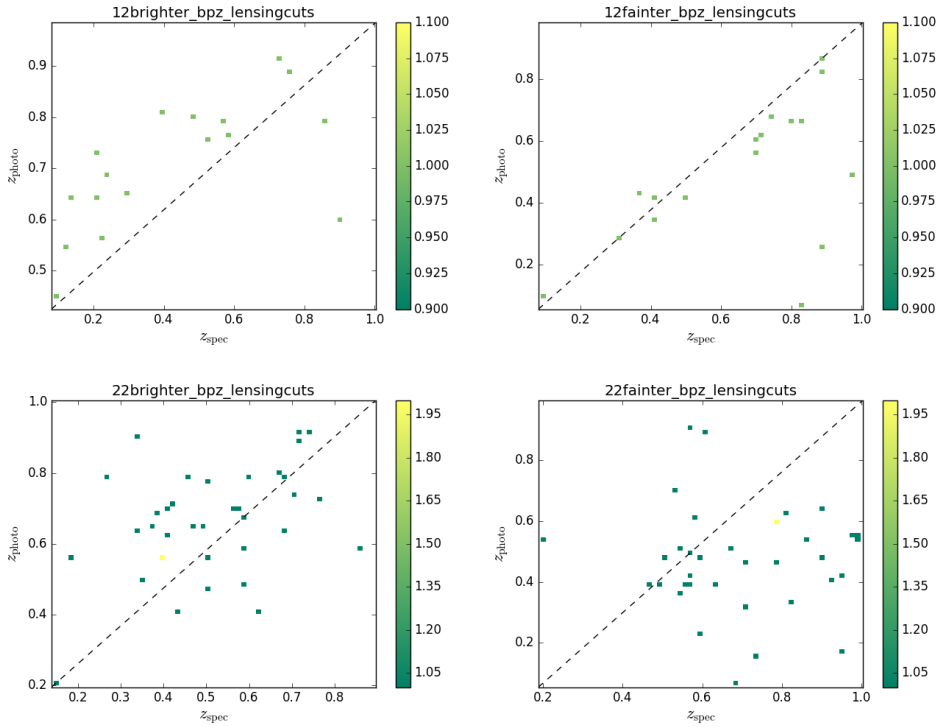


Figure 75: a
nd [2-2] group] The plots of PDF from the BPZ results. From the top row, plots are showing [1-2] and [2-2] group.

output objects is due to blending, we have studied [2-1] and [3-1] groups. Especially for [2-1] groups, we expected the fainter objects in truth catalog were merged into the brighter object(s), and the blended object(s) in the coadd catalog will be more affected by brighter object(s) in the truth catalog. Using MLZ and BPZ, photometric redshift estimation was done for each group, by giving color information of 6 filters. We have checked that the photometric redshift estimation on [2-1] groups showed more correlation with brighter object's spec-z than the spec-z of fainter object. Although [2-2] and [1-2] groups had very few objects matched, we could also see that the photo-z estimated follows spec-z better when brighter coadd object's color information was used.

We have also compared the photo-z results from the MLZ and the results

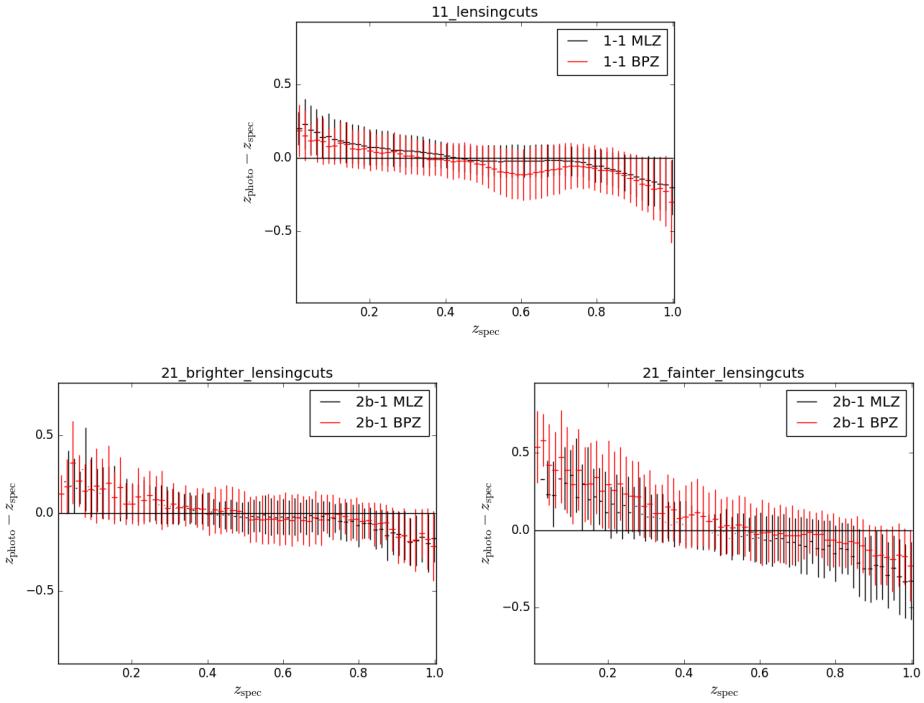


Figure 76: The subtraction of spec-z from photo-z from BPZ (red) and MLZ (black). Top : [1-1], Bottom : [2-1] brighter (left) fainter (right).

from the BPZ. Both methods showed similar results, showing the spec-z of brighter truth object matches better with the photo-z estimated.

The BPZ tool development and covariance matrix study is still in progress. We are going to apply this study to 2.1 catalogs and use this for deblending and to estimate photo-z more accurately.

# 6 Shear measurement for Large Scale Structures

## 6.1 Cosmic shear

As mentioned earlier, Cosmic shear is one of 3x2pt correlations that compares the shape of one galaxy to the shape of the other galaxy in pair. Since shape distortion due to gravitational lensing is very small and faint, it is important to reduce noise from all possible sources. For weak lensing study of DESC, it is suggested that size and shape of the galaxies should be measured with error by 0.1 % limit and 0.3 % limit. In this study, we are going to measure the size change in x, y, and 45 degrees directions and ellipticity $e1$ and $e2$ to calibrate shear $g1$ and $g2$ to check the cosmic shear correlation.

## 6.2 Method

### 6.2.1 GalSim and PhoSim

There are several simulation tools LSST-DESC is using: PhoSim, ImSim, and GalSim. Our Tree rings research results are applied to those and one can change the variables like amplitude, period, or the center of the Tree rings to run the simulation. While we are working on DC2 to use 2.1p (PhoSim)and 2.1i (ImSim) to apply Tree rings and CTE and plot cosmic shear correlation in TXPipe [33], we used simple GalSim and PhoSim simulation results to measure shape distortion from the Tree rings effect and CTE.

GalSim, ImSim and PhoSim are open-source software for simulating images of astronomical objects (stars, galaxies) in a variety of ways to calculate the physics of the atmosphere, telescope, and camera in order to simulate realistic optical/IR astronomical images [34] [36]. One can generate any set of objects to simulate with options to change variables for atmosphere and devices (telescope and camera). M. Jarvis, R. Mandelbaum, and J. Meyers are developing GalSim and ImSim, and J. Peterson is developing PhoSim. Test results of the LSST sensors and telescope information has been applied and will be updated more to the simulations.
We simulated single sensor image with grid of circular light sources with radius 1 pixel then measured change of the size in $x$, $y$, and $xy$ direction, and shape in + (vertical and perpendicular) and x (cross, 45 degrees) direction.

### 6.2.2 DESC Data-Management-Stack

Second moments $XX$, $YY$, and $XY$, and the ellipticities $e1$ and $e2$ were measured using LSST Science Pipelines software, DM (Data Management) stack. $e1$ and $e2$ are defined as Equation ((53)) when ellipticity $E$ is defined as Equation ((56)).

$$(e1, e2) = (Ecos(2\theta), Esin(2\theta)) \tag{53}$$

$$e1 = \frac{XX - YY}{XX + YY} \tag{54}$$

$$e2 = \frac{2XY}{XX + YY} \tag{55}$$

$$E = \frac{(a^2 - b^2)}{(a^2 + b^2)} \tag{56}$$

Initially, circular source objects will have ellipticity zero and 1 pixel of $a$, $b$, $XX$, $YY$, and $XY$ then will be distorted by atomosphere and device in the simulations. We will fix all other variables but values for the Tree rings effect or CTEs, then compare change depending on Tree ring's amplitude and period, and CTE values.
We could find all the object on the output image of the simulations by adjusting minimum fwhm of psf, background binsize, and minimum pixels for detection. After finding all hits, it measures the x and y position and second moments $XX$, $YY$, and $XY$. The script used to measure these variables is shown in Appendix B.1.

Using the second moments $XX$, $YY$, and $XY$, the ellipticities $e1$ and $e2$ are measured using the DM Stack pipeline in Appendix B.2.

### 6.2.3 TreeCorr

The cosmic shear correlation is calibrated by TreeCorr [62] [65]. TreeCorr is a package for computing 2-point and 3-point correlation functions using $(RA, DEC, r)$ or $(x, y, z)$ positions. Converting the $(x, y)$ position information to $(RAandDEC)$ in the unit of arcsec, TreeCorr will calculate $\xi$. The example of TreeCorr code given by M. Jarvis is shown in Appendix B.3. When the ellipticities $e1$ and $e2$ of the simulations with and without the sensor effects are put into $g1$ and $g2$ of the TreeCorr code, it will produce cosmic shear correlations of each case.

## 6.3 Results

### 6.3.1 Tree rings on GalSim

In GalSim we can choose to have simple *sin* function for Tree rings effect as shown in Figure 77-(a), without a dependency on radius.
Using the results of our study of Tree ring amplitude, depending on the distance from the center of wafer [5, 8], GalSim developed the code to apply Tree ring amplitude to follow the quadratic function, so that amplitude increases as radius gets larger, and makes users choose the coefficients. Instead of using Equation (57), GalSim defines centroid shift to follow Equation (58) and gives $A$, $B$, $CosFreq$, $CosPhase$, $SinFreq$, and $SinPhase$ variables, following real Tree ring data of LSST production sensors we measured above [5, 8]. To check clear Tree ring pattern, we have compared two flat images with coefficient B of Equation ((58)) as $4 \times 10^{-18}$ and $4 \times 10^{-5}$, and the resulting images are shown in Figure 77-(b,c). As an additional option, we can change center and period of Tree rings as well. We used the center of Tree ring (-295.1, -391.4) to have Tree rings in direction from left bottom corner to top right corner. For other coefficients, $CosFreq$, $CosPhase$, $SinFreq$ and $SinPhase$, we have used given variables in the parameter setting input file for R10 S00 sensor and all the values we have used are shown in Table 5.

$$Amplitude(r > 4000pix) = ar^2 + br + c \tag{57}$$

$$\begin{aligned} shift = \Big(\big(A + Br^2\big) * 0.01\Big) * \Bigg( & \sin\Big(2\pi * \big(\frac{r}{fval} + cphases\big) * \frac{fval}{2\pi}\Big) \\ & - \cos\Big(2\pi * \big(\frac{r}{fval} + sphases\big) * \frac{fval}{2\pi}\Big)\Bigg) \end{aligned} \tag{58}$$

After checking the Tree ring pattern with flat images, to see shape distortion due to Tree rings effect, we have generated circular objects with a radius of 1 pixel, spread in grid with 40 pixels of distance between the adjacent objects. In Figure 78, by subtracting image without Tree rings from the image with simple Tree rings, we can check that objects are shifted in radial direction to make brighter and darker areas.

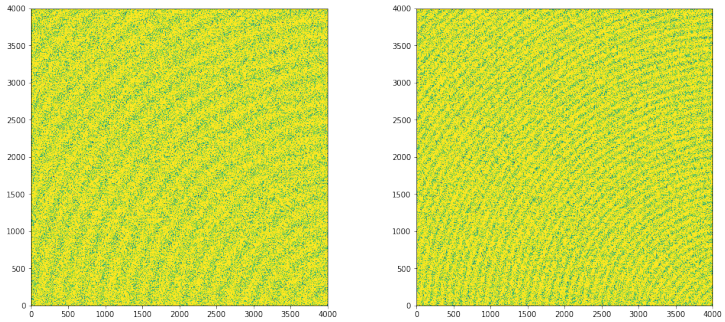

Figure 77: Flat images of Tree rings of LSST production sensors with different period options.

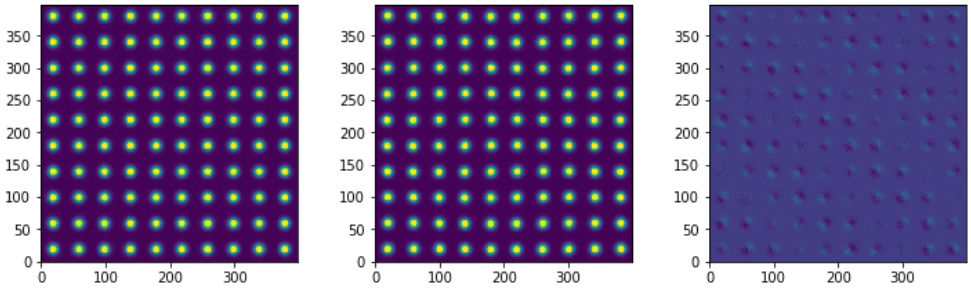

Figure 78: Source objects in grid: (a) without and (b) with Tree rings, and (c) subtract a from b.

### 6.3.2 Second moment $XX$, $YY$, and $XY$ with Tree rings on GalSim

$XX$ and $YY$ without the Tree rings effect were higher than 1 due to other effects. Adding Tree rings effect, $XX$ and $YY$ increase from 1.1 to 1.25 and XY decreased from $3.1 \times 10^{-5}$ to $-3.3 \times 10^{-5}$ when the coefficient of quadratic function of Tree ring amplitude was $4 \times 10^{-5}$. We can see dramatic change in Figure 79 with extreme Tree ring case, and we could also check that size distribution gets broader with Tree rings.

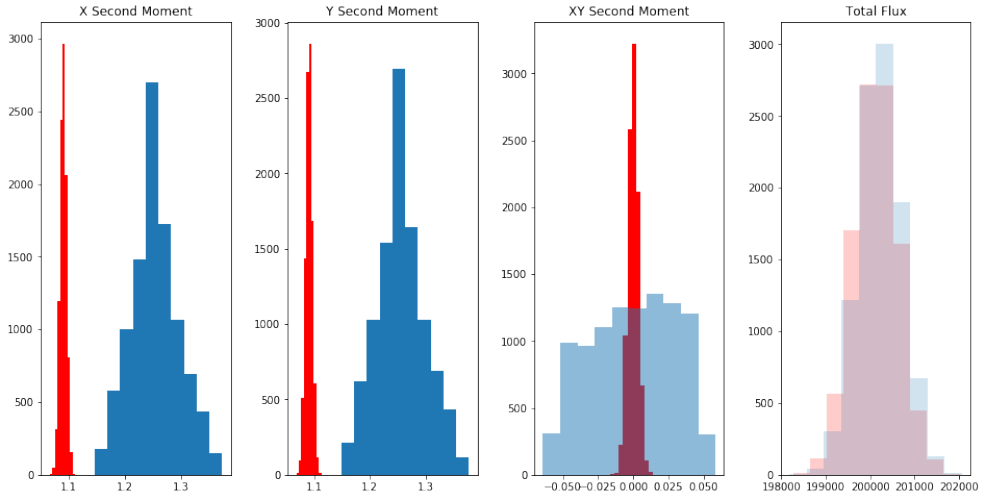


Figure 79: $XX$, $YY$, and $XY$ with and without Tree rings effect. Blue shows and red shows Tree rings on with the coefficient of quadratic function of Tree ring when coeffient $B$ was set to $4 \times 10^{-5}$.

### 6.3.3 Ellipticity $e1$ and $e2$ with Tree rings on GalSim

Without Tree rings, $e1$ and $e2$ histogram were spread near 0, as in Figure 80-(a), meaning shape of the objects are circular without Tree rings. When Tree ring is applied, both $e1$ and $e2$ of sources increased from near 0 to near 0.4 as in Figure 80-(b). $e1$ and $e2$ relation also lost its symmetric, showing less of e1 distribution near 0.0.

| object type | Tree ring coefficients in Eq 58 | | | | | | result |
|---|---|---|---|---|---|---|---|
| | A | B | CosFreq | CosPhase | SinFreq | SinPhase | |
| radius 1 pixel | 0.002 | $4 \times 10^{-10}$ | 62.0 | 5.8 | 62.9 | 2.6 | small Tree ring |
| | | | 63.3 | 2.8 | 48.5 | 3.0 | |
| | | | 62.9 | 2.5 | 53.8 | 2.1 | |
| | | | 36.4 | 5.1 | 66.7 | 2.3 | |
| | | | 62.3 | 1.3 | 59.1 | 0.2 | |
| | | | 55.0 | 1.0 | 59.5 | 1.8 | |
| | | | 53.2 | 6.0 | 58.1 | 3.9 | |
| | | | 69.5 | 3.2 | 72.2 | 1.5 | |
| | | | 79.6 | 0.7 | 60.1 | 5.2 | |
| | | | 59.1 | 1.8 | 60.5 | 0.6 | |
| | | | 55.9 | 6.0 | 58.3 | 5.1 | |
| | | | 49.8 | 1.9 | 68.0 | 4.6 | |
| | | | 53.2 | 5.9 | 60.6 | 2.7 | |
| | | | 53.6 | 1.6 | 36.9 | 5.1 | |
| | | | 41.7 | 4.0 | 67.0 | 4.8 | |
| | | | 30.6 | 3.1 | 43.9 | 4.6 | |
| | | | 31.4 | 1.8 | 48.4 | 1.1 | |
| | | | 31.3 | 1.1 | 29.3 | 1.4 | |
| | | | 18.3 | 1.1 | 21.1 | 1.5 | |
| | | | 26.4 | 2.1 | 44.0 | 2.6 | |
| radius 1 pixel | 0.002 | $4 \times 10^{-5}$ | same as above | | | | extreme Tree ring |

Table 5: GalSim options used to compare simulated images with Tree rings effect.

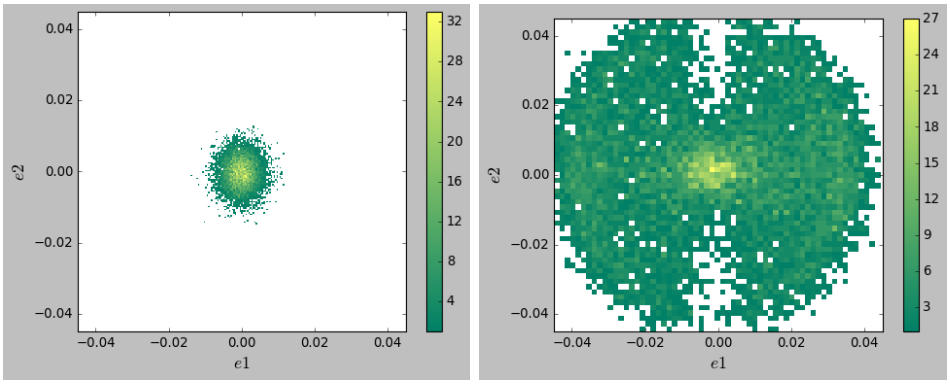


(a) (b)

Figure 80: Histogram of $e1$ and $e2$ for (a) Tree rings off (b) Tree rings on with the coefficient of quadratic function of Tree ring when coefficient $B$ was set to $4 \times 10^{-5}$.

### 6.3.4 Tree rings on PhoSim

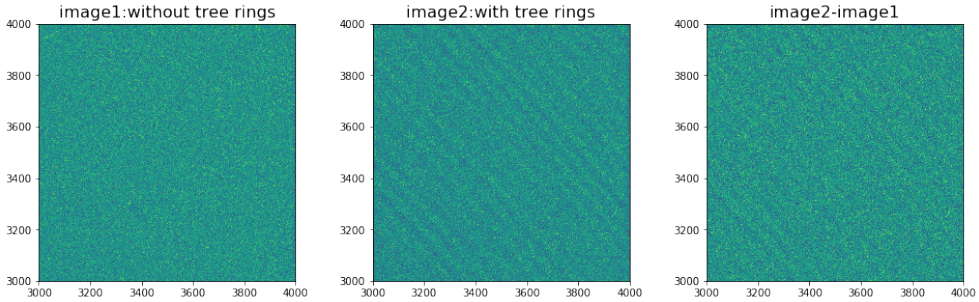


(a) (b) (c)

Figure 81: Flat images (a) with LSST Tree rings on with Tree ring's amplitude=0.7 % and (b) without Tree rings (amplitude=0). (c) Subtract b from a, in x and y range 3000 to 4000 pixels.

Figure 81 shows the simulated flat images with Tree rings' amplitude set to 0 (without Tree rings) and 0.7. PhoSim allows users to choose amplitude and period of the Tree rings, in the LSST sensor option setting file as an instrumentation option. Flat images in PhoSim are dome flat images, hence

fluxes over the sensor are not uniform and we can see that the top right corner receives more light than the bottom left corner.

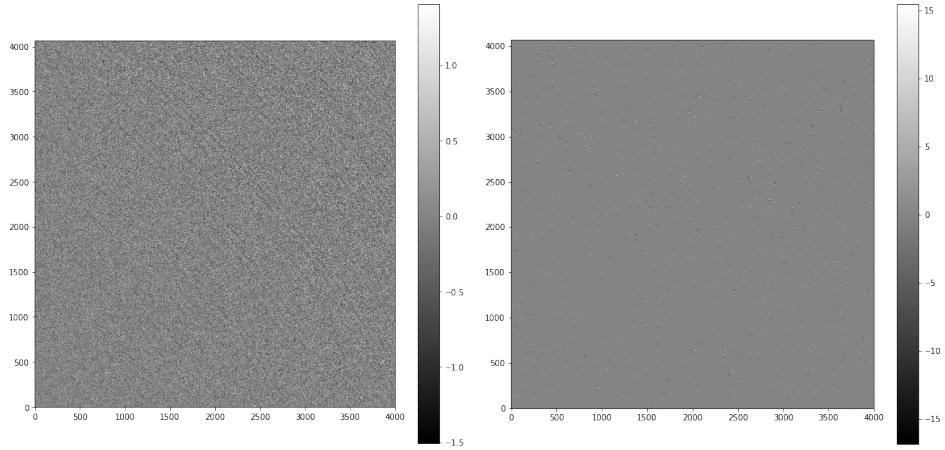


(a) (b)

Figure 82: Bigger image for subtracting "Tree ring off" from "Tree ring on". (a) Flat image (b) randomly spread objects

Instead of the objects in grid which we have used with GalSim, randomly spread objects were used with PhoSim. A hundred Gaussian objects with radius of 0.1 arcsec with magnitude of 18, were spread randomly over the R22-S11 sensor. We also made another set with 100 point objects, with magnitude of 18 spread randomly over the same sensor. We checked that objects are shifted to make bright and dark areas as shown in Figure 83 and Figure 84. However, its relevance with a radial Tree ring pattern was not visible in the image because very small objects were randomly spread and the distances between the objects were not close enough to see the pattern. Subtraction of two images with and without Tree rings effect are shown in Figure 83 for the Gaussian objects, and in Figure 84. Different scales for zooming the image were used for Figure 83 and Figure 84 to emphasize electron shift better. For later study on shape distortion, we chose to use the results of point objects, since it is harder to detect larger Gaussian objects, and also harder to define shape of Gaussian objects compared to point sources.

When we set Tree ring amplitude to be zero, a bug was revealed, resulting in 0.0 flux across the entire area. If we turn off field anisotropy and impurity

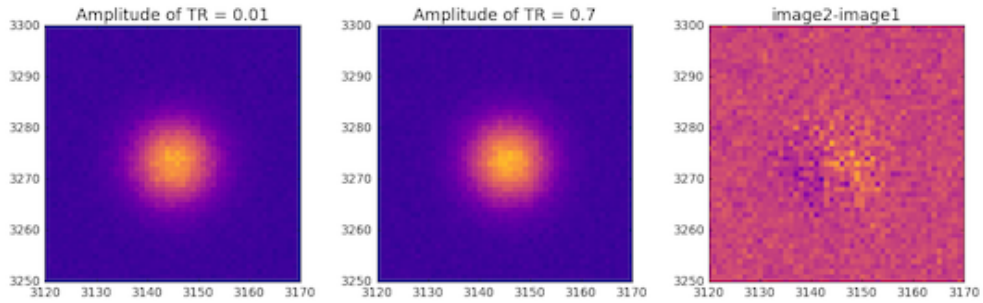


(a) (b) (c)

Figure 83: Randomly spread Gaussian objects (a) with Tree rings with amplitude 0.01 (b) with Tree rings with amplitude 0.7. (c) Subtract image a from b.

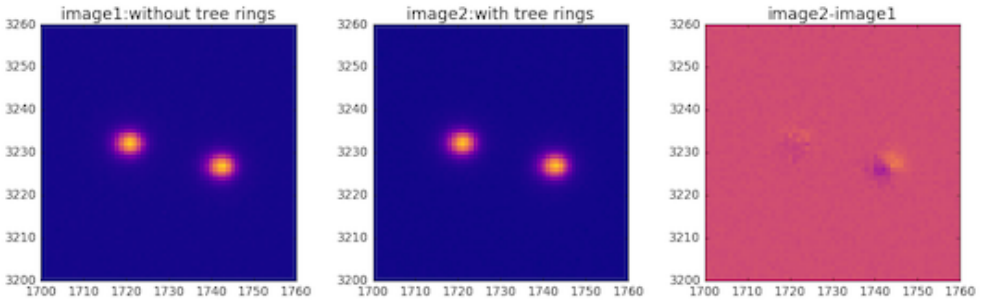


(a)

Figure 84: Randomly spread point objects (a) without Tree rings (b) with Tree rings with amplitude 0.7. (c) Subtract image a from b.

variation, it can turn off other sensor effects as well. Hence we set a very small Tree ring amplitude, with a value of $10^{-7}$, to simulate a sensor without Tree ring effect. Options used for PHOSIM are shown in Table 6. One can change Tree ring amplitude with sensor file, under instrumentation option files of PHOSIM and turn on/off atmosphere or sensor effects from observation parameters of PHOSIM.

| object type | Tree ring amplitude | fieldanisotropy impurityvariation | result |
|---|---|---|---|
| Gaussian sigma 1.0 | 0.01 | 1 | object too big |
| Gaussian sigma 1.0 | 0.7 | 1 | object too big |
| point | 0.03 | 0 | removing other effects also |
| point | 0.0 | 1 | resulting error to make all flux zero |
| point | $10^{-7}$ | 1 | Tree ring effect very small, considered as no Tree rings |
| point | 0.7 | 1 | large Tree rings effect |
| point | 0.03 | 1 | average LSST Tree ring amplitude at bbv 50V |

Table 6: PHOSIM options used to compare simulated images with Tree rings effect. For fieldanisotropy and impurityvariation, 1 is on and 0 is off. We also used nobackground option for all the simulations.

### 6.3.5 Second moment $XX$, $YY$, and $XY$ with Tree rings on PhoSim

LSST pixel size is 0.2 arcsec and 10 $\mu$m, which means that if Gaussian object has sigma of 1 arcsec, it is equal to 50 $\mu$m and 5 pixels. When we simulated Gaussian objects with sigma of 1 arcsec, $XX$ and $YY$ without Tree rings effect were slightly different, 4.17 and 5.55. Adding Tree rings effect the second moment $XX$ increased from 4.17 to 4.21 and $YY$ increased from 5.55 to 5.59. We could also see that histogram of XY became broader in Figure 85. Medain XY decreased from -0.011 to -0.017 when Tree rings amplitude was 0.7.

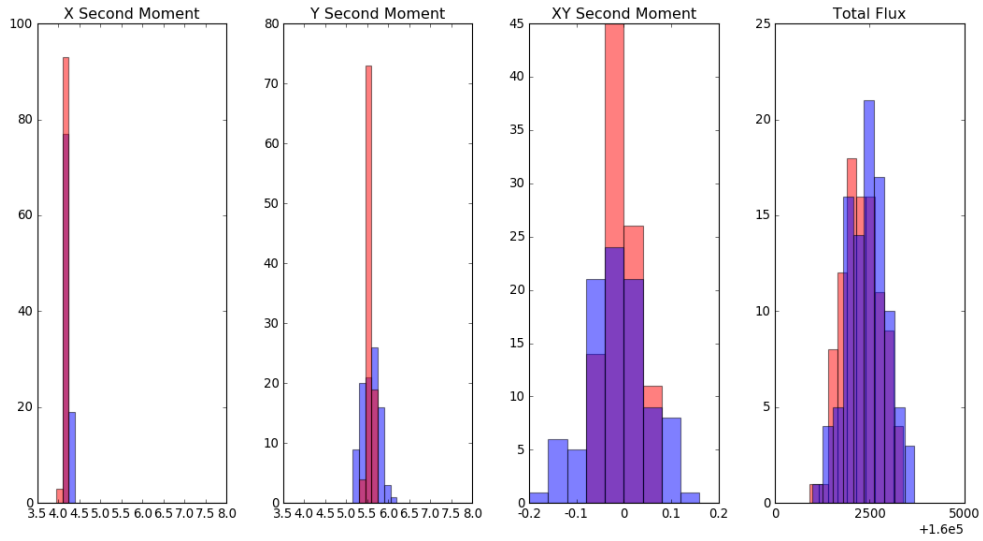


Figure 85: Gaussian object sources. $XX$, $YY$, $XY$, and flux histogram with and without Tree rings effect. Red shows Tree rings off and blue shows Tree rings on with amplitude 0.7

Point objects also had larger $YY$ than $XX$ with and without Tree rings effect. When Tree ring with amplitude 0.7 was applied, median $XX$ decreased from 3.880 to 3.872 and median $YY$ increased from 5.267 to 5.286. Median XY changed from -0.0081 to -0.0173. (Top histograms on Figure 86) When Tree ring amplitude was 0.03, as the mean Tree ring amplitude from the 189 LSST production sensors, change in $XX$, $YY$, and $XY$ were very small as expected. $XX$ and $YY$ increased to 3.907 and to 5.303. The distribution of XY got broader and median value changed to -0.0283. (Bottom

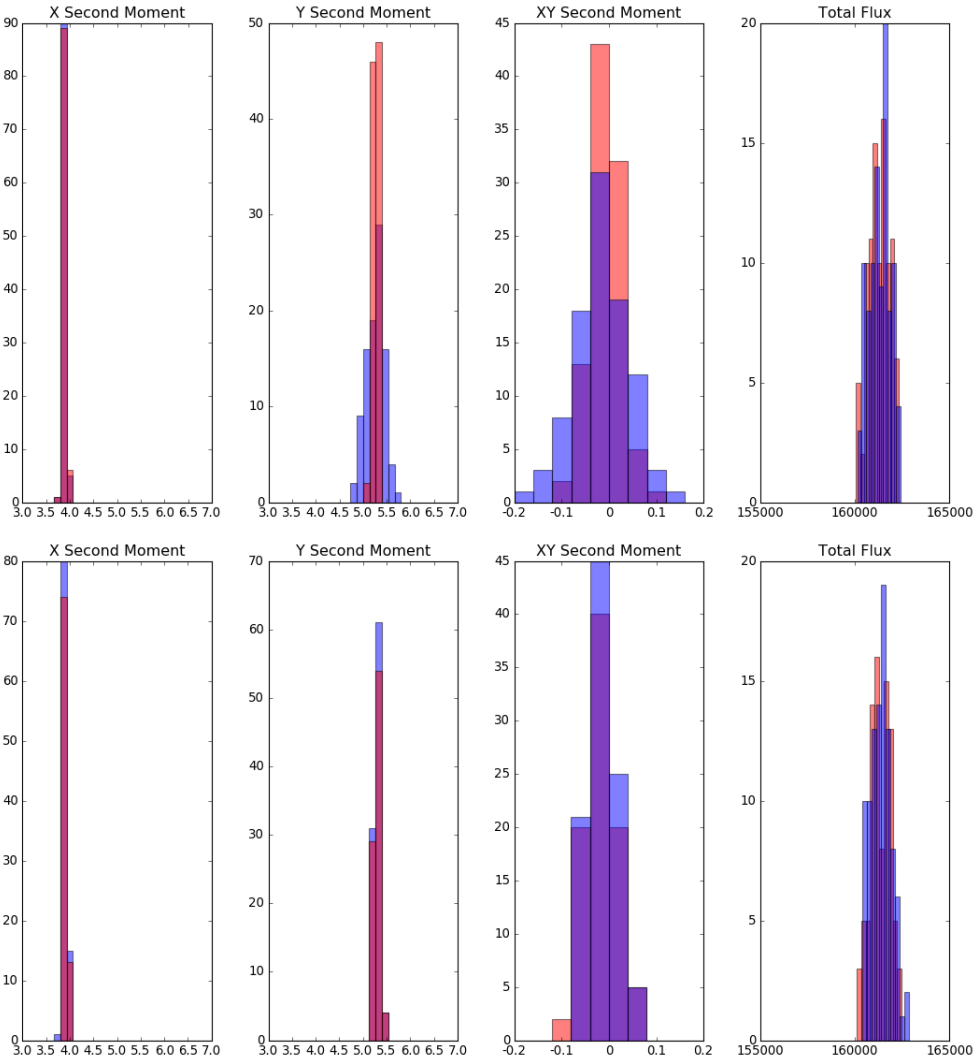


Figure 86: Point object sources. $XX$, $YY$, $XY$, and flux histogram with and without Tree rings effect. Red shows Tree rings off and blue shows Tree rings on with amplitude 0.7 (top) and with amplitude 0.03 (bottom).

histogram of Figure 86)

### 6.3.6 Ellipticity $e1$ and $e2$ with Tree rings on PhoSim

Change in shape of the point objects was not enough to visibly notice, as shown in bottom row of Figure 84. However, in bottom row of Figure 84-(c) by subtracting the image without Tree ring from the image with Tree ring amplitude 0.7, we could check that the object was shifted, radially, making a brighter pattern to the top right and darker pattern on the bottom left side of the object.

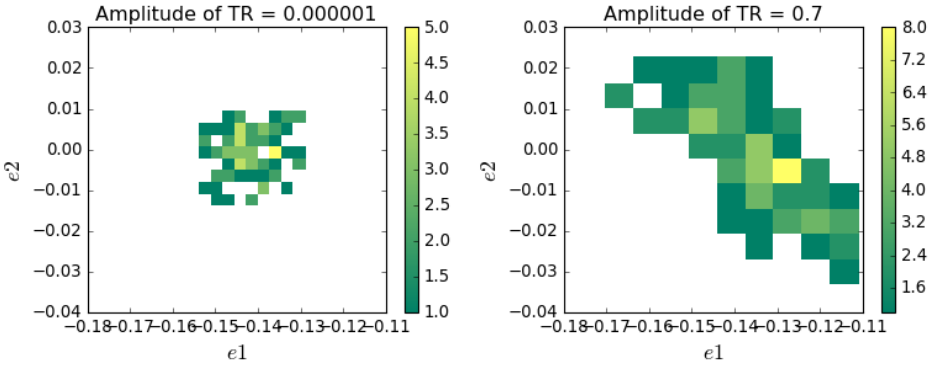


(a) (b)

Figure 87: Histogram of $e1$ and $e2$ for Gaussian objects with (a) Tree rings off (b) Tree rings on with amplitude 0.7.

Figure 87 shows the $e1$ and $e2$ comparison for Gaussian objects simulated with Tree rings off and Tree rings on with amplitude 0.7. Gaussian objects simulation without Tree rings, $e1$, $e2$ and total ellipticity $e$ were -0.142, -0.0014, and 0.142. With Tree rings amplitude 0.7, $e1$ and $e2$ decreased to -0.02 and -0.01. Total ellipticity decreased to 0.071.

Ellipticities $e1$ and $e2$ were both near 0 without Tree rings effect. Without the Tree rings (with very small amplitude of Tree rings $10^{-7}$), $e1$ and $e2$ were -0.151 and -0.0017. Total ellipticity was 0.151. With Tree ring amplitude 0.03, which is the amplitude from the 189 LSST production sensors, mean $e1$ and $e2$ were -0.152 and -0.0052. The mean ellipticity was 0.152. With the Tree ring amplitude 0.7, total ellipticity decreased to 0.152. Mean $e1$ and $e2$ were -0.151 and -0.0037. We could check that the Tree ring effect with

amplitude 0.03 will not bring significant change in ellipticity $e1$ and $e2$. As shown in Figure 88, as amplitude of the Tree rings gets larger, $e1$ and $e2$ distribution spreads broader, and towards -0.11 and -0.04 for $e1$ and $e2$.

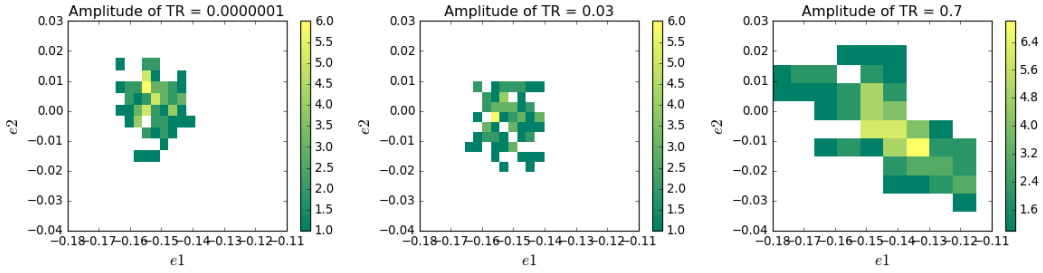


(a) (b) (c)

Figure 88: Histogram of $e1$ and $e2$ for point sources with (a) Tree rings off (b) Tree rings on with amplitude 0.03 (c) Tree rings on with amplitude 0.7.

### 6.3.7 Tree rings on cosmic shear correlation

Comparing 2pt correlation with and without Tree rings, we could check that the Tree rings effect of LSST production sensors will not be significant to Weak Lensing study. With an extreme case of GalSim the change in the correlation was very visible, and the ratio $< \frac{\xi_{noTR}}{\xi_{withTR}} >$ was 0.78. With PhoSim, the difference between extreme case and standard was unnoticeable compared to GalSim result as shown in Figure 89 and Figure 90.

The cosmic shear correlation for point sources are shown in Figure 90. The left plot shows the cosmic shear correlation of the Tree ring amplitude $10^{-7}$ case (blue) and the amplitude 0.03 case (red) and the right plot shows the cosmic shear correlation of the Tree ring amplitude $10^{-7}$ case (blue) and the amplitude 0.7 case (red). We can see that the Tree ring from 189 LSST production sensors will not affect cosmic shear correlation much, but larger Tree ring amplitude could cause uncertainty.

The cosmic shear correlation study is in progress and the simulation will be extended to cover larger area and to contain real galaxies model. Since Tree ring amplitude 0.7 in PhoSim brought negligible change in the cosmic shear correlation, larger Tree ring amplitude will be tested as well.

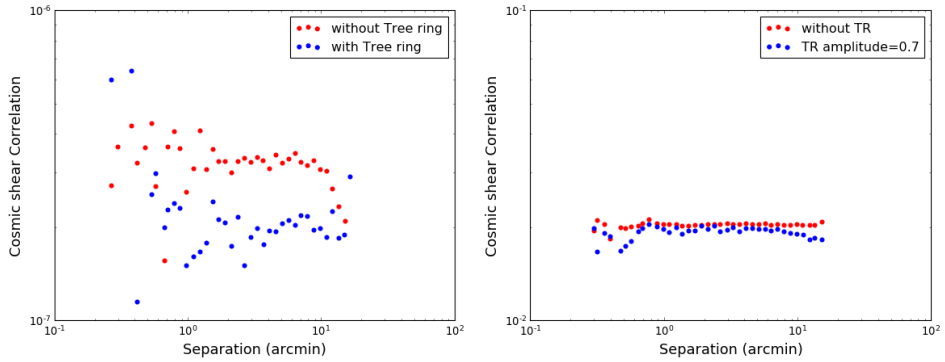


(a) (b)

Figure 89: The cosmic shear correlation comparison between (a) with and without the Tree ring on GalSim and (b) the Tree ring amplitude $10^{-7}$ and 0.7 for PhoSim simulation with Gaussian objects.

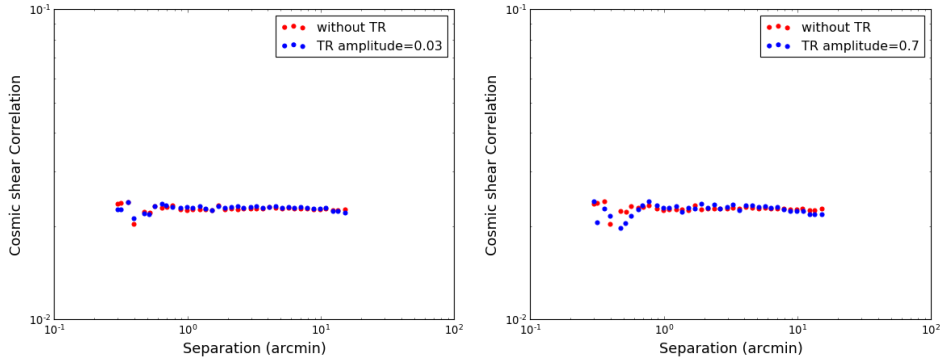


(a) (b)

Figure 90: The cosmic shear correlation comparison between (a) the Tree ring amplitude $10^{-7}$ and 0.03 (b) the Tree ring amplitude $10^{-7}$ and 0.7, both for PhoSim simulation with point objects.

### 6.3.8 CTE on PhoSim

Using PhoSim, we've changed HCTE from 1 to 1-5e-6 which is LSST specification and 0.5 to see extreme changes, while fixing VCTE to 1. We could expect that circular object with a tail of leaked electrons will increase the ellipticity. Figure 91 shows how CTE changes the shape of the circular source object. We also simulated 100 randomly spread point objects with magni-

tude 18, over R22 S11 sensor. We can see that shape of the point object gets wider and longer as we decrease serial and vertical CTE values. Because the second moment $XX$ is larger than $YY$ even with the perfect case, the increase in $XX$ makes the shape more elliptical but the increase in $YY$ makes the shape more circular. Left image shows when both CTEs are 1.0, middle image shows the CTE meets the LSST specification, 0.999995 (HCTE) and 0.999997 (VCTE), and right image shows when either CTE is extremely small, 0.5.

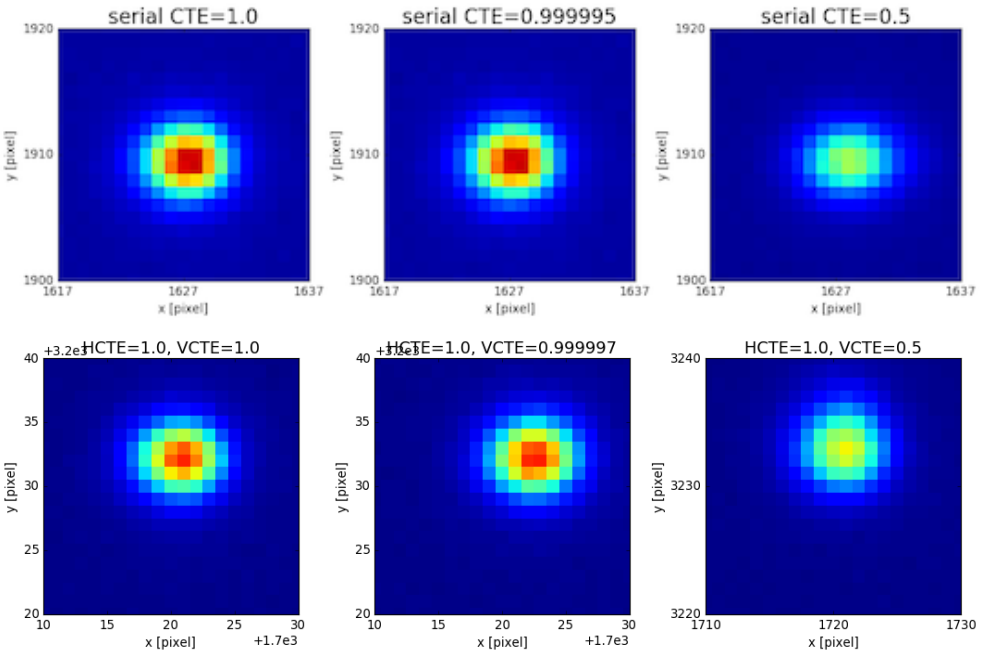


Figure 91: The shape of the source changing due to decrease in the serial CTE (top) and the vertical CTE (bottom). Left to right shows the perfect case, specification case, and the extreme bad case of CTE.

### 6.3.9 second moment $XX$, $YY$, and $XY$ with CTE on PhoSim

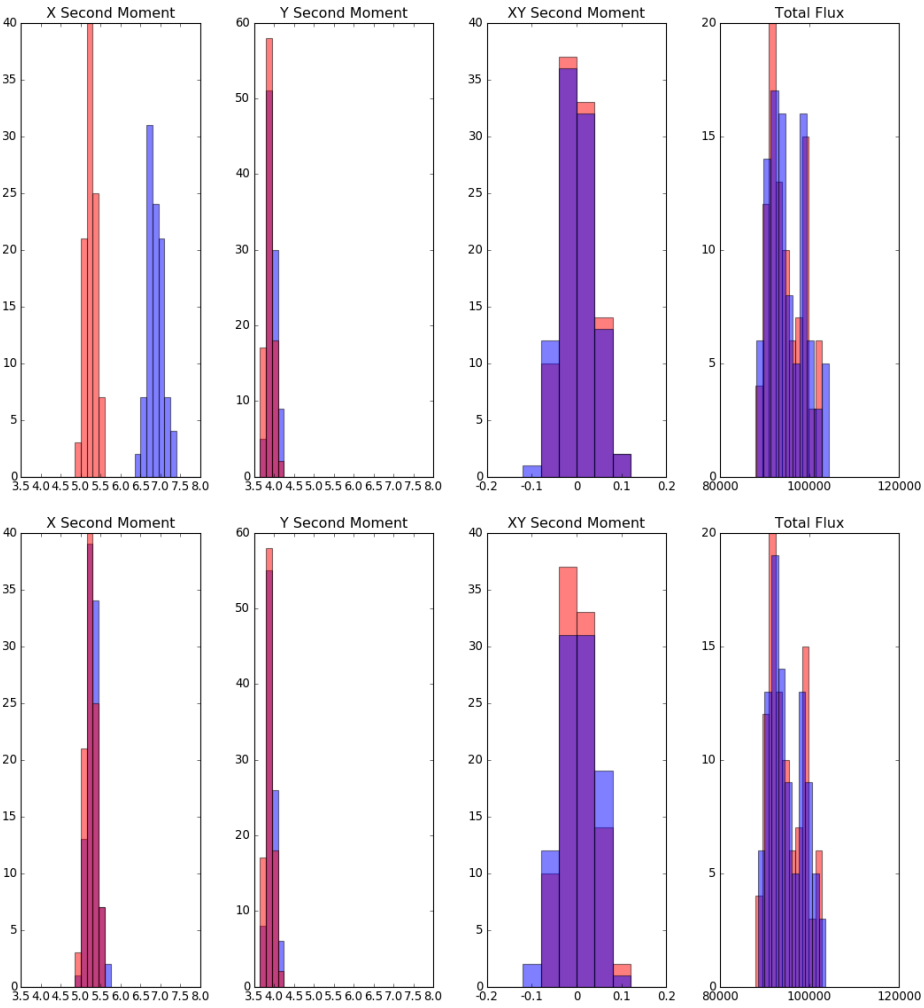


Figure 92: $XX$, $YY$, and $XY$ with HCTE. Top : Blue shows HCTE = 0.5, and red shows HCTE = 1.0. Bottom : Blue shows HCTE = 0.999995 as LSST specification, and red shows HCTE = 1.0. All with VCTE = 1.0

Here also, $XX$ was larger than $YY$ due to other effects even with both CTE 1. We can clearly see that $XX$ increases when serial CTE was extreme, 0.5, in top row of Figure 92. When VCTE is 0.5, $YY$ increased significantly as shown in Figure 93.

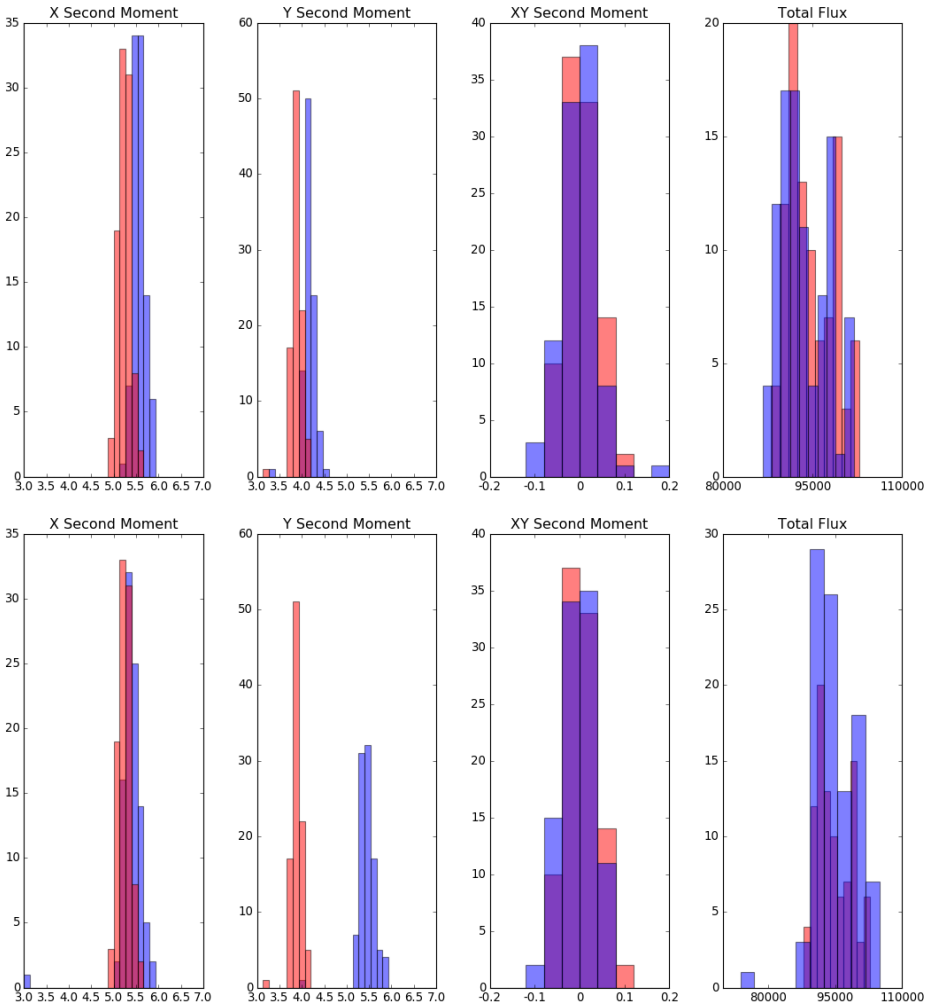


Figure 93: $XX$, $YY$, and $XY$ with VCTE. Top : Blue shows VCTE = 0.5, and red shows VCTE = 1.0. Bottom : Blue shows VCTE = 0.999997 as LSST specification, and red shows VCTE = 1.0. All with HCTE = 1.0

With serial CTE 0.5, $XX$ and $YY$ increased from 5.23 to 6.84 and 3.88 to 3.93. With HCTE $1 - 5 \times 10^{-6}$ as the specification of LSST, increase in $XX$ and $YY$ were insignificant. $XX$ and $YY$ increased from 5.23 to 5.28 and 3.88 to 3.90. The median XY increased fro 0.00039 to 0.0030.

With parallel CTE 0.5, $XX$ and $YY$ increased from 5.23 to 5.6, and 3.88 to 5.43. Due to electrons left behind, second moment $YY$ had a robust increase. With VCTE $1 - 3 \times 10^{-6}$ as the LSST specification, $XX$ and $YY$ increased from 5.23 to 5.6, and 3.88 to 4.1.

### 6.3.10 Ellipticity $e1$ and $e2$ with CTE on PhoSim

As serial CTE and vertical CTE gets smaller, we saw that circular shape of the object gets broader in x and y direction in Figure 91. Therefore we can expect ellipticity in x direction gets larger which means e1 will be larger, when serial CTE decreases. We could check that from Figure 94. Mean e1 increased from 0.15 to 0.15 and 0.2719, mean e2 decreased from 0.00080 to 0.00060 and -0.00003, and mean e increased from 0.1501 to 0.1502 and 0.2720 as serial CTE changed from 1 to 0.999995 and 0.5.

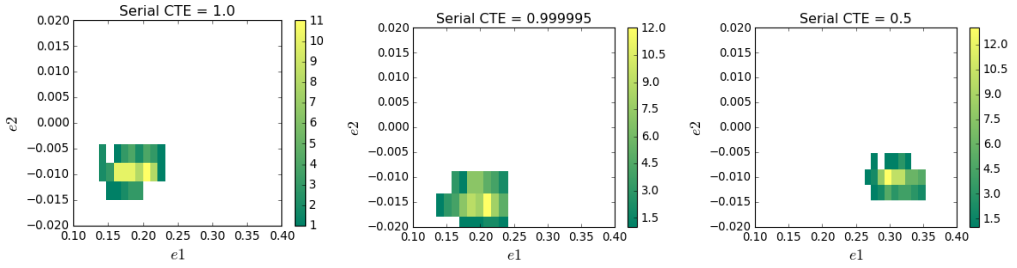


(a) (b) (c)

Figure 94: Histogram of $e1$ and $e2$ for (a) HCTE = 1 (b) HCTE=1-5e-6 and (c) HCTE=0.5.

As shown in Figure 95, $e1$ and $e2$ had robust change with VCTE = 0.5. When both CTEs are 1, $e1$ and $e2$ are 0.145 and 0.0008. Total ellipticity is 0.150. When VCTE is $1 - 3 \times 10^{-6}$, $e1$, $e2$ and total ellipticity are 0.146, -0.0005, and 0.146. For VCTE 0.5, $e1$ and $e2$ decreased to -0.006 and -0.001. Total ellipticity for VCTE 0.5 was 0.0132. In the beginning we expected the ellipticity will increase if VCTE gets smaller. However since the $XX$

was larger than $YY$ due to other effects than CTE, it is more elliptical with perfect CTE, then when CTE gets smaller and spills electrons, $YY$ grows and the shape becomes more circular. We can check it in Figure 91 as well.

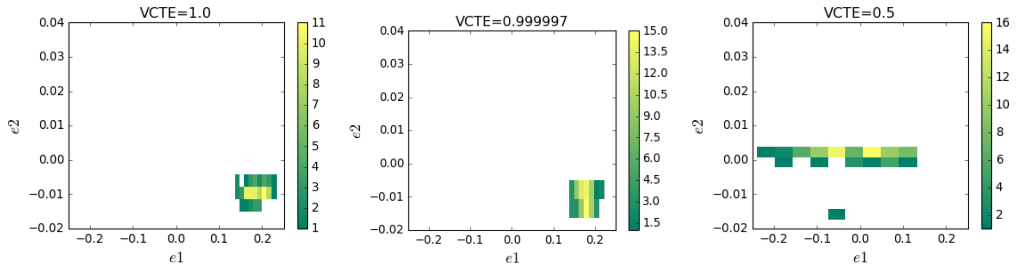


(a) (b) (c)

Figure 95: Histogram of $e1$ and $e2$ for (a) VCTE = 1 (b) VCTE=1-3e-6 and (c) VCTE=0.5.

### 6.3.11 CTE on cosmic shear correlation

As shown in Figure 96, while the correlation of HCTE=0.999995 was very similar to HCTE=1.0 case, extreme case of HCTE=0.5 brought huge increase in the correlation. Comparing the $\xi$ of each cases, $< \frac{\xi_{0.999995}}{\xi_1} >$ was 1.0047 and $< \frac{\xi_{0.5}}{\xi_1} >$ was 3.311.

For the accuracy limit, the $m$ and $c$ values below should be smaller than $3 \times 10^{-3}$ ($13 \times 10^{-3}$ for Y1) and and $2 \times 10^{-5}$ for Y10 LSST-DESC WL analysis as written in the LSST Dark Energy Science Collaboration Science Requirements Document [7].

$$g^{obs} = g^{true} + mg^{true} + c \tag{59}$$

In the introduction, the Equation (1.2.3) to measure the shear calibration parameters m1, m2, c1, and c2 using second moment terms was discussed as well. For VCTE $= 1 - 3 \times 10^{-6}$, $< \frac{\xi_{0.999997}}{\xi_{1.0}} >$ is 0.949 and m1=m2, c1 and c2 were -0.98, 0.065, and -0.00025 accordingly. With VCTE = 0.5 case, $< \frac{\xi_{0.5}}{\xi_{1.0}} >$ is very small, 0.0015, and $m$ and $c$ were (-0.359, -0.100) for g1 and (-0.378, -0.0016) for g2. Even with the VCTE of specification, the required limits of $m$ and $c$ fail. However we should be aware of that this was a one sensor simulation result with random objects and unrealistic background

options. Thus it will have large errors and unreliable shear calibration results. Further study on g1 and g2 accuracy is in progress. We can improve this by expanding the simulations to whole focal plane with real galaxies and background options. Figure 97 shows that the cosmic shear correlation will not be affected by VCTE $= 3 \times 10^{-6}$, but as CTE gets smaller, it brings significant change in cosmic shear correlation.

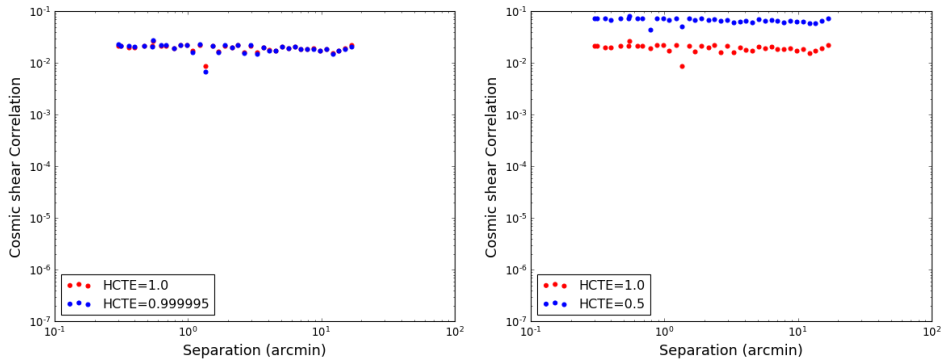


Figure 96: The cosmic shear correlation with various serial CTE values. Left : Red shows both CTEs = 1.0, and blue dots represent HCTE = 0.999995 as LSST specification. Right : Red shows both CTEs 1.0, and blue shows HCTE = 0.5. All with VCTE = 1.0

## 6.4 Conclusion

Two main sensor effects, Tree rings and CTE (Charge Transfer Efficiency) were measured during the Electro-optics tests in the cleanrooms of BNL and SLAC. These results were applied in PhoSim, GalSim and ImSim for the simulation of LSST sensors. We have used PhoSim to simulate Tree rings and CTE, and used GalSim for Tree rings only. Perfect case, extremely bad case, and average LSST sensor case were simulated. Comparing perfect case with extreme case, we could check that Tree rings and CTE both distort the shape of the circular light sources.

With the Tree rings, the symmetry in ellipticity $e1$ and $e2$ broke for the GalSim result. With PhoSim, $e1$ and $e2$ distribution got broader but the total ellipticity has not been changed even in the extreme case. The comparison of the second moments $XX$, $YY$ and $XY$ of the light sources with

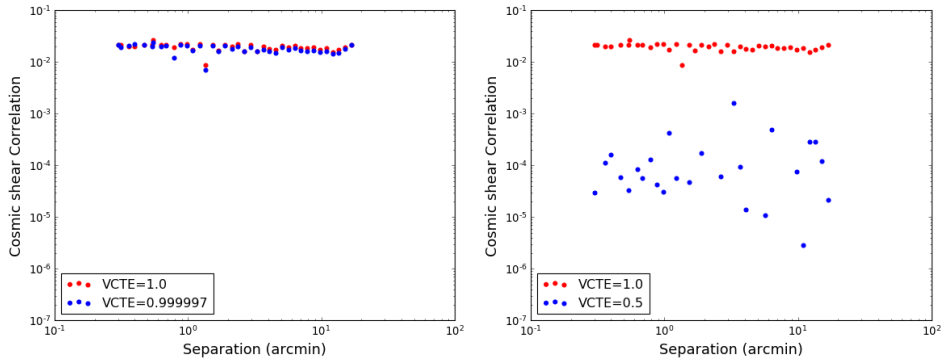


Figure 97: The cosmic shear correlation with various vertical CTE values. Left : Red shows both CTEs = 1.0, and blue dots represent VCTE = 0.999997 as LSST specification. Right : Red shows both CTEs 1.0, and blue shows VCTE = 0.5. All with HCTE = 1.0

and without Tree rings was also insignificant. The distribution of $YY$ and $XY$ got broader, but the median values remained similar in PhoSim results. In GalSim, $XX$ and $YY$ increased from 1.1 to 1.25 and their distribution got visibly broader as well. We checked with the cosmic shear correlation that Tree rings effect of LSST production sensors will be negligible for shear study. For the later research, we need to set the Tree ring option similar for both GalSim and PhoSim to define correct behavior of the change in the size and the shape due to Tree rings.

To see the change in size and shape due to CTE for LSST production sensors, the CTE values for the specification, HCTE $= 1 - 5 \times 10^{-6}$ VCTE $= 1 - 3 \times 10^{-6}$, were used. The perfect case for CTE means CTE = 1 and CTE = 0.5 was used for extreme case. In this extreme case for HCTE = 0.5, the second moment $XX$ and $YY$ changed from 5.23 to 6.84 and 3.88 to 3.93, and the ellipticity $e1$, $e2$ and e changed from 0.15, 0.0008, 0.1501 to 0.27, -0.00003, and 0.2720. When HCTE followed the specfication, the change in $XX$, $YY$, $XY$, $e1$, $e2$, and e were smaller than extreme case, but we could still check that $XX$ and total ellipticity increased.

However due to the fact that $XX$ is larger compared to $YY$ even with perfect CTEs, the shape of the source is more elliptical with perfect CTE, then becomes more circular when VCTE gets smaller. We could check this in the image showing the source shape, and also from the measurement of

second moments and ellipticity.

On the cosmic shear correlation plot, we could also check that HCTE and VCTE of LSST production sensors will not be robust to shear measurement. Interestingly, cosmic shear correlation showed opposite results for HCTE = 0.5 and VCTE = 0.5 cases. Because $XX$ is larger than $YY$ due to other effects, the shape of the source becomes more circular when CTI (Charge Transfer Inefficiency) increases and leave more electrons behind to make $YY$ broader. Therefore when HCTE decreases the correlation increases, but when VCTE decreases the correlation decreases.

The study on the required accuracy for weak lensing shear study in LSST-DESC Y1 to Y10 is still in progress. It will be studied deeper with multiple simulations with a whole focal plane results, with real galaxies and background options. We will check that Tree ring effect and CTE on LSST production sensors will satisfy the accuracy limit of $m$ and $c$ to be less than 0.003 (0.013 for Y1) and 0.0002. Once TXPipe is ready to use, we can use DC catalogs to compare the cosmic shear correlations with various sensor effect options.

As yet Tree rings on GalSim show closer result to LSST sensors, including the dependence on radius. The shape distortion and cosmic shear correlation change in GalSim were more evident, hence we are going to use GalSim to expand Tree ring study and use PhoSim for the CTE simulations.

# 7 Conclusions

## 7.1 Summay from the current work

Two main CCD sensor effects, Tree rings and Charge Transfer Efficiency (CTE), and the photo-z estimation were studied for precise measurement of LSST. Shape distortion due to gravitational lensing is a small effect and large scale structures are faint to detect, hence reducing noise and uncertainties is important in shear studies. Requirements of LSST-DESC for size and shape measurement errors should be less than 1% limit. The accuracy limit of weak lensing shear for LSST-DESC is 1.3% for Y1 and 0.3% for Y10 results.

### 7.1.1 Tree rings

By using Electro-Optics test images taken at BNL for 189 LSST production sensors, we have measured that the amplitude and the period of Tree rings depend on distances from the center of the wafer, wavelength of light, and back bias voltage. Dopant concentration variation of silicon wafer gets worse on the outer edge, hence we see larger amplitude and rapid periods of Tree rings pattern. Light with longer wavelength penetrates deeper into the silicon wafer. Between 350 nm to 900 nm where we can see Tree rings without Fringe pattern and where roughness of the surface doesn't dominate Tree ring pattern, we could see that Tree rings amplitude decreased, as for longer wavelength. Back bias voltage pulls electons faster to the bottom of the silicon, therefore electrons have less chance to be shifted. We checked that Tree ring pattern disappears as we increase back bias voltage. ITL will have -50 V and e2v will have -70 V applied as back bias voltage in real observations, and with this back bias voltage settings, we expect to have insignificant amplitude and periods of Tree rings effect.

### 7.1.2 CTE

LSST specification for CTEs are $1 - 5 \times 10^{-6}$ for the serial direction, and $1 - 3 \times 10^{-6}$ for the parallel direction. LSST have adjusted $1 - 3 \times 10^{-5}$ of HCTE to have a conditional pass. By testing all 21 Science Rafts of LSST, we have measured that the mean HCTE and VCTE were $1 - 0.6 \times 10^{-6}$ and $1 - 1.6 \times 10{-}6$. These results used EPER method, using the ratio of the flux on the actual image to the flux on the first two pixels of over scan region. We have introduced three methods and have shown that those methods do

not have significant correlations. The study with Fe-55 images to measure the CTE and to see its relation to other effects is in progress.

### 7.1.3 Photo-z and deblending

FoF matching was used to group the input and output catalogs by minimum separation distance and to bin them by the number of truth objects to coadd objects in each group. Two tools, MLZ and BPZ were used to estimate photometric redshift for [1-1], [2-1], [3-1], [1-2] and [2-2] groups on DC2-1.2i. Using MLZ, we have studied blended objects to estimate photo-z more precisely, and to de-blend coadd objects properly to be matched better with the truth objects. We have checked that the photo-z estimation of blended object correlates more with brighter object of truth catalog, which means [2 truth - 1 coadd] blended objects are caused by faint object merged by brighter object. We have found that that when two objects are blended to produce a single detection, the detection is surprisingly unbiased. This is because in most cases the blended objects are physically associated with redshifts closer than photometric redshift accuracy. Biases for multiple blends are more visibile but negligible within the accuracy of DC2 run 1.2i.

### 7.1.4 Shear correlation

We simulated point objects on grid with GalSim and randomly spread objects with PhoSim with all the other effects in fixed condition except values for Tree rings and CTEs, one at each time.

The second moments $XX$ and $YY$ increased from 1.1 to 1.25 in GalSim when the Tree ring amplitude was $4 \times 10^{-5}$. e1 and e2 increased from near zero to 0.045, meaning circular source gets distorted by Tree rings effect. In PhoSim simulation using Tree ring amplitude 0.7, Gaussian objects with sigma 1 arcsec had $XX$ and $YY$ increasing from (4.17, 5.55) to (4.21, 5.59). Point objects' $XX$ decreased from 3.880 to 3.872 and $YY$ increased from 5.267 to 5.286. The distribution of the ellipticity $e1$ and $e2$ got spread wider but total ellipticity did not change from 0.151. The shear correlation comparison between Tree ring amplitude $10^{-7}$ and 0.7 differed more while the shear correlation of Tree ring amplitude $10^{-7}$ to 0.03 almost overlapped each other with $\frac{\xi_{0.03}}{\xi_{0.0000001}} = 1.0093$.

For the CTE simulation using PhoSim, we have used two specification values for the HCTE and VCTE. For the comparison, we have used the

perfect CTE case with both CTEs 1.0, and the extremely bad CTE case with one of the CTEs 0.5. Due to the fact that second moment $XX$ is larger than $YY$ even with perfect CTE case, two cases of decreasing HCTE and VCTE showed opposite results on shear correlation. As charge transfer inefficiency increases, more electrons are left behind, so the size in x and y direction will increase for HCTI and VCTI accordingly. When VCTE decreased, the second moment $YY$ increased to become closer to $XX$. Therefore the shape of the sources became more circular, and the shear correlation got smaller for smaller VCTE.

Comparing the shear correlation with Tree ring amplitude 0.03 and with CTEs as in specification, we verified that the Tree ring effect and CTE on LSST production sensors will not bring any significant changes in shear correlation.

## 7.2 Prospects for the future

The study on the sensor effects to measure the shear more precisely is in progress. We will use the accuracy of shear $g1$ and $g2$ measurement by the terms shown below.

$$g^{obs} = g^{true} + mg^{true} + c$$

The required limits of $m$ and $c$ are $3 \times 10^{-3}$ and $2 \times 10^{-4}$ accordingly for the Weak Lensing working group of DESC. By using the whole focal plane simulations and with multiple simulations, we are going to expand this study to correctly calibrate the accuracy of shear measurement and to see how significant the systematics affect the result.

There will be automated codes and tools called TXPipe, to compare the shear correlation using the DC2 catalogs with and without the sensor effects. This is on going project, so it was not be discussed in this dissertation, but once it is ready we will be able to run full LSST focal plane simulation of real galaxies.

The research on photo-z estimation with DC2 1.2i catalogs will be applied for DC2 2.1p and 2.1i catalogs soon. The issue with the color matching is has been resolved and we are going to run same procedure on 2.1 catalogs for the FoF matching and photo-z estimation. With the new version of the catalogs, we are going to measure the covariance matrix and show how significant the error of the photo-z estimation and blending will affect the mass and

shear correlations. Using these results, we are going to develop the BPZ tool to measure redshift more accurately and to deblend blended objects in the output catalogs.

# References


[1]C. Chang, S. M. Kahn, J. G. Jernigan, et al., "Spurious shear in weak lensing with the Large Synoptic Survey Telescope", MNRAS (2013).

[2]Dark Energy Survey Collaboration, "Dark Energy Survey year 1 results: Cosmological constraints from galaxy clustering, weak lensing", Phys.Rev. (2018).

[3]V. Springel, C. S. Frenk, and S. D. M. White, "The large-scale structure of the Universe", Nature (2006).

[4]Dark Energy Survey Collaboration, "Dark Energy Survey Year 1 results: Cosmological constraints from cosmic shear", Phys.Rev. (2018).

[5]H. Park, A. Nomerotski, and D. Tsybychev, "Properties of Tree Rings in LSST sensors", Jinst (2017).

[6]F. Christen, K. Kujiken, D. Baade, C. Cavadore, S. Deiries, and O. Iwert, "CCD Charge Transfer Efficiency (CTE) Derived from Sicnal Variance in Flat Field Images", Scientific Detectors for Astronomy (2005).

[7]Dark Energy Science Collaboration, "The LSST Dark Energy Science Collaboration (DESC) Science Requirements Document version1", (2018).

[8]H. Park, S. Karpov, and A. Nomerotski, D.Tsybychev, "Tree Rings on LSST production sensors: their dependence on radius, wavelength, and back bias voltage", SPIE (2019).

[9]B. Beamer, A. Nomerotski, and D. Tsybychev, "A study of astrometric distortions due to "tree rings" in CCD sensors using LSST Photon Simulator", Jinst.

[10]S. E. Holland, C. J. Bebek, W. F. Kolbe, and J. S. Lee, "Physics of fully depleted CCDs", Jinst (2014).

[11]A. A. Plazas, G. M. Bernstein, and E. S. Sheldon, "On-sky measurements of the transverse electric fields' effects in the Dark Energy Camera CCDs", PASP (2014).

[12]P. O'Connor, P. Antilogus, P. Doherty, J. Haupt, S. Herrmann, M. Huffer, C. Juramy-Giles, J. Kuczewski, S. Russo, C. Stubbs, and R. Van Berg, "Integrated system tests of the LSST raft tower modules", SPIE (2016).

[13]DESC, "LSST DESC Science Roadmap Version v1.3", (2018).

[14]R. Coles, J. Chiang, D. Cinabro, W. Gilbertson, J. Haupt, I. Kotov, H. Neal, A. Nomerotski, P. O'Connor, C. Stubbs, and P. Takacs, "Verification of Absolute Calibration of Quantum Efficiency for LSST CCDs", AAS (2016).

[15]A. Gorecki, A. Abate, R. Ansari, A. Barrau, S. Baumont, M. Moniez, and J. Ricol, "A new method to improve photometric redshift reconstruction: Applications to the Large Synoptic Survey Telescope", ESO (2018).

[16]Y. Okura, A. A. Plazas, M. May and T. Tamagawa, "Spurious shear induced by the tree rings of the LSST CCDs", Jinst (2015).

[17]I.V.Kotov, J.Haupt, P.O'Connor, T.Smith, P.Takacs et al., "Characterization, acceptance testing of fully depleted thick CCDs for the Large Synoptic Survey Telescope", SPIE (2016).

[18]J. R. Janesick, *Scientific Charge-Coupled Devices* (SPIE).

[19]LSST Science Collaboration, *LSST Science Book* (2009).

[20]P. Z. Takacs, P. O'Connor, et al. (LSST Camera Team), "LSST Detector Module, Raft Assembly Metrology Concepts", (2006).

[21]LSST Camera Team, "An automated system to measure the quantum efficiency of CCDs for astronomy", (2017).

[22]I. V Kotov, J. Haupt, P. O'Connor, T. Smith, P. Takacs, H. Neal and J. Chiang, "Characterization, acceptance testing of fully depleted thick CCDs for the Large Synoptic Survey Telescope", in High Energy, Optical, and Infrared Detectors for Astronomy VII (2016).

[23]P. O'Connor, P. Antilogus, P. Doherty, J. Haupt, S. Herrmann, M. Huffer, C. Juramy-Giles, J. Kuczewski, S. Russo, C. Stubbs, et al., "Integrated system tests of the LSST raft tower modules", in High Energy, Optical, and Infrared Detectors for Astronomy VII (2016).

[24]W. A. Dawson, M. D. Schneider, J. A. Tyson and M. J. Jee, "The Ellipticity Distribution of Ambiguously Blended Objects", (2015).

[25]N. Petitdidier, "LSST: Characterization of the CCD sensors", (2015).

[26]DES Collaboration, "Instrumental Response Model and Detrending for the Dark Energy Camera", (2017).

[27]DES Collaboration, "Astrometric Calibration, Performance of the Dark Energy Camera", (2017).

[28]G. M. Bernstein, T. M. C. Abbott, R. Armstrong, D. L. Burke, H. T. Diehl, R. A. Gruendl, M. D. Johnson, T. S. Li, E. S. Rykoff, A. R. Walker, W. Wester and B. Yanny, "Photometric Characterization of the Dark Energy Camera", (2018).

[29]R. Mandelbaum, "Instrumental systematics, weak gravitational lensing", (2015).

[30]R. Mandelbaum, H. Miyatake, T. Hamana, et al., "The first-year shear catalog of the Subaru Hyper Suprime-Cam SSP Survey", (2017).

[31]M. Jarvis, "Challenges for precision shape measurements", (2014).

[32]D. Gruen, G. M. Bernstein, M. Jarvis, B. Rowe, V. Vikram, A. A. Plazas and S. Seits, "Characterization, correction of charge-induced pixel shifts in DECam", (2015).

[33]LSSTDESC, *TXPipe*, `https://github.com/LSSTDESC/TXPipe`.

[34]M. Jarvis, R. Mandelbaum and J. Meyers, *GalSim*, `https://github.com/GalSim-developers/GalSim`.

[35]K. L. Hazelwood, S. G. Olenych, J. D. Griffin, C. S. Murphy, J. A. Cathcart and M. W. Davidson, *Concepts in Digital Imaging Technology*, `http://hamamatsu.magnet.fsu.edu/articles/microscopyimaging.html`.

[36]J. Peterson, *PhoSim*, `https://bitbucket.org/phosim/phosim_release/wiki/Home`.

[37]*Wikipedia: Shear*, `https://en.wikipedia.org/wiki/Gravitational_lensing_formalism`.

[38]*COSMOS, GAIA*, `https://www.cosmos.esa.int/web/gaia/dr2`.

[39]D. N. Spergel, L. Verde, H. V. Peiris, E. Komatsu, M. R. Nolta, C. L. Bennett, M. Halpern, G. Hinshaw, N. Jarosik, A. Kogut, M. Limon, S. S. Meyer, L. Page, G. S. Tucker, J. L. Weiland, E. Wollack and E. L. Wright, "First Year Wilkinson Microwave Anisotropy Probe (WMAP) Observations: Determination of Cosmological Parameters", Astrophysical Journal (2003).

[40]C. Baugh, "Correlation Function, Power Spectra in Cosmology", IOP (2006).

[41]T. Lange, B. Bowdish, S. Russo, S. Tether, S. W. Digel, T. Johnson, S. P. Newbry, A. P. Rasmussen, V. T. Lee, K. A. Reil, T. Bond, and G. Dho, "LSST craft raft integration support equipment: design, assembly, and test status", Ground-based Airborne Instrumentation for Astronomy (2018).

[42]J. Scargle, "Studies in astronomical time series analysis. II - Statistical aspects of spectral analysis of unevenly spaced data", APJ (1982).

[43]C. R. Keeton, C. S. Kochanek, U. Seljak, "Shear, Ellipticity in Gravitational Lenses", (1996).

[44]V. Radeka, J. Frank, J. C. Geary, D. K. Gilmore, I. Kotov, P. O'Connor, P. Takacs, J. A. Tyson, "LSST sensor requirements, characteriation of the prototype LSST CCDs", (2009).

[45]J. E. Meyers, P. R. Burchat, "Impact of Atmospheric Chromatic Effects on Weak Lensing Measurements", (2018).

[46]M. C. Kind; R. Brunner, "MLZ: Machine Learning for photo-Z", (2014).

[47]A. Nomerotski, "New characterization techniques for LSST sensors", (2015).

[48]B. Ryden, *Introduction to Cosmology* (2002).

[49]J. Anderson, L. R. Bedin, "An Empirical Pixel-Based Correction for Imperfect CTE. I. HST's Advanced Camera for Surveys", (2010).

[50]T. Hardy, R. Murwinski, M. J. Deen, "Charge Transfer Efficiency in Proton Damaged CCD's", (1998).

[51]J.A.Tyson, J.Sassian, K.Gilmore, A.Bradshow, C.Claver, M.Klint, G.Muller, G.Poczulp, and E.Resseguie, "LSST optical beam simulator", (2014).

[52]P. O'Connor, "Uniformity and Stability of the LSST Focal Plane", (2019).

[53]D. Kirkby, *AstroCCD*, `https://github.com/dkirkby/AstroCCD`.

[54]S. Karpov, *Tree Rings Analysis*, `https://github.com/karpov-sv/lsst-misc/blob/master/Tree_Rings_Analysis.ipynb`.

[55]*e2v*, `https://www.teledyne-e2v.com/products/imaging/`.

[56]*ITL*, `http://www.itl.arizona.edu/doku.php`.

[57]*NASA WMAP science team*, `https://wmap.gsfc.nasa.gov/news/5yr_release.html`.

[58]*LSST*, `https://www.lsst.org/`.

[59]*NASA-WMAP*, `https://map.gsfc.nasa.gov/media/080998/index.html`.

[60]*Machine Learning for Photo-z*, `http://matias-ck.com/mlz/`.

[61]A. Christov, *Sensor Anomalies Working Group meeting.*

[62]M. Jarvis, *TreeCorr*, `https://github.com/rmjarvis/TreeCorr`.

[63]E. Bertin, *SExtractor*, `https://www.astromatic.net/software/sextractor`.

[64]E. Sheldon, *ngmix*, `https://github.com/esheldon/ngmix`.

[65]M. Jarvis, G. Bernstein, B. Jain, "The skewness of the aperture mass statistic", (2004).

[66]S. Bridle, J. Shawe-Taylor, A. Amara, et al., "Handbook for the GREAT08 Challenge: An image analysis competition for cosmological lensing", (2008).

# Appendix A Orientations of tree rings for LSST Science Rafts

## A.1 Tree ring orientations

Tree ring orientations for the sensors as they are installed in the rafts are indicated with arrows. The location of the sensors in the rafts is given by labels S00 – S22. Two tables on the right side provide the raft serial numbers as they are presented in A.2 for the ITL rafts and in A.3 for the e2v rafts.

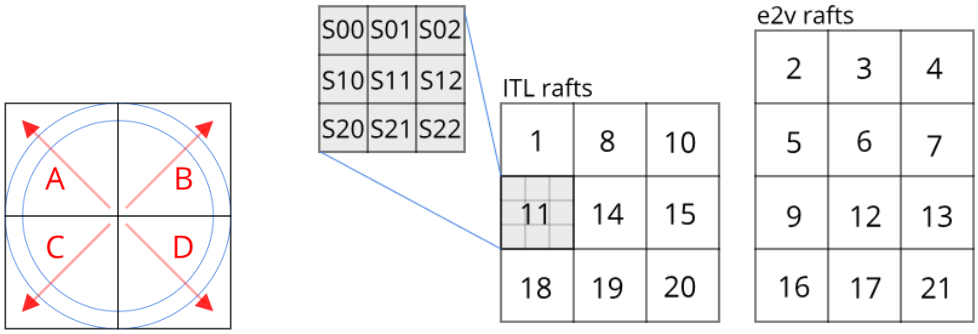

## A.2 ITL rafts

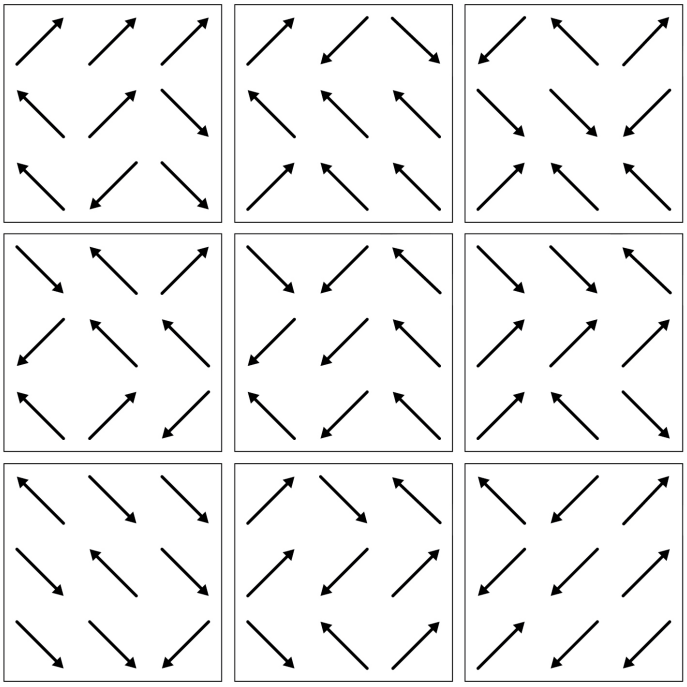

Figure 98: Tree ring orientations for 81 ITL sensors. Respectively 25, 21, 17 and 18 sensors have A, B, C and D directions.

## A.3 e2v rafts

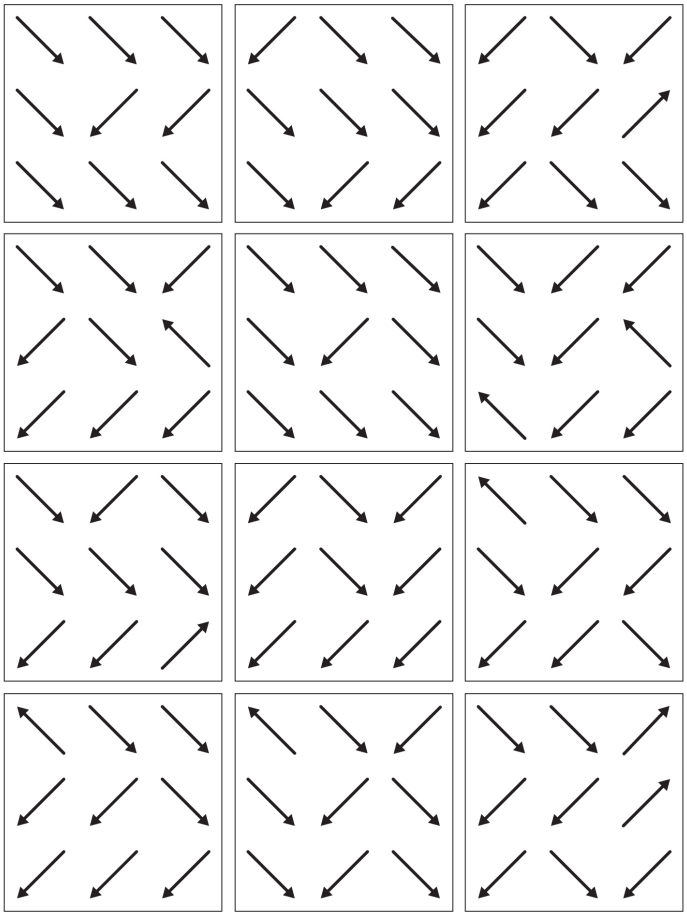

Figure 99: Tree ring orientations for 108 e2v sensors. Respectively 6, 4, 47 and 51 sensors have A, B, C and D directions.

# Appendix B Python scripts

## B.1 DMstack to measure x, y, xx, yy, and xy

Code Listing 1: Measuring x, y, xx, yy, and xy from lsst.pipe.tasks.characterizeImage. Code written by C. Lage and H. Park.

```
x=charResult.sourceCat['base_SdssCentroid_x'] #position x
y=charResult.sourceCat['base_SdssCentroid_y'] #position y
xx =charResult.sourceCat['base_SdssShape_xx'] #second moment XX
yy = charResult.sourceCat['base_SdssShape_yy'] #second moment YY
xy=charResult.sourceCat['base_SdssShape_xy'] #second moment XY
```

## B.2 DMstack to measure e1, e2, and ellipticity residulas

Code Listing 2: Measuring e1, e2, g1, and g2 from lsst.pipe.tasks.characterizeImage. Code written by C. Lage and H. Park.

```
def ellipticity(i_xx, i_yy, i_xy):
    e1 = (i_xx - i_yy) / (i_xx + i_yy)
    e2 = (2. * i_xy) / (i_xx + i_yy)
    return e1, e2
e1_without, e2_without =
    ellipticity(charResult.sourceCat['slot_Shape_xx'],
                            charResult.sourceCat['slot_Shape_yy'],
                            charResult.sourceCat['slot_Shape_xy'])
e1_with, e2_with =
    ellipticity(charResult2.sourceCat['slot_Shape_xx'],
                           charResult2.sourceCat['slot_Shape_yy'],
                           charResult2.sourceCat['slot_Shape_xy'])
e1_res, e2_res = e1_without - e1_with, e2_without - e2_with
```

## B.3 TreeCorr example

```
nbins=40
min_sep=0.25
max_sep=20
sep_units='arcmin'
verbose=False
g1=e1_with #or e1_without #for shear correlation
g2=e1_with #or e2_without #for shear correlation
catTree = treecorr.Catalog(ra=RA,dec=DEC,
                           g1=g1, g2=g2,
                           dec_units='arcsec', ra_units='arcsec')
gg = treecorr.GGCorrelation(nbins=nbins, min_sep=min_sep,
    max_sep=max_sep,
                            sep_units=sep_units,
                            verbose=verbose)
gg.process(catTree)
r = np.exp(gg.meanlogr) * u.arcsec
xip = gg.xip * u.Unit('')
xip_err = np.sqrt(gg.varxi) * u.Unit('')
```